Dissertation Advisor: Professor Mehmet Toner Joseph Maurice Martel

Particle Focusing in Microchannels

Abstract

The ability to control the motion of particles and cells in microchannels has been a center of fascination since the advent of microfluidics. Entire fields have been created in order to accomplish separation, volume reduction and overall positioning of particles and cells within microfluidic devices in the fastest and most accurate manner possible. While most of these technologies rely on low Reynolds number operation, one technique entitled inertial focusing takes advantage of the inertia of the surrounding fluid and the interaction between a particle and the channel itself which cause the lateral migration of particles across streamlines to equilibrium positions within a flow. The major advantage of inertial microfluidics in biomedical and microfluidic applications is that it is inherently high throughput being dependent on inertia whereas most microfluidic concepts are dependent on low Reynolds number operation.

This dissertation presents new experimental evidence of the dynamics and equilibrium behaviors of particles within inertial flows. Through the variation of several important parameters including Reynolds number, particle confinement ratio, curvature ratio and residence time were varied in order to clarify the importance of each in terms of eventual inertial focusing behaviors. New regimes of inertial focusing towards and away from the center of curvature are detailed. The transition between these two regimes is shown to be a set of flow conditions where a single lateral and vertical equilibrium

position is achieved. New parameters are defined describing these different regimes and the transition. The capability of separating particles by size by taking advantage of the different regimes is discussed. Finally, a hypothesis for the underlying mechanism behind the range of behaviors is presented. This hypothesis combines the effects of not only the Dean drag and inertial lift but also the redistribution of the velocity profiles that occurs with Dean flow and its effect on the shear gradient lift forces key to the determination of equilibrium positions. This new understanding of these high-throughput inertial focusing modes is one step toward the development of a complete theory of inertial focusing that can be used to design solutions for future biomedical technologies.

Table of Contents

List of Figures

List of Tables

Citations to Previously Published Work

Large portions of Chapter 4 appeared in the following paper:

> Martel, J. and Toner, M. "Inertial Focusing Dynamics in Spiral Microchannels." Physics of Fluids, 24, 032001 (2012).

Acknowledgements

I could not have written this dissertation without the support of many people who continued to believe in me, even at times when I did not believe in myself.

First, I want to thank my best friend and the Love of my life, my wife Rosie Martel-Foley, for her unwavering Love, encouragement, and patience. This has been a long process and you have been my most important life-line and strongest supporter through it all, for which I am infinitely thankful. And to our Layla, I owe thanks for the persistent but productive distractions of a good walk and a good laugh.

I am forever grateful to my family, the Martels and the Foleys, and my friends for their loyal support, genuine interest in my projects, and, of course, for their understanding of my absence. I am especially appreciative of my mother, Adele D'Amico Martel, as I have long striven to follow in her scientific footsteps, and I have benefited grateful from her input throughout my pursuit of this degree.

I have had the honor and joy of working with numerous people at the BioMEMS Resource Center, to whom I am all so grateful. They have kept me sane and caffeinated. Specifically, thanks to Bashar Hamza, Elisabeth Wong, Laurie Dimisko and Nil Gural for their friendship and advice. Thanks to Ian Wong, Anh Hoang and Shannon Stott for their mentorship over the years. Thanks to Octavio Hurtado for his endless patience and knowledge. To A.J. Aranyosi for teaching me how to say "no" and for his help as a fellow Micro-Pier. To Daniel Irimia for helping me teach and offering advice over the years, and also for his help as fellow a Micro-Pier. To Dino Di Carlo for his interest and inspiration. I want to give a special acknowledgement those who have survived the BMRC experience with me: Ajay Shah, Sukant Mittal, and Eugene Lim, thanks for

always sympathizing and sharing a good discussion. And thanks to Vijay Ambravaneswaran for teaching me that you can only be expected to do 4 good hours of work per day. Thanks to Brian Storey for the opportunity to teach and for his help with fluids problems.

Thanks to all those I have had the pleasure of working with as part of collaborations and side projects, especially Beth Fuchs, Jerome Fung and Anna Wang.

Thank you to my committee for their valuable time and energies dedicated to the review of this dissertation.

Thank you to the BioMEMS Resource Center, National Science Foundation, National Institute of Health, and Harvard University for their financial support that made my research and this dissertation feasible.

Most of all, I am so grateful to Mehmet Toner for his endless ideas, vision, patience, and support. It has been a pleasure working under your guidance over the past four years, and I have gained so much as the result of your leadership.

Chapter 1

Introduction

1.1 Motivation

Biological fluids contain a plethora of clinically relevant materials that have been utilized for disease and infection detection throughout history. As technology has developed our understanding of the cells within the fluids has also grown. With the simple early microscopes, differentiation between cells was done by size and shape. As equipment and staining techniques were improved numerous other subpopulations were discovered as well as the function of some of the different cells. These types of classification are still used today. In fact, one of the most utilized medical tests involves measuring the ratio of the different types of blood cells within a sample of blood or a complete blood count (CBC). Another highly utilized test involves a pathologist looking at a concentrated volume of fluid smeared or spun onto a glass slide and stained looking for cells of interest. State of the art technology now allows for the interrogation of these cells in new ways using DNA sequencing and antigen presentation measurements. These measurements have proven that even the different subpopulations of cells can be complex and even heterogenous on the single cell level.

Through this type of investigation numerous important target cells within biological fluids have been discovered at very small numbers. These rare or dilute cells have been implicated in cancer and infection and are thus important to study in terms of their roles in the diseases. Even with state-of-the-art technology it is still difficult to detect and isolate these cells. One of the main complicating factors for the isolation of these key

cells are the composition of the fluids which varies widely, from blood and bone marrow aspirate, have complex properties and a seemingly infinite number of background cells, to extremely dilute lavage or urine samples, which are mostly liquid and can be as large as 2 liters in volume. The requirement that several of these cells be collected for further analyses also increases the volume of fluid to be processed. Effectively and efficiently finding and isolating these rare or dilute cells from biological fluids has the potential to revolutionize medicine and our understanding of the human body but can be very challenging. However, the constant theme is that such fluids hold key information with respect to the cells they contain.

Rare cells in blood: Blood is perhaps the most intriguing biological fluid due to the large variety of rare cells that can be found in circulation, several of which are presented in Figure 1-1, and the ease in which it can be collected. Some of these rare cells are indicative of systemic issues and are incredibly important to detect during early stages of the diseases.

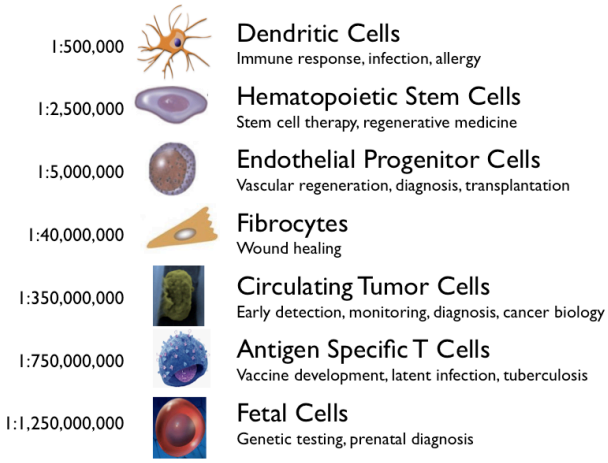

Figure 1-1: Clinically relevant cells found circulating in the blood stream as well as their ratio to background nucleated cells.

For instance, circulating tumor cells (CTCs) may be found at a rate of only 1-100 cells in a milliliter of blood, but the presence of these cells is an indicator for metastatic cancer,

the cause of 90% of cancer deaths [1-4]. Fungal cells may appear at the same rate as CTCs, and are a marker of fungemia, a surprisingly devastating infection whose mortality rate climbs steeply if not treated within the first 12 hours [5, 6].

Large volumes of bodily fluids with very dilute cellular components: While the primary challenge of isolating rare cells from blood is the rarity of the target cells relative to the background population, numerous other biological fluids that contain similarly important information present other unique challenges such as being extremely dilute. Peritoneal washings [7-9], ascitic fluid analyses [10], bronchoalveolar lavages [11-15], colonoscopic lavages [16], spinal taps (cerebrospinal fluid) and urinalyses [17, 18], among other medical procedures, produce large volume fluid samples for which accurate and timely processing is key to the correct diagnosis and successful treatment of cancers and numerous other diseases.

Large volume bodily fluid samples are also extremely difficult to process. Samples are normally split into dozens of smaller tubes and then centrifuged, aspirated, mixed and centrifuged again. The multiple, repetitive steps required of this time-intensive process amplify user errors and can increase the false positive rates for the infections of interest. Each of these large volumes of fluid must be processed for the collection of extremely dilute species of particles or cells for the diagnosis and monitoring of disease proliferation and treatment effectiveness. In both cases, whether the cells are rare or sparse, it is challenging to isolate them due to non-specific contaminating cells and/or the large volumes of fluid as depicted in Figure 1-2.

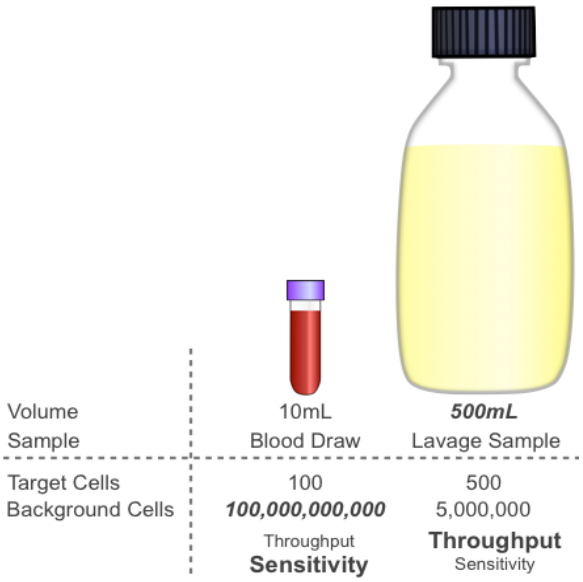

Figure 1-2: Figure motivating the different engineering challenges posed by different bodily fluids.

1.2 Microfluidics

Microfluidic technologies, with micron-scale channel dimensions comparable to the target cells, emerged a potential solution of choice to process the various bodily fluids discussed above. There are myriad of "passive" and "active" microfluidic technologies already available for separating cells. Passive techniques are used to manipulate and separate cells on the microscale without an externally applied force or field. These passive techniques include hydrophoresis [19], deterministic lateral displacement [20] and gravitational methods [21]. Both hydrophoresis and deterministic lateral displacement utilize low Reynolds number behaviors based upon the fluid and particles interacting with structures along a channel to cause the separation of particles by size. These are shown graphically in Figure 1-3 a and b, respectively.

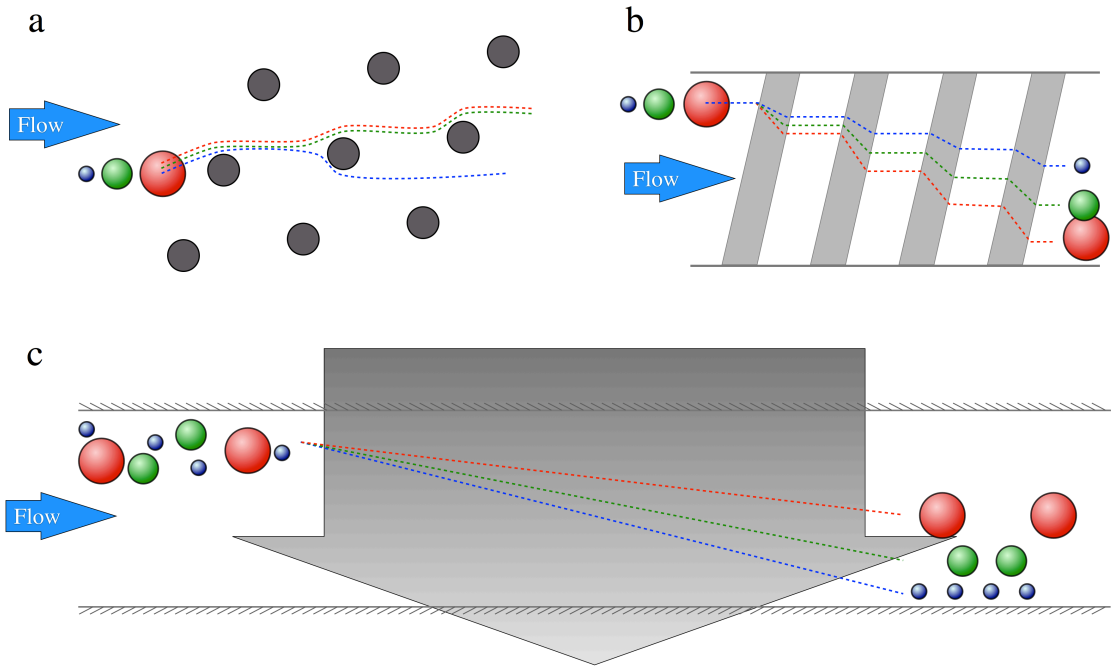

Figure 1-3: Conceptual comparison of passive and active microfluidic techniques for the separation of particles by size.

Hydrophoresis is based upon the generation of transverse pressure gradients in a microchannel with slanted obstacles. This pressure gradient then sets up a secondary flow, which can be used to guide and separate particles. This can also be used in conjunction with Weir-type filters that pass only particles below a certain size range [22-24]. Deterministic lateral displacement works on a similar particle-structure interaction principle. In the absence of structures particles flowing through a straight channel at low Reynolds number will follow the streamline where their center of mass is located. When a particle interacts with an obstacle, the way in which it moves around the obstacle is dependent on this same center of mass streamline. As it passes the obstacle its center of mass crosses streamlines as it rolls along the surface of the obstacle. A larger particle will therefore cross more streamlines, as its center of mass will end up further from the obstacle due to steric effects. If the obstacles are shifted in the direction of the flow a certain distance related to the particle size, some particles will always bump the same

direction around each obstacle while others will alternatively pass in either direction depending on their initial position. This creates a critical diameter above which particles will move along the shifted obstacles and below which particles will essentially pass straight through the array. This critical particle diameter can be calculated and adjusted based upon the design parameters of the array [25, 26]. Gravitational separation works on the basic principle that particles of different sizes will have different terminal velocities in a gravitational field since the balance of Stokes' drag and buoyancy forces scale differently with diameter and volume respectively. While gravitational separation is using an external field and operates much like the other field flow fractionation techniques, it is considered passive in this case since it is not an actively applied or modulated field.

Active techniques include dielectrophoresis [27-29], acoustophoresis [30], and magnetophoresis [31]. These techniques are all considered field flow fractionation (FFF) techniques in which par ticles within a flow are moving at relatively uniform velocities, and then a field (electrical, magnetic or acoustic) is applied causing the separation of particles by their size or other properties. This generalized technique is depicted in Figure 1-3c. Dieletrophoretic forces are dependent on not only the size of the objects but also their electrical properties and the electrical properties of the surrounding fluid in addition to the properties of the electrical field [29, 32]. Acoustophoresis uses standing sonic waves to generate a pressure force on a body suspended in a fluid proportional to the particle size. Magnetophoresis is reliant on the use of magnetic beads, which can be attached to cells of interest through antibody-antigen interactions. The advantage of using magnetophoresis out of all of the FFF techniques is that biological samples have minimal naturally occurring magnetic properties leading to excellent separation sensitivity.

Several reviews comparing these different separation modalities are also available in literature [33-35]. In general, these techniques rely on the low Reynolds nature of the fluid flow to allow for the separation technique to occur in an ordered and predictable fashion. While all of these concepts have proven successful for a variety of biological applications, their low throughput has been a principal impediment, preventing their widespread use and application to the rare cell isolation. This major challenge of being able to process real-world sized samples efficiently has been known since the beginning of the field of microfluidics [36]. The field continues to ask: is it possible to take advantage of microfluidic sensitivity without the limitation on throughput? The solution to this real-world problem may well lie within a regime of inertial fluid dynamics on the microscale where suspended particles migrate across streamlines to predictable equilibrium positions within a flow. The reliance on the inertia of the fluid in the system rather than the desire to limit its effects, as normally done in microfluidics, results in a significantly higher throughput.

1.3 Thesis Structure

The ability to control particles within fluids based upon their mechanical properties is of significant interest both experimentally and for application to solve real-world biomedical and industrial problems. This dissertation presents and discusses experimental evidence of the behavior of neutrally buoyant suspended particles moving through microchannels in inertial flows across a wide range of experimental conditions in an attempt to better understand and predict how particles of different sizes migrate and equilibrate in such flows. The improved understanding of such systems presented will benefit the future design of devices for the aforementioned biomedical applications.

Chapter 2 details the evolution of the field of inertial focusing from its discovery through the microfluidic renaissance. This includes a description of the current understanding of inertial forces on neutrally buoyant particles as well as the different biomedical applications completed to date.

Chapter 3 presents the detailed methodology for fabricating, testing and analyzing inertial focusing behavior. Specifically highlighted is a novel method for creating rigid microfluidic channels.

Chapter 4 presents experimental evidence and associated improvements in the understanding of the dynamics of inertial focusing behaviors along curved microchannels. A new adjusted ratio of forces factor is defined for the prediction of the onset of inertial focusing in curved channels. A relationship between the streak width and the stability of focusing for a given device is demonstrated and an upper limit on particle confinement for the current designs is given.

Chapter 5 presents experimental data supporting a hypothesis of the three-dimensional nature of inertial focusing in curved channels. Two distinct regimes of focusing are defined in terms of the eventual behaviors. Through the separate variation of three different non-dimensional parameters, new scaling parameters are defined for the different regimes of inertial focusing behavior including the transition between the two regimes. The scaling differences are also examined in terms of particle size and the meaning of the results in terms of the ability to separate particles.

Chapter 6 presents and discussed an improved model for the direct numerical simulation of forces on a sphere in inertial focusing flows in curved channels using the finite element method. This model incorporates the redistribution of the velocity profile

due to the secondary flow perpendicular to the axial flow. Preliminary results for the effect of this redistribution are given in terms of the three-dimensional position of the particle streaks.

Chapter 7 summarizes the contributions presented in this dissertation and highlights the critical next steps to advance the understanding and application of inertial focusing to not only the biomedical device community but other industrial applications as well.

Chapter 2

Review of Inertial Focusing

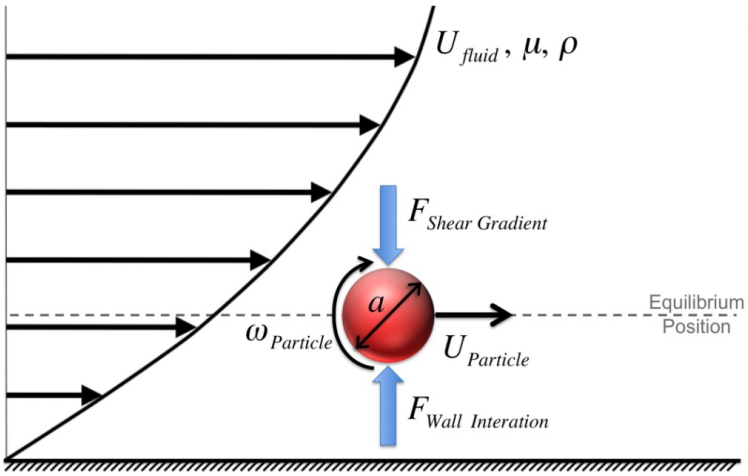

Figure 2-1: Schematic of a particle in a parabolic flow field near a wall and the associated forces.

2.1 Origins of Inertial Focusing

The lateral migration of particles in confined flows due to inertial effects was initially discovered by Segré and Silberberg in 1961. Their experiments in a cylindrical pipe (~1cm diameter) found that particles (~1mm diameter) migrated to an annulus ~0.6 times the radius of the pipe between the centerline of the pipe to the wall, entitled the 'tubular pinch effect' [37-39]. From analysis of the Stokes equations for fluid motion at a Reynolds number of zero, or without inertia, it is understood that single particles in a flow are unable to cross streamlines due to the symmetric nature of the flow around the particle [40]. Here, Reynolds number is defined as the ratio of inertial to viscous effects in a channel flow,

$$\mathrm{Re}_C = \rho U_{Max} D_h / \mu \tag{2.1}$$

where ρ is the fluid density, μ is the fluid viscosity, U_{Max} is the maximum velocity of the fluid and D_h is the hydraulic diameter of the channel defined as $D_h=2hw/(h+w)$ where h and w are the height and width of the channel cross section respectively. Segré and Silberberg revealed a non-linear dependence of the lateral migration velocity on the axial velocity at a small but non-zero Reynolds number proving that the migration effect was due to the inertia of the fluid [37]. This discovery motivated attempts by numerous theorists to explain this motion, as the current theories for lateral motion of particles could not explain these experimental results. One of these theories from Rubinow and Keller (1961) recently provided a theoretical explanation for the Magnus force, which is lift on a rotating object in a uniform flow, but could not explain the Segré and Silberberg equilibrium position because the Magnus force was always directed towards the center of the pipe when applied to the Segré and Silberberg experiments [41].

A comprehensive historical summary of the development of the modern understanding of inertial focusing is given by Matas, Morris and Guazzelli (2004) based on Feng (1994), and is briefly summarized here [42, 43]. Two major advancements since the initial attempts to explain the Segré and Silberberg results have contributed to the development of the current understanding of inertial lift. First, Saffman (1965) developed a theoretical force independent of the particle rotation due solely to the difference in fluid velocity on either side of the particle in a linear shear flow [44]. This force was found to be dependent on the difference in velocity between the particle and the undisturbed velocity profile at the same position within the flow. At the time, this helped justify some of the experimental results for sedimenting particles in flows, but was still unable to

account for the equilibrium position of the neutrally buoyant particles of Segré and Silberberg [45, 46].

The second major addition to the study of inertial focusing occurred when Ho and Leal (1974) and Vasseur and Cox (1976) applied similar analytical techniques to quadratic flows and found a force directed towards the walls of a channel proportional to the variation in shear rate [47, 48]. This shear gradient lift force coupled with a wall-interaction induced repulsive force accurately predicted the Segré and Silberberg equilibrium position. It was determined at this point that the shear gradient lift force was actual only one of three effects, but by far the most dominant. The Saffman lift force due to the velocity difference between the particle and the undisturbed fluid (sometimes referred to as lag or slip velocity) was found to be a single order of magnitude smaller and a rotation induced lift force three orders of magnitude smaller [47]. The majority of these early analyses utilized perturbation methods, each of which come with distinct validity limitations depending on the expansion parameters utilized and depending on the solution procedure limitations depending on the definition of the domains prescribed near and far from the particle [43]. These restrictions were usually on the size of the particle, the particle being far enough from the wall, and/or low Reynolds number. More recent advancements have still been able to utilize these methods with relaxed restrictions [49], however, with the improvements of computational power, the direct numerical simulation of the problems has removed these theoretical restrictions [43]. Importantly, these early simulations were for two-dimensional problems alone but still elucidated the different mechanisms of motion and helped provide intuitive explanations for the forces by directly investigating the pressure and shear forces on a particle's surface.

Most modern results have improved upon the numerical or analytical methods to relax Reynolds number restrictions. Interesting effects have been measured and described concerning the movement of the equilibrium position towards the wall of a channel at increasing Reynolds number [42, 49] and the possibility of a secondary position that occurs due to the non-linear shear gradient lift force [50, 51]. A direct comparison of cylindrical channels and a 2D planar geometry also showed that the forces in a planar channel are higher than in a pipe [50]. The earliest three-dimensional (3D) model of these behaviors was developed in 2006 by Chun and Ladd using lattice-Boltzmann to investigate the transient motion of particles in a rectilinear cross-sectioned channel that predicted 8 equilibrium positions, one in each corner and one centered on each face of the rectangular cross section [52]. At this point, inertial focusing was mostly a scientific curiosity, but that changed with the advent of microfluidics.

2.2 Inertial Focusing in Microfluidics

Microfabrication and microfluidics allowed the direct investigation of various rectilinear geometries like the ones depicted in the Chun and Ladd model. The first experimental results for a rectilinear channel were generated in 2007 by Di Carlo et. al. and confirmed the existence of 4 of the 8 Chun and Ladd equilibrium positions, the ones centered on each face of the channel cross section [53]. The major results from these early experiments were extensions of the Segré and Silberberg analysis to rectangular cross-sections that for such behaviors to occur the inertia of the fluid must be significant on the scale of the particles, or the particle Reynolds number must be approximately equal to or greater than 1.

$$\mathrm{Re}_P = \mathrm{Re}_C (a/D_h)^2 = \rho U_{Max} a^2 / \mu D_h \tag{2.2}$$

The other main result was the scaling produced for the channel length required to achieve such focusing behaviors as defined in Equation 2.3.

$$L_f = D_h/(f_L \mathrm{Re}_P) = \pi\mu D_h^2 / \rho U_{Max} a^2 f_L \tag{2.3}$$

Where f_L is a non-dimensional force dependent on the cross sectional location of the particle and the Reynolds number but whose average value for a channel of aspect ratios 2 to 0.5 (h/w) varies from ~0.02 to 0.05 [54]. The main implication of this paper was that it was the first application of inertial focusing to cells (blood cells) within microfluidics and truly jumpstarted an entire field.

These initial experiments were subsequently followed by the first direct numerical simulation for highly confined inertial focusing flows [55]. In this study it was discovered that the wall effect force and shear gradient force scaled differently with particle size.

$$F_{\text{shear gradient}} = f_L \rho U_{Max}^2 a^3 / D_h \tag{2.4}$$

$$F_{\text{wall effect}} = f_L \rho U_{Max}^2 a^6 / D_h^4 \tag{2.5}$$

The dependence of the non-dimensional lift force on Reynolds number has been investigated both numerically [49] and empirically [55, 56]. Though the inertial forces still increase in magnitude as Reynolds number is increased, the lift coefficient drops ($\propto \mathrm{Re_C}^{-0.5}$). Zhou and Papautsky's (2013) lift coefficient analysis also calculated a second, separate lift coefficient dependent on the rotation of particles for the motion of particles to the centers of the faces by investigating the effects of aspect ratio on the channel length required (residence time) to achieve focusing in opposite aspect ratio channels [56]. A dependence of the motion towards the walls of a^2 and across the walls to the center of each face of a^1 allows for the separation of particles by size through first focusing the

particles in one aspect ratio channel then changing the width thereby altering the force field in a manner to allow the larger particles to migrate to the new equilibrium position faster than smaller particles [57]. This behavior was investigated over a small range of Re_C values from 30 to 70. A similar concept has been used for the separation of bacteria from diluted blood, taking advantage of the lack of focusing of the smaller bacteria but focusing the larger blood cells [58].

At this time, the application of inertial focusing in microfluidics to the processing of biological samples prompted the study of different effects in such channels including the effect of both cell shape and deformability. The shape of a particle was found to have a minimal effect on particle migration, although the equilibrium position of a particle is proportional to its largest effective diameter [59]. These non-spherical particles were also found to rotate at a frequency dependent on their largest diameter. This was applied to the separation of fungal cells (Saccharomyces cerevisiae) based upon their shape, which is determined by the different stages of their growth cycle [60].

Non-rigid or deformable particles were also investigated with the motivation that cells are deformable objects. Initial testing with viscous droplets in microfluidics found that the equilibrium position moved further away from the walls of a channel with decreasing internal viscosity[61], matching previous theoretical results [62-64]. Different cancer cell lines were then tested in a similar device and it was shown that modified breast cancer cells, known to be more metastatic, equilibrated further from the wall than unmodified cells; in other words, the modified cells were more deformable (modMCF7 versus MCF7). This concept is now being utilized as a mechanical biomarker for the detection of cancer and sepsis and other diseases [65].

One of the other interesting aspects of Di Carlo's discovery in 2007 was that the particles not only migrated to an equilibrium position in the cross section but also ordered longitudinally in the direction of the axial flow [53]. The cause behind this spacing was found to be a hydrodynamic interaction between particles in which stable uniform motion was achieved after an oscillatory interaction between particles [66]. This spacing was also investigated in wider channels where multiple particle trains formed with a longitudinal spacing of approximately 2 particle diameters at a particle Reynolds number of approximately 1 [67, 68]. For many biological measurements, including cytometry, this kind of ordering is extremely useful. Current technologies utilize sheath flows that surround the sample flow in order to space cells and particles out evenly for more accurate counting. By taking advantage of inertial focusing it is possible to have particles aligned and ordered without the requirement of sheath flows and the associated reduction in sample flow rate [69-71]. This ordering has also been used for the improvement of encapsulation efficiencies by matching the frequency of cell ordering and the production of droplets [72, 73].

Another intriguing measurement was of the rotation of inertially focused particles. While shown theoretically to not have a significant affect on the overall migration of the particles, the rotation rates in a microfluidic system were measured to be in the kilohertz range [55]. This rotation changed with increasing particle aspect ratio for non-spherical particles, which followed Jeffery orbits with a period proportional to the particle aspect ratio [60]. Furthermore, this rotation induces a secondary flow found to cause mixing across the channel that increases as the particle fraction was increased in the channel [74].

Other investigations have looked into the effect of discontinuous walls. In this way, it was hoped that the equilibrium positions would be altered by the removal of the wall leaving only the shear gradient lift. As it turned out, the manner in which this was accomplished led to the size selective trapping of cells in the regions where the walls were moved further away. Essentially, when inertially focused particles entered a section of channel where the sidewalls moved away sharply, at sufficient Reynolds number and depending on the size of the side chambers, separation of the flow would occur. This separation of the flow caused vortices to form in the side chambers. When this occurred the velocity gradient in the center stream of the channel barely changed allowing for the shear gradient lift force in the absence of the walls to force particles, by size ($\sim a^3$), towards these vortices. Depending on the initial focused position of the particles and the strength of the shear gradient lift, the larger particles would migrate into the vortex regions and become trapped. These cells stay trapped until the flow rate was decreased to a point where the vortices are no longer formed. This concept as been applied for use as a cell staining platform [75], the isolation of large cells from a mixed sample [76] and for enhancing the electroporation and vector delivery processes for transfection of cells with notably increased viability of cells post-processing [77].

2.3 Secondary Flow Assisted Inertial Focusing

Two major limitations for the application of inertial focusing in straight channels to biomedical problems were the existence of multiple equilibrium positions and that the lateral forces across larger channel dimensions become weaker as the velocity profile becomes blunted [78]. This velocity profile leads to inefficient focusing in wide straight channels as the aspect ratio is increased or decreased from h/w=1, requiring unrealistic

channel lengths to provide a long enough residence time for the forces to cause all particles to migrate to the center vertically mirrored positions as shown in Figure 2-2a.

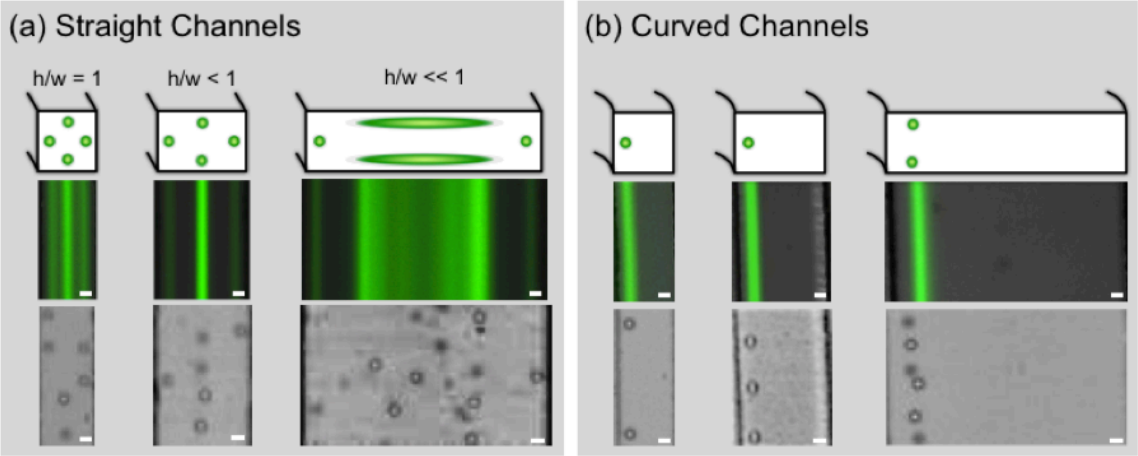

Figure 2-2: Schematics showing the theoretical cross-sectional equilibrium positions for (a) straight and (b) curved channels of equivalent aspect ratio (h/w = 1, 1.5, 4, respectively) with the corresponding overhead fluorescent streak images and high speed video stills (Some images stitched to show all equilibrium positions not all shown in a single image). All images taken 6cm downstream from the inlet of the devices at an average downstream velocity of ~1 m/s. Scale bars are 10μm.

The most utilized method of overcoming these issues is the addition of a secondary flow that adds a drag force on particles suspended in the channel. This drag force improves the lateral motion of the particles and also adjusts the states of the equilibrium positions. Different means of generating secondary flows have been investigated including asymmetric periodic structures on straight channels [79-83], however, the most common way a secondary flow has been generated is through the addition of curved channels.

The addition of curvature to microfluidic channels at low Reynolds number simply increases the length of the channel. However, in a finite Reynolds number regime with inertia, curvature allows for the addition of a secondary flow known as Dean flow [84-87]. Initially, described by William Dean in 1928, Dean flow is formed due to the inherent velocity differences in the channel cross-section (parabolic flow – fluid in the center of the channel moves faster than fluid near the walls). The additional momentum

carried by the fast moving fluid in the center of the channel carries it towards the outer wall of the channel curvature as it enters a curve. Due to conservation laws, this generates a recirculation of fluid towards the center of the channel curvature along the top and bottom surfaces of the channel as depicted by the black vectors in the right schematic of Figure 2-3 where the flow is into the page.

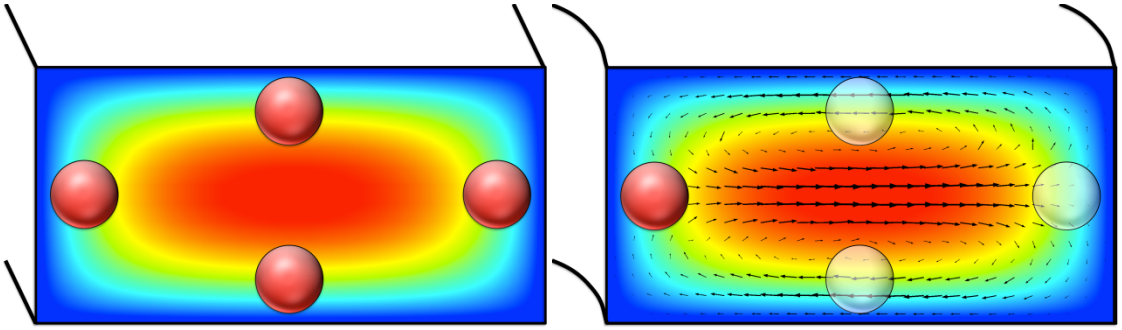

Figure 2-3: Velocity profile in a straight channel (left) with the equilibrium positions highlighted and the velocity profile in a slightly curved channel with vectors representing the Dean flow caused by the curvature of the channel. The red particles show the stable equilibrium positions and the transparent particles are indicative of the stable positions in a straight channel made unstable under the correct conditions in a curved channel. Axial flow is into the page.

The strength of the secondary flow in a curved channel, characterized by the non-dimensional Dean number, is dependent on the cross sectional shape, Reynolds number of the flow, and the curvature of the channel [84, 85, 88].

$$De = \mathrm{Re}_C (D_h/2r)^{1/2} \tag{2.6}$$

Both alternating curves and spirals have been investigated for the generation of Dean flow in conjunction with inertial focusing of particles [53, 89]. The additional force imparted by this flow is normally assumed to follow the Stokes' drag relationship defined in Equation 2.7. This assumption is usually made for $\mathrm{Re}_P<1$, however, since the secondary flow velocities are only a fraction of the axial flow, which was used to define the particle Reynolds number in Equation 2.2 this threshold should not be breached in terms of the secondary flow.

$$F_{\text{Dean Drag}} = 6\pi\mu a U_{Dean} \tag{2.7}$$

Under the effect of sufficient Dean flow, the equilibrium position at the center of the top and bottom of a channel cross section become unstable, as well as the position at the outer wall, further from the center of curvature due to the impingement of the secondary flow on particles. This leaves a single lateral equilibrium position at the inside wall of the curve as seen in Figure 2-2b experimentally and Figure 2-3 schematically.

The majority of researchers found a small range of conditions through trial and error to achieve 'good' focusing in curved channels. Di Carlo found that the ratio of inertial lift to Dean drag specified the existence of this working regime (R_f~1) [89, 90].

$$R_f = {F_L}/{F_D} = \frac{\rho G^2 C_L a^3}{3\pi\mu U_{Dean,Avg}} \tag{2.8}$$

While the dynamics of inertial focusing have been proven to be significantly dependent on size, the eventual equilibria in a straight channel are usually collocated or in very close proximity. Dean flow offers an opportunity to provide separation based upon size due to the dependence of the drag force on size, a, and the direction of the Dean flow at the mid-height of the channel being opposing the shear gradient lift force that scales with a^3 [55]. This type of separation depicted in Figure 2-4 therefore scales with ~a^2 and is the one of the most utilized applications of inertial focusing to date [90, 91].

Separation in curved channels was shown in the early inertial focusing papers for particles of different sizes and blood cells. The flows in asymmetrically curved channels were more complicated, but based upon the same mechanism [89]. Spiral geometries have also been used for separating nucleated cells from blood [92, 93] including the

separation of CTCs (circulating tumor cells) from diluted blood samples [94-97]. Similarly, cells have been concentrated by collecting the cell rich and cell free streams separately in curved channels [98, 99].

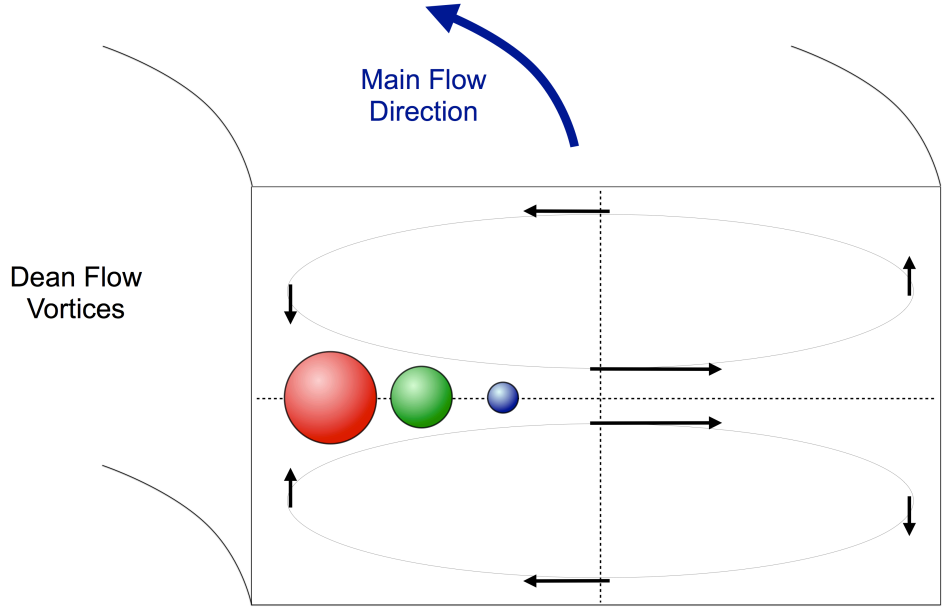

Figure 2-4: Conceptual separation of particles through the balance of Dean drag (directed with Dean vortex vectors) and Inertial lift directed from the center towards each wall. The particles should separate according to a^2.

Several different versions of separation have been detailed utilizing inertial focusing in curved channels depending on the balance of the strengths of the Dean flow on differently sized particles. At low Dean numbers, larger particles have been shown in certain aspect ratio channels to focus to the centerline of the width as if the channel were straight while smaller particles with smaller magnitude inertial forces are pushed to towards the inner wall of the channel [92, 95]. If correctly designed at a high enough Dean number using a co-flow of two solutions, the large particles from one fluid will be trapped by inertial forces but the fluids will completely swap if diffusion is also minimized [100]. The most recent papers studying these Dean flow assisted inertial focusing have found a continuum of behaviors and particle equilibrium positions which

change with flow rate [92, 99]. However, this continuum of behaviors is unsatisfactorily justified using the same ratio of forces as the early inertial focusing papers.

2.4 Breakdown of Inertial Focusing Literature

Looking at the summed knowledge in the literature about inertial focusing you can see a trend emerge when you classify each by the type of channel used; Straight, straight but structured with secondary flow and curved with secondary flow. These groups of articles were then sectioned by the type of results presented, from applied where an article presented a biomedical application of inertial focusing, to experimental where data using non-biological materials were presented to theoretical improvements justifying new definitions of forces or flows. Many articles were both theoretical and applied and were distinguished as such. While the majority of applications are in curved channels there is a distinct deficiency of theoretical development for the same devices, necessary to understand the physics and thereby predict inertial focusing behaviors, as shown in Figure 2-5.

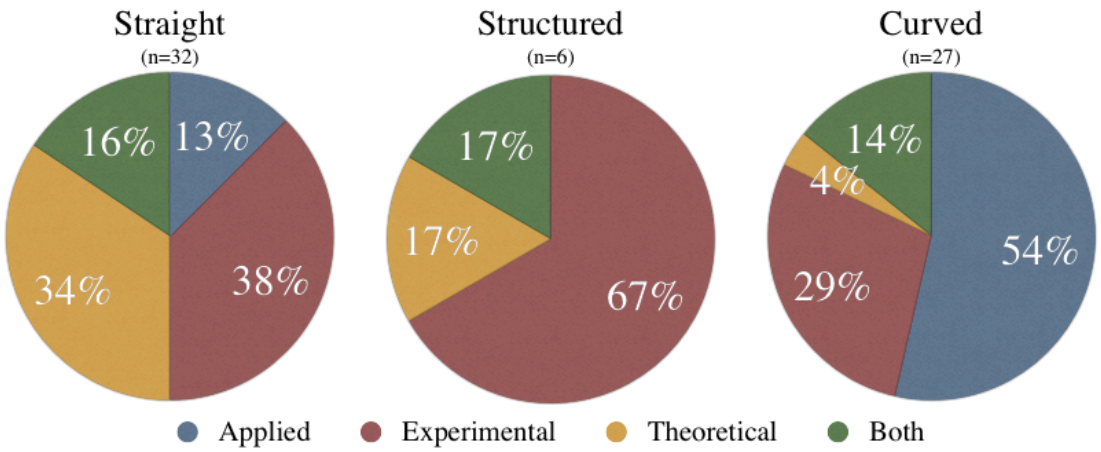

Figure 2-5: All inertial focusing published papers since 2006 segregated by the type of channel used and by application versus theoretical.

Of course this trend is understandable as simplified systems are more likely to understood from a theoretical point of view than more complex ones. However, the

current and future application development being so centered on curved channels clearly indicates the importance of these flows. The desire to better predict experimental outcomes in such channels and develop new biomedical applications of inertial focusing is the main impetus for this dissertation.

Of the shortcomings of the current understanding of inertial focusing in curved channels, one critical, initial question that guided the investigations of this dissertation was the assumption of a single equilibrium position at the mid-height of the channel. When investigated under certain conditions dual mirrored height locations were found rather than a single position as in Figure 1.2b in the widest spiral device. If so, what is the actual scaling for this type of separation and can it be predicted for different applications?

Chapter 3

Experimental Methods

3.1 Overview

This chapter will present the designs, fabrication techniques, operational details and analysis procedures utilized for gathering the data presented in Chapters 4 through 6. The major contributions described in this chapter are the automated image analysis programs developed, new data presentation methods and the development of a fabrication technique for rigid microfluidic channels.

3.2 Channel Design

3.2.1 Width Controlled Spirals (Chapter 4)

The devices used in Chapter 4 were designed by setting an average radius for each consecutive turn that was kept constant for all of the different channel widths. These radii were chosen based on geometric requirements for the inlet and outlet as well as having at least 1.5 times the maximum channel width (600μm) in bonded linear distance between adjacent curves. Full 180º sections of curvature were added to a shorter first turn needed to have enough bonded area around the inlet. The turns were added until the pattern was approximately 6cm long. The device design as well as the turn radii and their corresponding Reynolds and average Dean number values for each different width device can be found in Figure 3-1. Small triangular markers were placed along the channel at regular angular intervals of 20° starting with turn 2. These were used for accurate image acquisition at the specific distances along the channel.

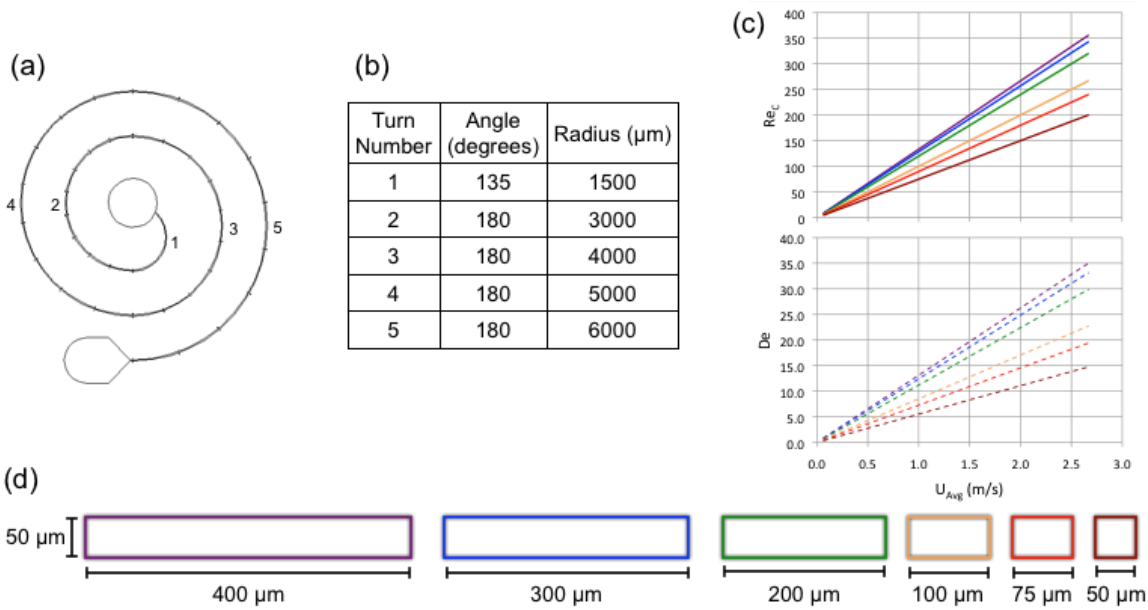

Turn Number	Angle (degrees)	Radius (µm)
1	135	1500
2	180	3000
3	180	4000
4	180	5000
5	180	6000

Figure 3-1: This is (a) a schematic of the device design and its (b) dimensions. The (c) channel Reynolds number and average Dean number are given as a function of average downstream velocity. Each line represents a different channel width increasing from bottom to top (50µm bottom line to 400µm top line). (d) Cross sectional views of the channels utilized are also shown [78].

3.2.2 Dean Number Controlled Channels (Chapter 5)

The designs of the microchannels for independently investigating the effects of Reynolds and Dean number on inertial focusing behavior are presented in Figure 3-2. As Dean number is linearly dependent on channel Reynolds number (Equation 2.6) and altering the cross sectional dimensions of a device also changes the particle confinement ratio, the radius of curvature was chosen for adjusting Dean number. Five different channel designs were created over a broad range of curvature values from the tightest spiral possible to a straight channel. The smallest spiral design was determined by the inlet port size (~1200µm diameter) and requiring a minimum distance of a single channel width (100µm) between consecutive lanes of the spiral to ensure bonding. The cross section of each channel is 100µm wide and 50µm high and the length kept constant at 4cm. The cross sectional dimensions were chosen as a particle of an approximate diameter of normal cells (8-15um in diameter) are all above the stated a/D_h threshold of

0.07 [54]. These different channels are referred to by their curvature ratio, $\delta=(D_h/2r)^{0.5}$, or the square root of the ratio of the hydraulic diameter (D_h) to twice the average radius of curvature (r). This is the Reynolds number independent component of the Dean number. The flow rate applied to these devices was varied from 25µL/min (U_{Avg}=0.066m/s) to 1200µL/min (U_{Avg}=4m/s).

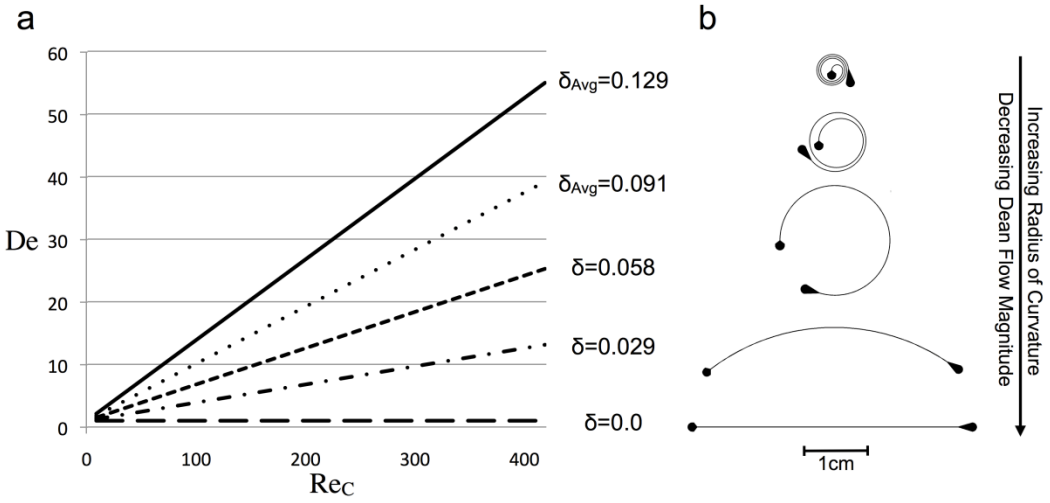

Figure 3-2: This figure presents (a) the Dean number to channel Reynolds number ratios for the five different channel curvature values, (b) schematics of the different channel designs.

The exact dimensions of these devices are given in Table 3-1 where each turn has an arc angle of 180° unless otherwise stated. Small triangular markers were also used in these designs at an interval of 1mm along each channel.

3.2.3 Filters

No on-chip filters were incorporated into these designs, as they would have increased the initial diameter allowed for the first turns of the smallest spiral designs. However, it is recommended that filters be used in any device to be used with biological specimen.

Table 3-1: This table contains the dimensions for the different curves and their length averaged value used to describe the curvature ratio for the entire device. Each turn is 180° long unless otherwise stated.

Device Name	δ=0.129	δ=0.091	δ=0.058	δ=0.029	δ=0
Turn 1	850	3387	9886	39723 (74.102°)	∞
Turn 2	1700	4087	10086 (114.75°)		
Turn 3	1850	4287			
Turn 4	2000	4687 (139.334°)			
Turn 5	2150				
Turn 6	2300				
Turn 7	2450 (172.318°)				
Length Averaged Radius (μm)	2007	4014	9931	37923	∞

3.3 Fabrication

3.3.1 PDMS Microchannels (Chapter 4)

Standard SU8 photolithography and soft lithography were used to fabricate the positive master mold and the polydimethylsiloxane (PDMS) microchannels respectively. Briefly, negative photoresist, SU8-50 (Microchem Corp, Massachusetts), was spun at 2750 RPM to a thickness of approximately 50μm, exposed to UV light through a mylar emulsion printed photomask (Fineline Imaging, Colorado) and developed in BTS-220 SU8-Developer (J.T. Baker, New Jersey). A 10:1 ratio mixture of Sylgard 184 Elastomer base and curing agent (Dow Corning, Michigan) was then poured over the raised mold, degassed, then allowed to cure in an oven at 65°C for 8 hours and then removed from the silicon/SU8 master. Inlet and outlet holes were punched using custom sharpened needle tips. The devices were then cleaned of particulate using low-residue tape and oxygen plasma bonded to pre-cleaned 1mm thick glass microscope slides. Due to the high driving pressures required for the smaller channels (50 and 75μm widths), 0.06 inch outer

diameter Tygon tubing (Greene Rubber, Massachusetts) otherwise press fit into the inlets and outlets were chemically bonded to the PDMS using Loctite® Medical Grade epoxy.

3.3.2 Rigid Epoxy Microchannels (Chapters 5 and 6)

The microfluidic channels used in the studies described in Chapters 5 and 6 utilized devices fabricated in rigid epoxy without minimal measurable deformation at high pressures (up to 1000psi) and an extreme pressure rating of 6000psi (pump maximum). The importance of the constant cross sectional dimensions along the length of the devices cannot be understated as the deformation of PDMS channels can significantly alter the flow conditions over a large fraction of the channel length [101-103].

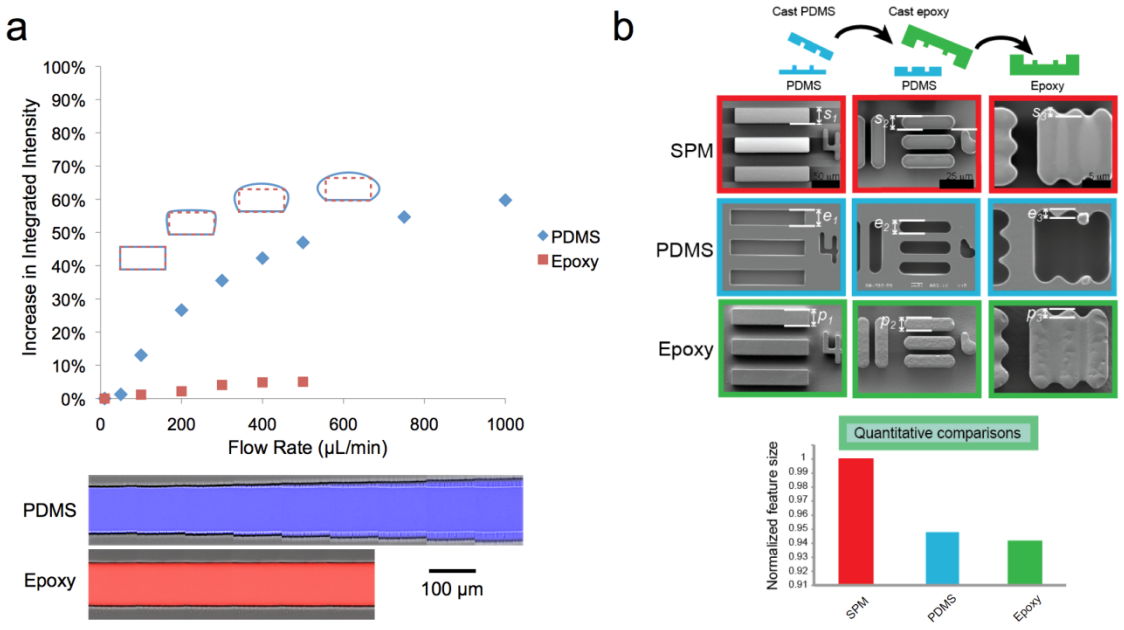

Figure 3-3: (a) Relative deformation of PDMS and Epoxy microfluidic channels (100µm wide by 50µm high) measured using the relative increase in intensity of a fluorescence line scan across the channel at increasing flow rates. A montage of brightfield images with the overlaid fluorescence data is given underneath the plot as well as (b) the replication fidelity of the epoxy fabrication process on the right.

The expansion of the PDMS channels alters the balance of Dean drag and inertial lift forces as the larger cross sectional area leads to a higher Dean flow magnitude and decreases the overall flow velocities and therefore shear gradients in the channel. Figure

3-3 presents the relative deformation of PDMS channels and rigid epoxy channels of equivalent dimensions and the replication fidelity of the fabrication process.

The fabrication of rigid epoxy microfluidic devices starts with unbonded PDMS channels created using the same process described in the previous section. One addition to the design for devices to be fabricated in rigid epoxy is the use of donut ports. These donut ports require a second layer of thick SU8 (300-800μm – exposed for 90 seconds), and a new mask with alignment marks to expose the donuts located at the inlet and outlet of each device where holes are normally punched for PDMS devices. These donuts have an inner diameter of 720μm and an outer diameter of 1200μm.

The PDMS channels with donut ports were then used as a template for creating a flexible mold for the rigid material. This was accomplished through the passivation of the channel surface through vapor silanization with tridecafluoro – 1,1,2,2 – (tetrahydrooctyl) trichlorosilane (Gelest). First, the PDMS templates were exposed to an oxygen plasma (50 watts, 3% oxygen for 30 seconds) then placed in a dedicated vacuum dessicator with 100μL of the silane. The treated templates were removed after 15 minutes and placed channel side up in a petri dish at least 1cm from any edge of the dish. Care should be taken not to touch any of the channel surface of the PDMS template during the transfer of the templates. Approximately 110 grams of uncured PDMS at a 10:1 ratio was mixed and poured on top of these templates. The uncured PDMS should reach at least 1mm but no more than 3mm above the channel side of the silanized templates. A blank, unpatterned, wafer was also covered with PDMS at this stage to be used as a flat surface for coating glass slides with epoxy. Both dishes were degassed, cured overnight at 65°C and then the entire slab containing the mold templates was removed from the petri dish whole. The

PDMS was cut off of the other unpatterned wafer approximately 1mm from the edge of the wafer and this PDMS slab was saved flat side up in a separate petri dish. The templates were then delicately removed from the slab and discarded leaving the PDMS molds. Any devices that have marks from transferring issues, incomplete silanization or bubbles were discarded at this stage. The molds were then separated from one another using a knife. Holes were then punched in the donut ports using the 0.75mm Harris Uni-Core biopsy punch. These molds were then stored at ambient conditions until needed.

Next, PEEK tubing (1/16 inch outer diameter × 0.030 inch inner diameter) was cut to 14-inch lengths and roughened on one end with coarse sandpaper up to 2 inches from the end. This roughening was done to increase surface area adhered to epoxy material. Teflon coated wire with an outer diameter of 0.028 inches (16 inch long sections) were then inserted into the PEEK tubing. About 1mm of wire should extend out of the roughened end of the PEEK tubing.

At this stage the Epoxacast 690 (Smooth-On) was mixed per the manufacturer's instructions (approximately 5 grams total per device to be made). The two components were mixed and degassed for 30 minutes along with the PDMS molds and PDMS slabs. This step significantly reduces the number of bubbles formed on the devices during curing. After 30 minutes, the molds were first removed from the vacuum desiccator and the tubing assemblies were inserted into the inlet and outlet punched holes taking care not to press more than 1mm into the donut port and mold (a full press fit will deform the channel surface). Note: Tygon tubing can be used for lower pressure applications and only requires a small plug of Teflon wire press fit into both the end of the tubing and the mold itself. It was sometimes necessary to secure the PEEK tubing in an upright position

(tape to a taller item) to prevent it from falling over. Once a mold had both inlet and outlet tubings inserted and secured, approximately 2mL of mixed epoxy was bulb pipetted into the mold until the top surface of epoxy was even with the top of the mold. This was repeated for all device molds. To prepare epoxy coated glass slides, a degassed PDMS slab was placed flat side up on a working surface. A small amount (<1mL) of epoxy was pipetted onto this surface in a T shape. A clean glass slide was then slowly lowered onto this epoxy starting with one end of the slide on the wide side of the T-shape. Care should be taken to minimize the number of bubbles trapped under the glass slide. Both the devices and slides were allowed to cure for 28 hours after mixing.

At 28 hours after mixing, the epoxy coated slides were separated from the PDMS slabs and placed glass down on a hot plate at 55ºC. The partially cured devices were cooled in a minus-20ºC freezer for 3 minutes in order to reduce deformation during mold separation. The teflon wire was pulled out of the end of the PEEK tubing away from the devices (or carefully from the bottom of the device if Tygon tubing was used). The devices were then removed carefully from the molds and pressed gently against the epoxy side of the heated coated glass slides. Slight pressure was applied to the bottom of the glass slide and top of the epoxy device to ensure bonding. The devices should then be allowed to fully cure for another 24 hours before use. This process is briefly summarized in Figure 3-4. A full procedure and images for the process of fabricating rigid microfluidic device is available in Appendix A.

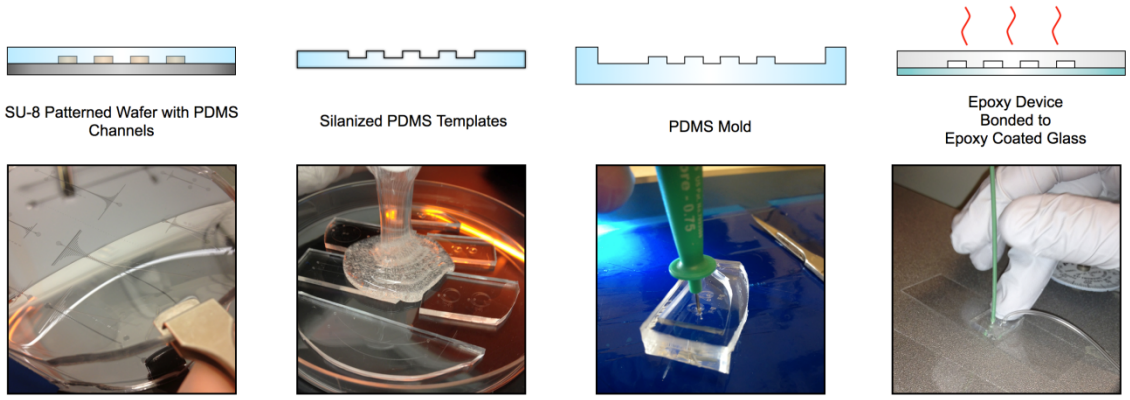

Figure 3-4: Images and process schematic for production of rigid epoxy microfluidic devices.

3.4 Particle Suspensions

For the experiments in Chapter 4, a 250,000 beads/mL (0.013% v/v) solution were created using Thermo Scientific 10µm diameter green fluorescent aqueous microspheres (ρ_P = 1.050g/ml) added to a solution of equivalent density comprising 5.4 parts deionized water (ρ_W = 1.000g/ml) and 1 part Iodixanol (Optiprep density gradient solution, ρ_I = 1.32g/ml) (Sigma-Aldrich). Tween 20 was added to prevent particle aggregation at a volume percentage of 0.1%. This suspension was mixed and filtered using Beckton Dickinson 40µm Cell Strainers to remove large PDMS debris and any dust particulate. These solutions were then loaded into plastic syringes and injected into the devices using a Harvard Apparatus PHD Ultra syringe pump. The devices were primed with a 1% v/v Tween 20 solution in deionized water prior to each experiment.

For the experiments in Chapters 5 and 6, water based solutions with 0.1% Tween 20, 0.01% fluconazole (antifungal) and 0.01% penicillin-streptomycin (anti-bacterial) were density matched to polystyrene beads using iodixanol (Optiprep, Sigma-Aldrich) to a final fluid density of 1.05g/mL. Polystyrene beads (4.4µm DAPI-fluorescent, Polysciences, 9.9µm FITC-fluorescent, Thermo-Scientific, and 15µm, TxRed-

fluorescent, Invitrogen) were washed and resuspended in the density-matched solution at a length fraction of 0.1 (0.021%v/v, 0.103%v/v, and 0.230%v/v respectively). Stainless steel syringes (Cole-Parmer) and a high-pressure Harvard Apparatus XPSI syringe pump were used to drive flow through devices (up to ~1000psi).

3.5 Image Acquisition

3.5.1 Fluorescent Streak Imaging

Using an automated Nikon TiE inverted microscope with a Retiga 2000R monochromatic camera, multi-position long exposure streak images were taken at 38 different positions along each spiral microchannel using Nikon NIS-Elements AR 3.10 software. Exposure times were varied to account for the magnification being used and the number of events per second at a given flow rate for each device ranging from 250ms to 3s. Three consecutive images were taken at each position at each flow rate then averaged together. Approximately 30 seconds were allowed between each flow rate for pressure stabilization. Each averaged fluorescent streak image gathers positional data from over 1,000 individual particles.

3.5.2 High Speed Imaging

A Vision Research Phantom v4.2 high-speed camera was utilized with a Lumen 200 mercury arc lamp. The maximum frame rate with an exposure time of 2μs was always utilized for a given image size. For a 512 by 256 pixel image this frame rate was 4400 frames per second.

3.6 Data Analysis

3.6.1 Streak Position and Width Measurement

After fluorescent streak images were collected three images from each position and flow rate were averaged together. These averaged images were filtered first using a median filter then using a large radius top-hat filter to remove background variation. Outliers were then removed by resetting saturated pixels to zero. At this point, five separate cross sectional lines were drawn digitally by hand across the image from inside wall to outside wall of the channel. These lines were used to collect five different intensity profiles.

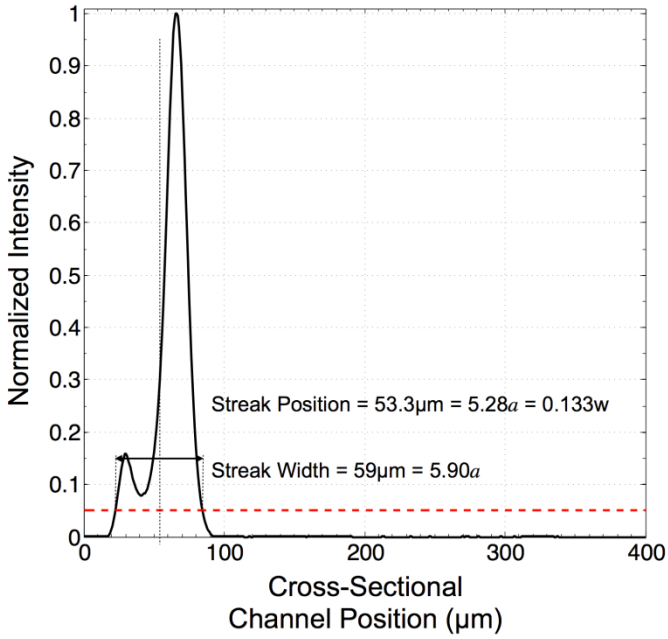

Figure 3-5: This figure shows the intensity profile from a 400 μm wide channel with 9.9 μm beads in a PDMS device above the breakdown flow rate at the outlet. The streak width and position are labeled at the 5% of the maximum intensity threshold used for this type of analysis.

These intensity profiles from each position along the channel were then used to calculate the streak width and position. Streak width was determined as the greatest lateral distance between intensity values above 5% of the maximum intensity of that specific intensity profile as shown in Figure 3-5. A 5% threshold was used so that lower intensity streaks missed by a standard full width at half maximum analysis were able to be detected as the intensity profiles were not purely Gaussian in nature when these extra

streaks were visible. Streak position was determined as the center location of the streak width also shown in Figure 3-5. The streak width and position was then averaged between the five different intensity profiles to minimize the effect of any local intensity variations or temporal fluctuations in the streak behavior as well as minimize user error from the drawn cross sectional lines.

3.6.2 Straightened Image Generation

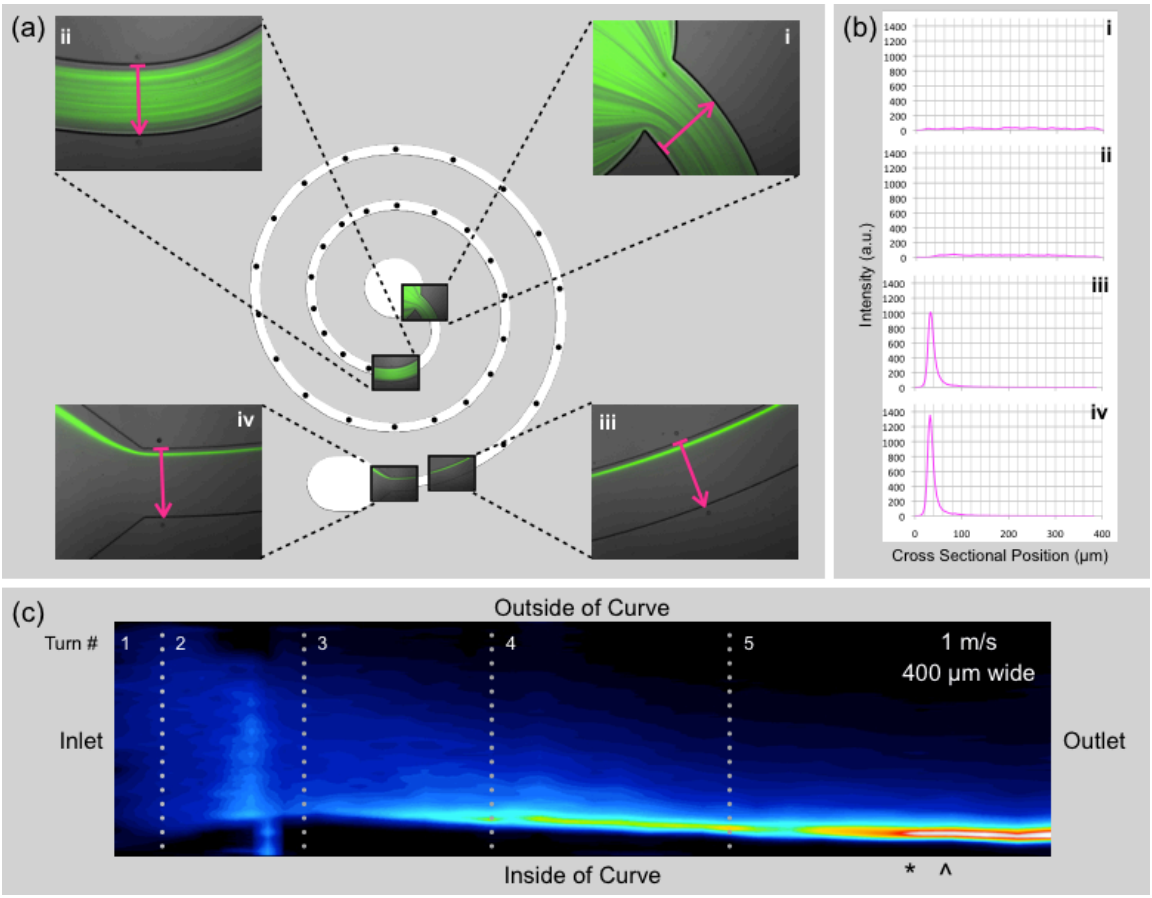

Figure 3-6: (a) A device schematic with imaging positions marked by dots along the channel with the first and last two positions highlighted with the actual images and the cross sectional lines used to generate (b) the intensity profiles which are then stacked, smoothed and converted to (c) image form, effectively a straightened image of the focusing behavior in the spiral device which is labeled with points of importance separating the different behavior regimes (* Focusing Achieved, ^ Point of Closest Wall Approach). There is no breakdown in this example image. The dotted lines demarcate where the channel curvature changes or, in other words, the interface between turns [78].

To investigate and compare the dynamics of inertial focusing behavior between different width devices it was necessary to create a representation of the focusing

behavior along the channel. This was accomplished by stacking the intensity profiles from 38 longitudinal imaging positions and converting the resulting matrix to an image format which was smoothed and scaled in each dimension separately accounting for the increasing spacing between imaging positions along the channel and for the different channel widths.

Figure 3-6 shows the steps for generating a straightened image with (a) example positional images, (b) intensity profiles and the (c) resultant straightened image for a 400 μm wide device at an average downstream velocity of 1 m/s.

3.6.3 Re_C Map Generation

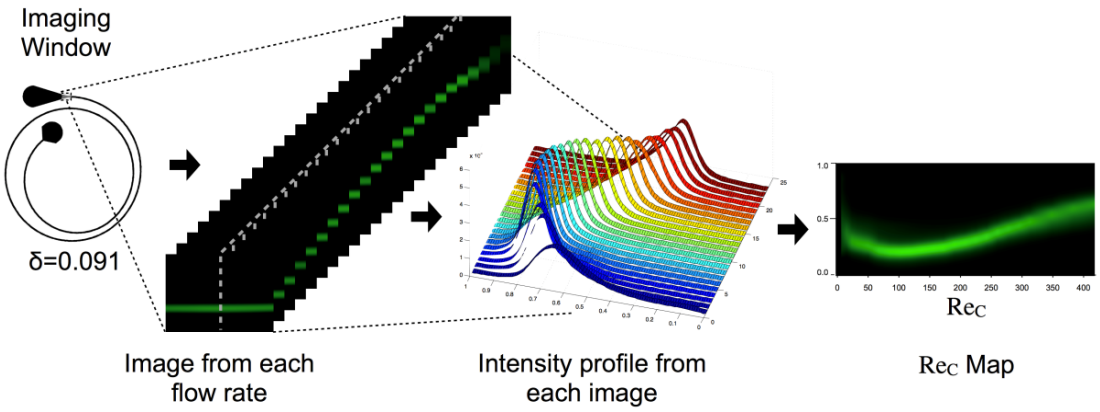

Figure 3-7: Re_C map generation process (left to right). Fluorescent streak images are captured at the same position of a device as flow rate is changed. One averaged image for each flow rate is created and then three intensity profiles across the channel width are measured and averaged together. One intensity plot per flow rate is saved in a matrix and then scaled, smoothed and saved in an image format. These intensity plots are the same that are used for measuring streak width and position as well as other parameters for the given flow conditions.

Results from a given device are also presented using Re_C maps [104]. These were compiled by taking intensity line scans at the outlet position of each channel at different flow rates. Each line scan becomes a column of pixels in the Re_C map showing the inertial focusing behavior at the outlet across a large range of Re_C values. The bottom of each Re_C map represents the inside wall of the channel closer to the center curvature (x/w=0) and

the top is the outside wall (x/w=1), further from the center of curvature. Figure 3-7 gives a graphical explanation for the generation of these plots.

3.7 Finite Element Simulation

3.7.1 Dean Flow Modeling

For Chapter 4, COMSOL Multiphysics finite element software was used to simulate the incompressible Newtonian fluid flow conditions within different aspect ratio channels. Each model was solved using the FGMRES iterative solver. The element size and quality was adjusted based upon computer memory restrictions and the actual volume of the model for each width. Maximum element size at the outlet was kept constant at 5 μm. An array of vectors for velocity was exported and then the average magnitude of the fluid velocity in the transverse direction to the channel, $U_{Dean,Avg}$, was calculated.

Computational modeling efforts for Chapter 5 were accomplished using COMSOL Multiphysics software using a 2D axisymmetric incompressible CFD model with swirl flow to obtain steady state flow velocities. As the resistance of a curved channel is higher than a straight channel a custom Matlab code was built in order to calculate the correct volume force required to achieve equal average velocities in each of the different curvature cases.

Computational modeling efforts for the measurement of inertial forces on a particle for Chapter 6 are described in that chapter.

3.8 Conclusion

Important advances in fabrication and automation of image analysis were essential for the completion of the following work on particle focusing in microchannels. These new means of obtaining more accurate focusing data and processing larger data sets allow for

the exploration of a greater number of parameters and distilling the results to a meaningful result in terms of the particle distributions across and along the microchannel dimensions.

Chapter 4

Dynamics of Inertial Focusing

4.1 Overview

This chapter details a comprehensive study of inertial focusing dynamics and particle behavior in low aspect ratio (h/w ~ 1/1 to 1/8) spiral microchannels. A continuum of particle streak behavior is shown with longitudinal, cross sectional and velocity resolution, yielding a large analyzed parameter space. The data set is then summarized and compared to prior results from both straight microchannels and other low aspect ratio spiral microchannel designs. Breakdown of focusing into a primary and secondary fluorescent streak is observed in the lowest aspect ratio channels at high average downstream velocities. Streak movement away from the theoretically predicted near inner wall equilibrium position towards the center of the channel at high average downstream velocities is also detailed as a precursor to breakdown. State diagrams detail the overall performance of each device including values of the required channel lengths and the range of velocities over which quality focusing can be achieved.

4.2 Introduction

This chapter presents an investigation of inertial focusing in spiral microchannels of varying widths providing missing pieces to the overall inertial focusing parameter space. The device designs are presented in Figure 3-1. They have the same central guideline but different widths. Overall, 6 different widths were tested from 50μm to 400μm. Width was chosen as a variable in order to vary the Dean flow magnitude and aspect ratio of the

channel while retaining the ratio of the particle size relative to the channel height. Figure 4-1 contains (a) cartoon representations of the flow conditions within curved microchannels of different widths, (b) the velocity profile for the main channel flow and (c) the secondary Dean flow velocity profile.

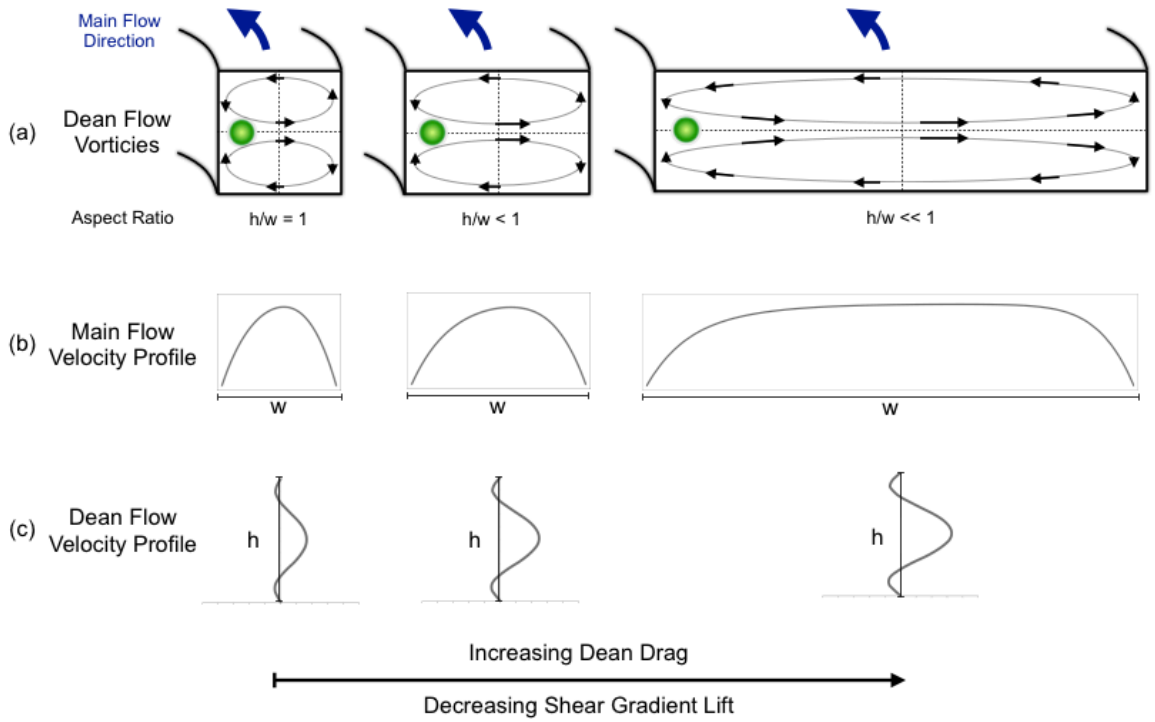

Figure 4-1: (a) Schematics of the different flow profiles and associated forces in curved channels of differing widths at inertial focusing velocities. Theoretical particle equilibrium positions are presented along with the directions and magnitudes of the secondary flow velocity (vectors and streamlines). (b) The main flow velocity profile at the center of the channel height or the horizontal cross section going into the page is given as well as (c) the Dean flow velocity (components tangent to the main channel flow) at the midline of the channel width or the vertical cross section. Note the slightly off center main flow velocity profiles are due to the Dean flow transferring the momentum of the faster moving fluid in the center of the channel towards the outer wall.

These flow profiles are representative of the competing mechanisms that affect inertial focusing behavior in curved channels and how each mechanism depends on the channel width at equivalent average downstream velocity. First, the inertial lift decreases as D_h increases, since the velocity profile becomes flattened and the shear gradient decreases as seen in Figure 4-1b. Next, the wall effect of the lift force has a more complicated dependence on D_h, but it is a shorter-ranged effect that is not the primary cause of

transverse particle motion across any of the channel widths [49]. Finally, the Dean drag on a particle increases with $D_h^{1.5}$ and becomes stronger as the width increases which is apparent in Figure 4-1c. At some critical channel width, the motion of particles across the channel will be dominated by Dean drag rather than inertial lift forces. This switch in dominant means of particle transport across the channel should become apparent in the focusing dynamics along the channel.

By direct visualization and measurement of inertial focusing behavior in such devices, it is possible to elucidate the underlying fluid physics. Expanding our understanding of inertial focusing in curved channels will assist in the development of basic design rules for future high-throughput biomedical devices. Moreover, the functional limitations of these devices and the driving mechanisms for inertial focusing in spiral microchannels can be understood by examining the dynamics at the device outlet as well as along each channel.

4.3 Outlet Behaviors

Inertial focusing behavior is routinely classified by the position and width of the particle distribution at the outlet of a device, where particles have been exposed to the inertial lift and Dean drag forces for the longest amount of time. Figure 4-2 presents the raw images at the outlet of each of the devices over a select range of flow conditions. A cross-sectional view of each spiral device is given on the left with adjacent brightfield images of the outlet of each device. The same imaging position was used for the next four fluorescent streak images at different average downstream velocities increasing from left to right. In each fluorescent streak image the flow is from left to right into the diverging section where the outlet tubing opening is located. In general, the devices exhibit similar

trends, with a critical threshold velocity for inertial focusing that scales as ~$1/D_h$. This inertial focusing behavior tends to remain stable over some range of flow conditions, which is consistent with prior results [54].

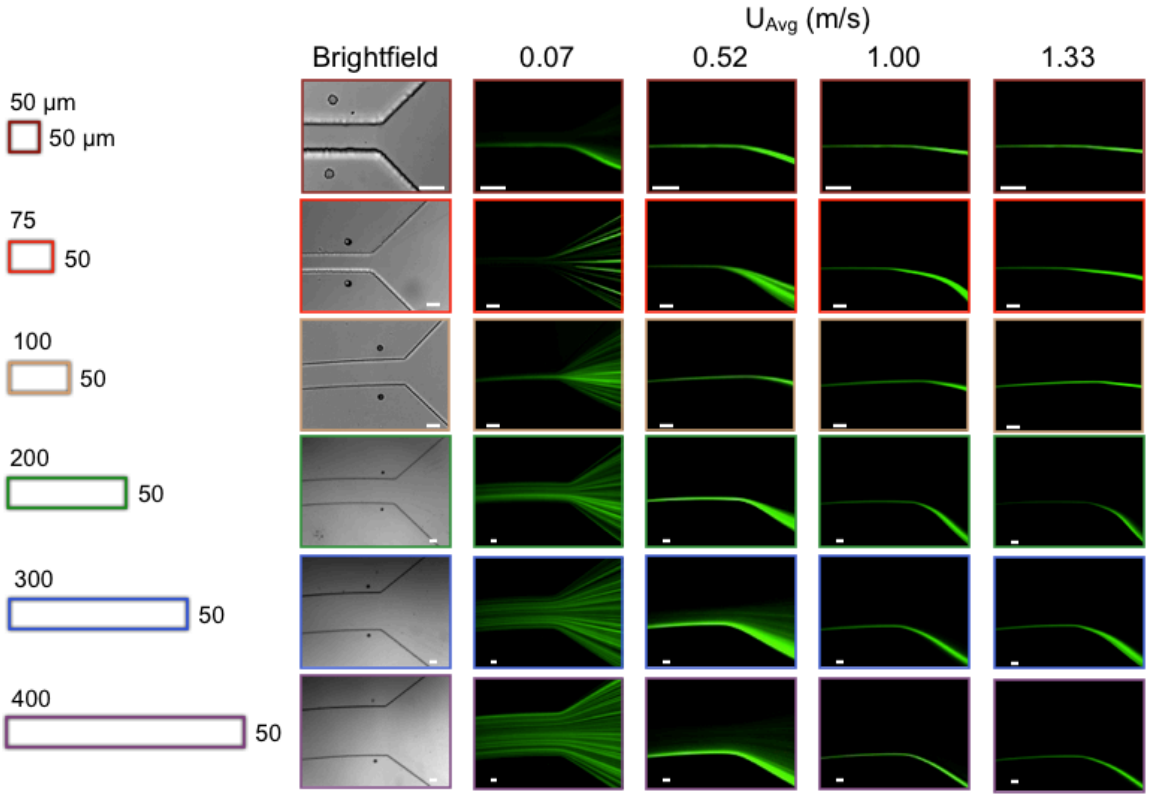

Figure 4-2: Brightfield and fluorescent images of the outlet of each device at select flow conditions are grouped by channel width (horizontal) and flow rate or image type (vertical). Cross sectional views are given for comparison (left). Image scale bars are 50µm. Note that these images were acquired at different magnifications to optimize spatial resolution, so the channel sizes appear to be similar in the images.

Although these images are helpful for qualitatively visualizing trends at different U_{Avg} and channel widths, they not sufficient for assessing more subtle quantitative differences in streak width and position. Thus, these values were measured from the images in Figure 4-2 and other similar ones for all channel widths and velocities. The results of these measurements are presented in Figure 4-3 where both streak width and position normalized by particle diameter are plotted versus the average downstream velocity. These plots show streak width on the left (b) and streak position within the channel cross section on the right (c) measured from the inside wall of each curve. Each

point on the plots describes a single measurement at the outlet of a device at a given downstream velocity. The points are grouped by channel width (color and marker style). In order to investigate the parameter space further with the same devices, each was run backwards from largest radius to smallest radius turn, in other words, increasing in Dean number, whereas the previously discussed cases describe a decreasing Dean number situation.

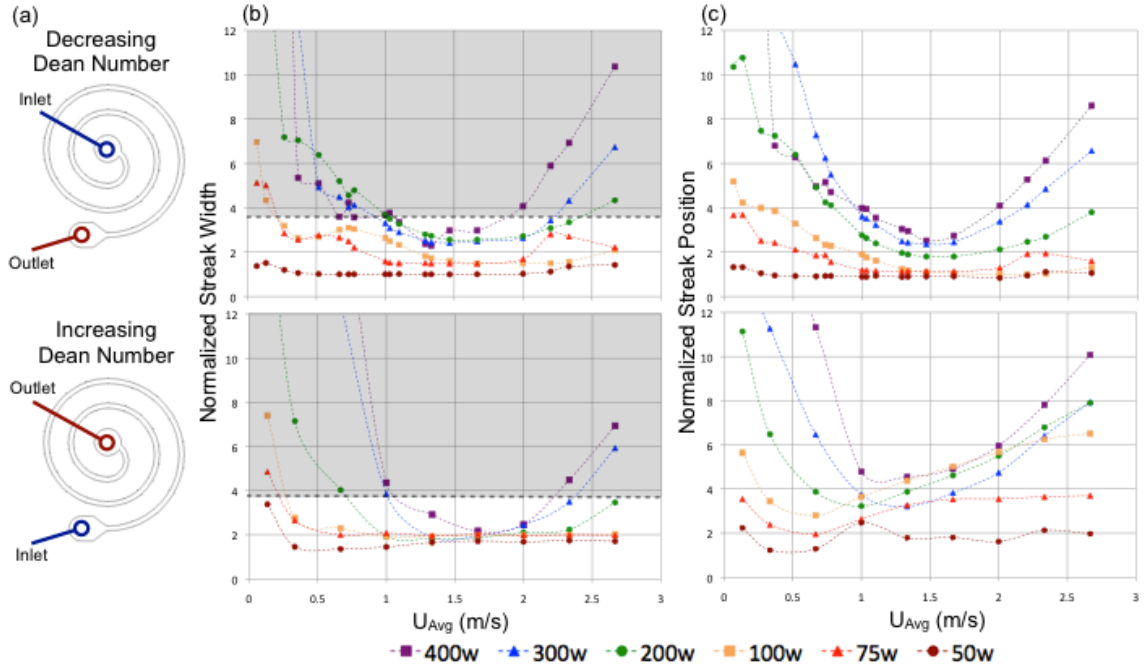

Figure 4-3: Device schematics (a) with arrows indicating the difference between the increasing and decreasing Dean number cases (inlet and outlet reversed). Quantitative comparison of normalized streak width (b) and normalized streak position (c) or the distance from the inside wall normalized by the particle diameter for cases of both decreasing (top) and increasing (bottom) Dean number along the device. The gray area indicates that the streak width is greater than 3.8 particle diameters at the 5% threshold.

The top row of plots in Figure 4-3 present the results from the decreasing Dean number case and the bottom row presents the increasing Dean number case results. Since the plots are only describing outlet behavior the main difference between the two cases at the same average downstream velocity is the instantaneous Dean number at the position of measurement. The history of Dean flow along the device may also have an effect on the outlet behavior but since the overall behavior was quite similar it was believed that the

upstream flow field had a greater effect on focusing dynamics rather than the outlet behavior.

The quantitative measurement of streak width and position in Figure 4.3 reveals that the stable range of inertial focusing is narrower for the wider devices, as the streak tends to shift away from the inner wall at higher average downstream velocities in the wider devices. The streak movement away from the wall has been previously observed and explained through Dean drag increasing faster than inertial lift at higher Reynolds numbers due to a decreasing lift coefficient [49, 90, 104]. Unexpectedly, at much higher downstream velocities (2 m/s) in the wider devices, the focusing behavior breaks down causing an increase in streak width. There is also a strong correlation between streak position and width, since the minimum streak width occurs at or near the closest approach to the wall. This result can be explained by the dominance of inertial lift forces, which vary most strongly at the equilibrium positions and would cause tighter focusing when this position is close to the wall. Finally, it should be noted that the Dean flow will alter the velocity profile across the channel, but the Dean flow velocities are considerably slower near the equilibrium positions than they are elsewhere in the channel cross section. As a result, inertial lift forces should dominate the behavior.

When comparing the outlet behavior between decreasing and increasing Dean number cases, presented in Figure 4-3, the streak width and position generally follow the same trends but exhibit several key differences. First, for the increasing Dean number case, the streak position shifts towards the center of the channel and the magnitude of this shift grows with increasing downstream velocity. The shift in streak position is similar to data for a 500μm wide spiral device in the literature although the constant and linear streak

position versus Dean number relationships separated by a critical Dean number are not as apparent in the current device [90]. This may be due to differences in flow patterns as their devices were taller (90-170 μm). Second, the minimum streak width varies less in the increasing Dean number case (standard deviation = 0.27*a*, mean = 1.85*a*) versus the decreasing Dean number case (standard deviation = 0.67*a*, mean = 1.87*a*). This change could indicate that the stronger Dean drag forces at the outlet of the devices in the increasing Dean number case create more steeply varying force field around the equilibrium position causing a lower streak width. Finally, when comparing the decreasing to increasing Dean number cases, there is a shift in the velocity at which minimum streak width is achieved for the larger width devices, from 1.48m/s to 1.73m/s for the 400μm wide device and 1.60m/s to 1.70m/s for the 300μm wide device. This may be due to the Dean number at the outlet or upstream effects of initially focusing at lower Dean numbers, which suggests there may be an optimal Dean flow for focusing performance in a given cross section.

4.4 Adjusted Ratio of Forces Threshold

Other investigators have provided a non-dimensional factor as a possible means of characterizing inertial focusing flows in curved channels defined as the ratio of shear gradient lift to Dean drag forces, R_f. Different approximations have been used for this factor due to the complex relationship between position in the channel, velocity and the inertial lift and Dean drag forces [55]. Of the two main formulations, the first ignores velocity variation altogether in order to make the value more accessible as a design parameter [104] and the other uses an approximation of the secondary Dean flow velocity only valid for a single device cross section (170μm tall and 200μm wide) [90]. Both

approximations accurately predict that each width spiral used in the current experiment is capable of focusing 10μm particles but only the second attempts to predict the velocity at which focusing will initially occur. However, the R_f value at which focusing is initially predicted varies with width based upon the second approximation. In an attempt to decrease the variability of this threshold value, COMSOL simulations were completed to get the average Dean flow velocities, $U_{Dean,Avg}$, for each device width. A power fit of $U_{Dean,Avg}$ versus Dean number similar to previous scalings was generated with an exponent of approximately 1.4 for all the devices simulated as shown in Figure 4-4 [105].

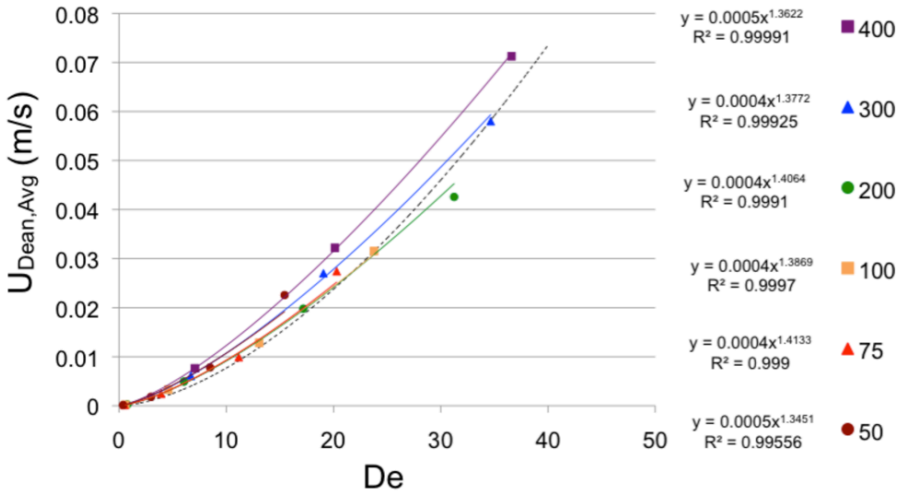

Figure 4-4: COMSOL simulation values for average Dean flow velocity ($U_{Dean,Avg}$) versus the Dean number (De) for each channel width and their approximate scalings. The dashed line is the approximation used by [90] from [105].

These more accurate values for $U_{Dean,Avg}$, are incorporated into the second approximation of R_f defined in Equation 4.1, where the average shear rate $G=U_{Max}/D_h$, where U_{Max} is approximated as $3/2U_{Avg}$, and C_L is a lift coefficient which is a function of cross sectional position and Reynolds number [49].

$$R_f = F_L / F_D = \frac{\rho G^2 C_L a^3}{3\pi\mu U_{Dean,Avg}} \tag{4.1}$$

The more accurate Dean flow velocities reduced the variability of the threshold between the different width devices drastically as shown in Table 4-1, which compares the second approximation with the new adjusted one.

Table 4-1: The R_f threshold values for initially achieving focusing (lowest velocity at which streak width is less than 3.8 particle diameters) in the decreasing Dean number case for the different width devices assuming C_L=0.5. 2nd Approximation used by Kuntaegowdanahalli et al[90].

Width (μm)	2nd Approximation	Adjusted 2nd Approximation
400	1.31	0.83
300	1.54	1.16
200	2.17	1.53
100	3.36	1.81
75	5.37	2.73
50	7.24	1.91

While the new adjusted parameter gives a single threshold (R_f~1) for achieving focusing, a useful value in device design, it still cannot accurately predict the minimum streak width in the different width devices. Figure 4-5 presents the calculated R_f values for the different width devices versus U_{Avg}. Along each line are all of the tested R_f values for each device width.

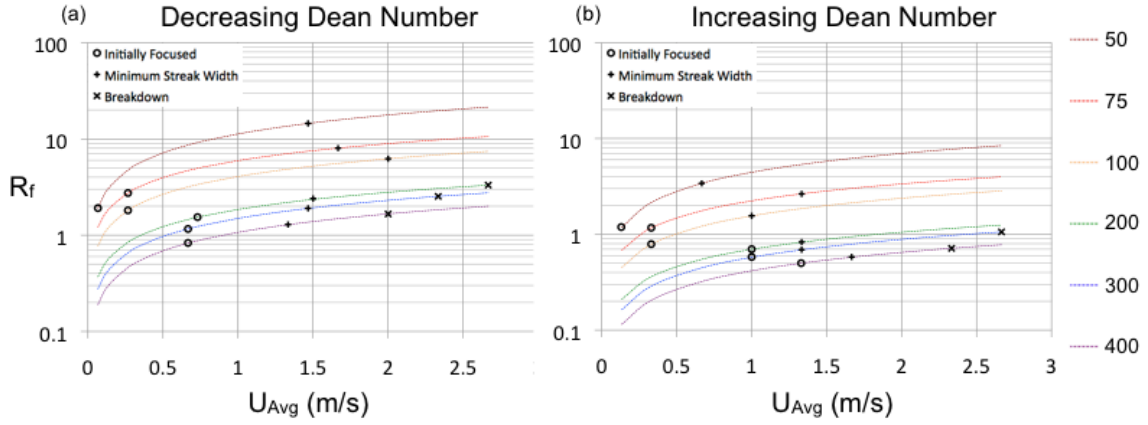

Figure 4-5: R_f versus U_{Avg} for the different device widths in both the decreasing and increasing Dean number cases. The symbols along each device line are indicative of when the streak width initially goes below the 3.8 particle diameter threshold (circles), the minimum streak width (plus signs) and the streak breaks down or when the streak width goes above the 3.8 particle diameter threshold (Xs). The channel width for each line increases from the top line (50μm width) to bottom line (400μm width) as in the legend.

Certain R_f values are marked for each device when focusing is initially achieved (circles), the minimum streak width is achieved (plus signs) and where breakdown occurs, in other

words, when the streak width goes back above 3.8 particle diameters (Xs). The widely varying R_f values for the minimum streak width may indicate that a different balance between forces is required in each device cross section to achieve optimal focusing. It is also interesting that the minimum streak width does not occur at the highest values of R_f where the inertial lift forces are strongest. While the ratio R_f has been useful in the design of single devices for particle sized based separation, in its current cross sectional averaged form, it is not specific enough to account for the range of streak width and position behaviors between devices of different widths even with the simulated Dean flow velocities, for both the increasing and decreasing Dean number cases.

In order to determine the most appropriate parameter for comparing and predicting the performance of curved inertial focusing devices it will be necessary to examine the constituent parts of R_f more closely. For example, the dominant forces that control inertial focusing behavior are governed by several other non-dimensional parameters such as particle Reynolds number, Re_P and Dean number. The particle Reynolds number incorporates the confinement of a particle within the channel, $Re_P=Re_C(a^2/D_h^2)$, where a is the particle diameter. This specialized Reynolds number along with channel aspect ratio are the main factors determining the number and location of equilibrium positions. As these equilibrium positions change the Dean flow velocities that particles at those positions are exposed to also change. Since Dean number varies linearly with Re_C changing the velocity of a fluid is insufficient for decoupling the effects of De and Re_P. This inability of the general non-dimensional numbers to describe the range of behaviors is apparent in Figures 4-6 and 4-7 where the streak width and position data are

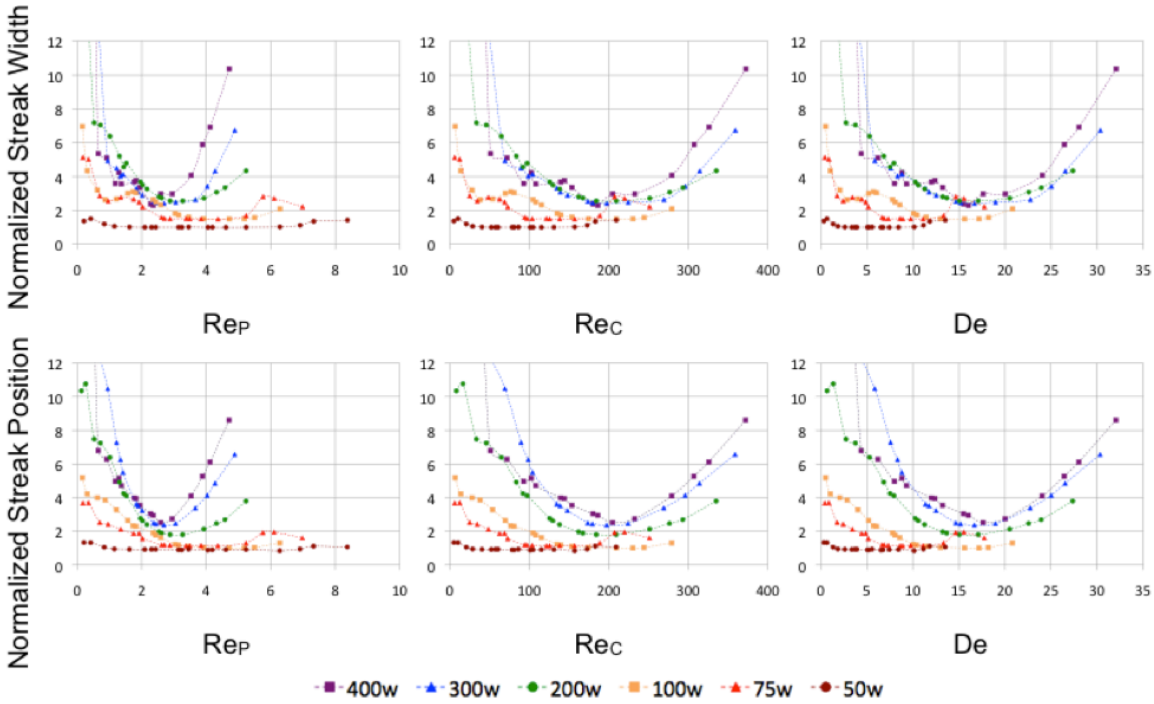

Figure 4-6: Plots of normalized streak width and position are given versus Re_P, Re_C and De non-dimensional parameters for the decreasing Dean number case. Note that the Dean number presented is the instantaneous Dean number at the outlet where the streak width and position measurement was made.

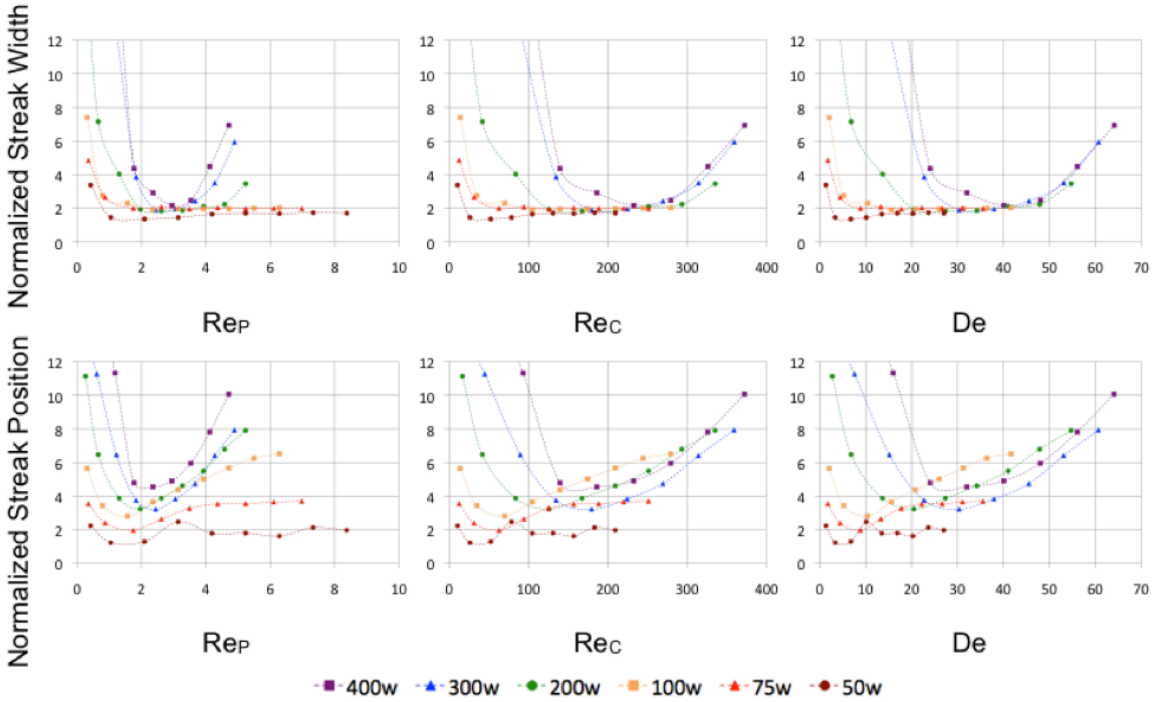

Figure 4-7: Plots of normalized streak width and position similar to Figure 4 are given versus Re_P, Re_C and De non-dimensional parameters for the increasing Dean number case. Note that the Dean number presented is the instantaneous Dean number at the outlet where the streak width and position measurement was made.

presented versus Re_P, Re_C and De for the decreasing and increasing Dean number cases, respectfully.

To this end a brief investigation into decoupling the effects of arguably the two most important non-dimensional values for inertial focusing in curved channels can be accomplished comparing the increasing and decreasing Dean flow cases. At each Reynolds number two different Dean number values at the outlets of the devices could be compared. While the sample size is very small, the predicted streak positional shift towards the center of the channel curvature is present but overall the streak behavior throughout the devices is very similar. It is possible that decoupling these effects is more important in some regimes than others depending on the equilibrium positions and the relative effects of Dean flow as those positions change. Therefore, addressing the change in curvature as a means of isolating the effects of Dean number on focusing behavior should be one of the next steps towards understanding and predicting inertial focusing behavior in all curved channels.

4.5 Dynamics: Decreasing and Increasing Dean Number

Understanding the dynamics of inertial focusing requires going beyond the streak behavior at the outlet to characterize the particle distribution throughout the device. The spiral geometry can be more easily visualized in this manner using straightened images which clearly show the streak width and position along the entire channel as well as the channel length required for focusing as previously described in Figure 3-7. A comparison of the straightened images for six different average downstream velocity conditions increasing from left to right for all six different width devices in the decreasing Dean number case is given in Figure 4-8.

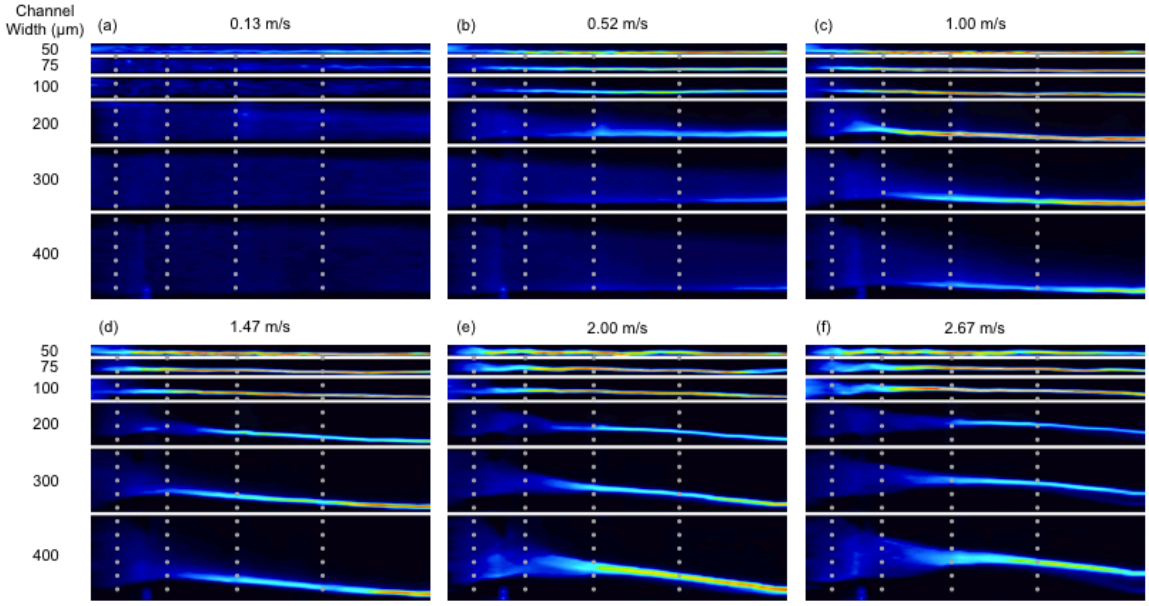

Figure 4-8: Straightened images for similar flow conditions to those presented in Figure 4-2 for all channel widths. Dark blue is low intensity and red/white is high intensity seen when a focused streak is formed. All images are for decreasing Dean number devices.

These straightened images clearly illustrate the previously described dynamic behaviors where focusing is achieved at lower velocities and shorter distances in the narrower devices. The streak movement away from the wall can also be seen to increase with increasing velocity in the wider channels. Despite the motion of the streak away from the wall the position of closest approach to the inner wall remains stable near the outlet of the device. The streak breakdown occurring at higher average downstream velocities for the 300 and 400 μm wide devices can be seen statically in Figure 4-8f.

Other interesting observations include that the streak breakdown seems to begin when the streak initially focuses to the center of the channel rather than the inner wall. Perhaps even more interesting is comparing these straightened images between the decreasing and increasing Dean number cases, as the behavior is strikingly similar. The increasing Dean number case straightened images can be seen in Figure 4-9.

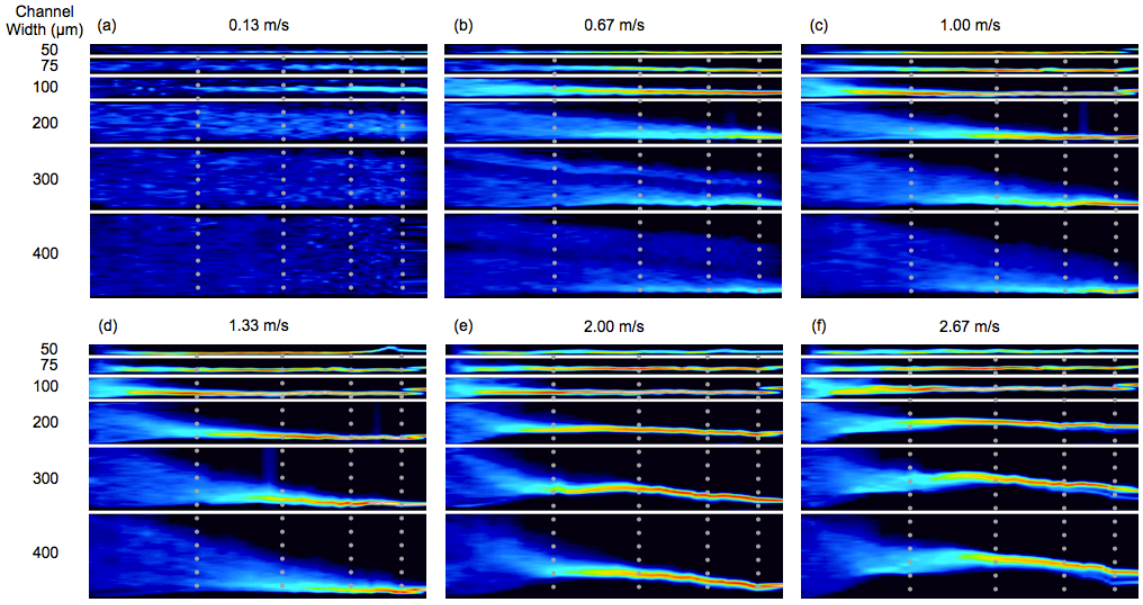

Figure 4-9: Straightened images for similar flow conditions to those presented in Figure 4-2 for all channel widths. Dark blue is low intensity and red/white is high intensity seen when a focused streak is formed. All images are for increasing Dean number devices.

Despite lower Dean number values during the initial stages of focusing the channel length required to achieve focusing is very similar. This may indicate that both Dean number values are within a range that is above a critical value causing the single equilibrium position but not yet to the value where Dean mixing is stronger than the inertial forces. It appears that the streak forms closer to the inner wall for the increasing Dean number case at least at U_{Avg}=0.67, 1.0, and 1.33m/s. This hints at a possible dynamic issue of a particle free layer near the inside wall that is dependent on Dean number also seen by Xiang et al (2012) [106]. From these images it also appears that there is a large change qualitatively in the focusing between the 100 μm and 200 μm wide devices possibly indicating the critical width at which Dean forces become more important in terms of achieving a quality focused streak. Unexpectedly, in the increasing Dean number case, the streak still moves towards the inner wall for the 200 μm and wider channels. This is the opposite of the expected result given the increase in Dean number

toward the outlet of the device. One possible explanation is that there is substantial deformation of the channel near the inlet of the device causing different cross sectional shapes and therefore different equilibrium positions. Alternatively, the Dean flow may not be fully developed over this distance in the wider channels causing this difference. A complete set of straighten images is available in Appendix B.

4.6 Stability and Particle Confinement

Since streak width and position are strongly correlated, the compiled data set can be mapped as a state diagram of velocity, distance along the channel and a measure of streak width relative to the channel width. These are given in Figure 4-10, for the decreasing Dean number case, for each channel width (a-f). The increasing Dean number case state diagrams can be found in Figure 4-11. The streak width is presented as the channel width divided by the streak width as a measure of the particle confinement, ψ, within each channel cross section. Each state diagram shows two regions, one, where the streak width is greater than 3.8 particle diameters (Unfocused – bottom of colorbar), and two, the area of the parameter space where focusing is achieved (Min Particle Confinement to Max Particle Confinement – cyan to red on colorbar above Unfocused threshold). The size of this area is used as a measure of the stability of the focusing, ζ. The maximum confinement, ψ_{Max}, indicative of the minimum streak width for each device, and stability values, ζ, are presented in a summary plot (g).

The performance of these devices with increasing width is subject to two competing mechanisms. First, the maximum particle confinement increases with increasing width. This is an extremely important performance metric for lab-on-a-chip applications such as

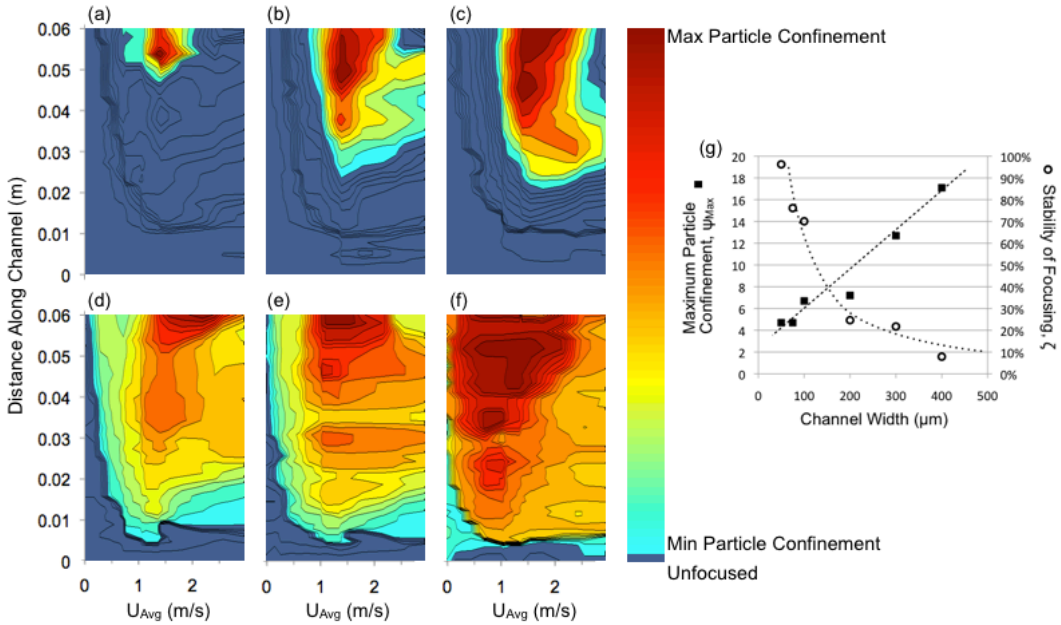

Figure 4-10: State diagrams for each decreasing Dean number device whose color indicates the particle confinement (Red maximum – Cyan minimum – Dark blue next to cyan unfocused) over the length of the device in the vertical direction and the different average downstream velocities in the horizontal direction for the different width channels (a) 400μm, (b) 300 μm, (c) 200 μm, (d) 100 μm, (e) 75 μm and (f) 50 μm. A plot (g) of the actual maximum particle confinement for each device and the corresponding amount of the parameter space where focusing was achieved. Guidelines for the maximum particle confinement (dashed) and focusing stability (dotted) are given as well.

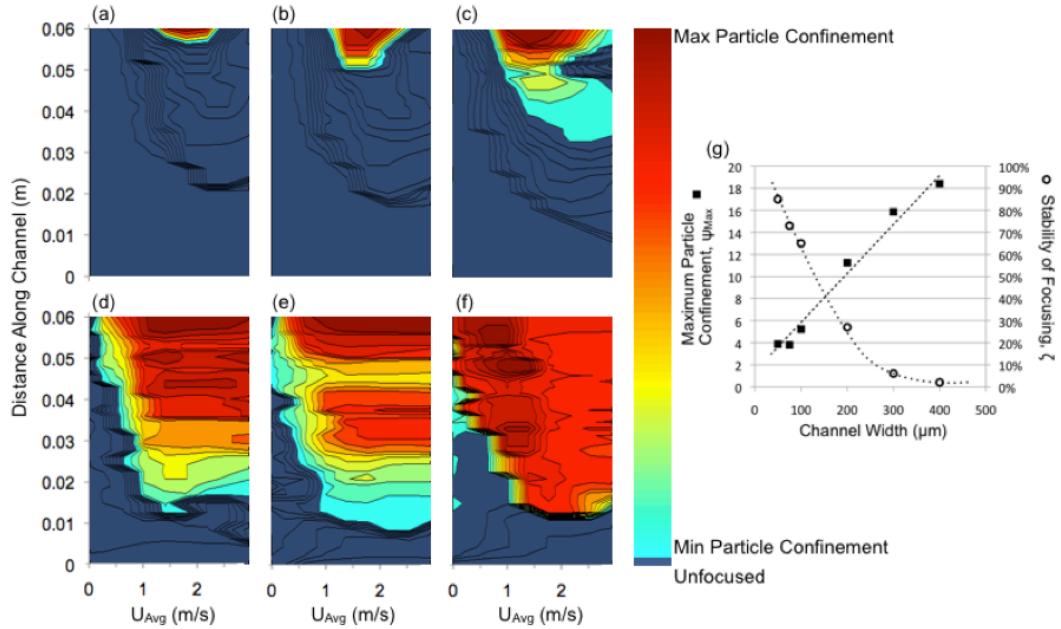

Figure 4-11: State diagrams for each increasing Dean number device whose color indicates the particle confinement (Red maximum – Cyan minimum – Dark blue next to cyan unfocused) over the length of the device in the vertical direction and the different average downstream velocities in the horizontal direction for the different width channels (a) 400μm, (b) 300 μm, (c) 200 μm, (d) 100 μm, (e) 75 μm and (f) 50 μm. A plot (g) of the actual maximum particle confinement for each device and the corresponding amount of the parameter space where focusing was achieved. Guidelines for the maximum particle confinement (dashed) and focusing stability (dotted) are given as well.

sample concentration and volume reduction. However, stability, defined as the operating range of lengths and flow rates where the quality focusing can be achieved, decreases with increasing width. Achieving robust focusing is also important given the complex nature of biological fluids and the sample to sample variability based upon health and age of the patient.

Although the maximum particle confinement is linear over the range of device widths tested, the slight increase in the measured streak width and steady decrease in stability suggests that there may be a maximum width for a given length device at which focusing can no longer be achieved, at least for a channel length of 6cm. The stark transition in behavior between the 100 μm and 200 μm wide devices can also be seen in these state diagrams again indicating the transition to Dean flow dominated focusing behavior. This same transition and the general trends hold for the increasing Dean number devices as shown in Figure 4-11. One minor difference between the decreasing and increasing Dean number cases are that the focusing stability is lower for the increasing Dean number case when directly comparing devices of the same width.

The breakdown of focusing is also visible in Figures 4-10 and 4-11 at higher velocities (decrease in particle confinement moving left to right after the point of maximum particle confinement, especially at the end of the device or the top of each diagram). This breakdown occurs at lower U_{Avg} values in the increasing Dean number device suggesting the breakdown be partially due to a Dean flow related phenomenon.

Another important factor that can be witnessed in the state diagrams is the channel length required for each width and flow rate in order to achieve focusing (Minimum distance up the vertical axis to a particle confinement equivalent to the channel width

divided by 3.8 particle diameters marked by the end of the unfocused region in Figures 4-10 and 4-11). This minimum distance required for focusing decreases with increasing downstream velocity similar to the expression for straight channels presented by Di Carlo but must be adjusted in order to incorporate effects of Dean flow, since the secondary flow assists the focusing in the larger channels where the inertial lift driven migration would be much slower without the additional Dean drag force component [54]. A comparison of the previously reported scaling for straight channels compared to the data from the current experiments is given in Figure 4-12. Note that the discrepancy between straight channel values (dashed) and the spiral devices (markers) is greater for the larger widths indicating the larger advantageous effect of Dean flow in the wider devices.

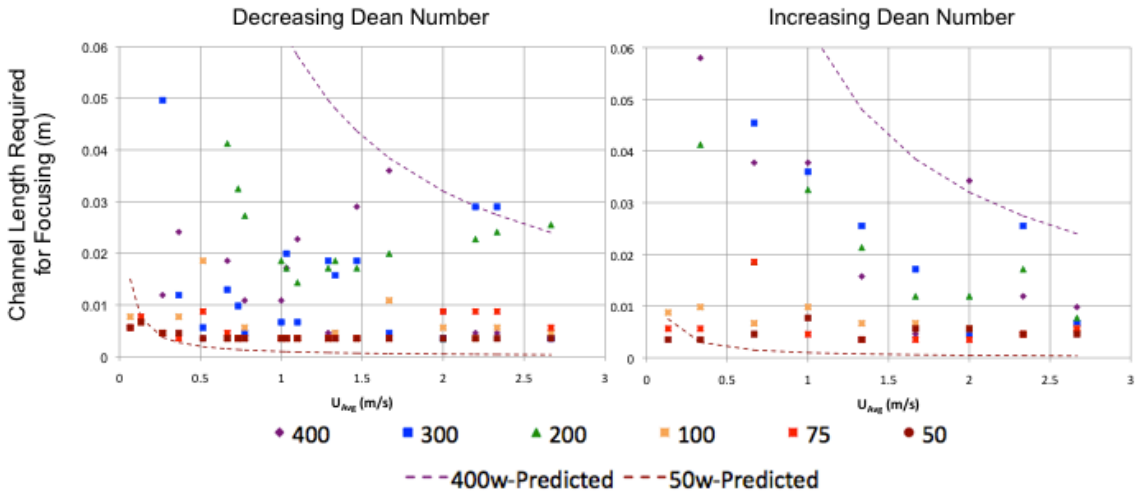

Figure 4-12: Plots of the length of channel required at each flow rate to achieve focusing or when the 50% threshold streak width is less than 2 particle diameters. The dashed lines are the length predicted by Di Carlo for the 400μm wide (top) and 50μm wide (bottom) devices [54].

It should be noted that significant deformation of each channel was noted at several of the higher velocity flow conditions. This may partially explain the effect of higher average downstream velocities (higher driving pressure and greater deformation) on the dynamics of focusing as the required channel length for achieving focusing increases for the wider devices at the higher average downstream velocities greater than 1.5 m/s. An

expanded cross section reduces the downstream velocity of the particle as well as increases the distance a particle must migrate across the channel to its equilibrium positions thereby increasing the overall length of the device needed to obtain quality focusing. The deformation does not necessarily explain the breakdown of the streak at the outlet of the device at the higher velocities, as at the outlet of each device the absolute pressure difference to atmospheric is approximately zero.

4.7 Breakdown at high U_{Avg}

A common thread throughout the results is the breakdown of the focusing at higher average downstream velocities. A closer inspection of this occurrence shows that the breakdown appears as the formation of two separate streaks after moving away from the wall. One of these two streaks remains at a seemingly constant position while the other (actually 2 streaks mirrored across the center of the channel height) moves toward the center of the channel.

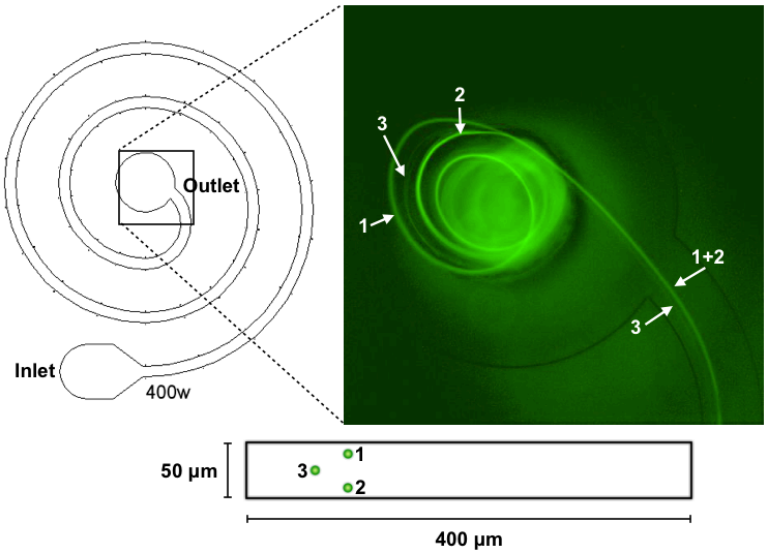

Figure 4-13: Device schematic for streak breakdown image. This specific video is from a increasing Dean number experiment (flow from outside to inside of spiral as labeled from inlet to outlet). U_{Avg} = 2.667 m/s.

Figure 4-13 presents an image of this breakdown within the 400 μm wide channel in the increasing Dean number condition with the different streaks labeled and matched with their approximate cross sectional positions in a diagram of the cross section. It should be noted that the multiple streaks are treated as a single wide streak in our analysis. In actuality, although the single streak formation breaks down, each individual streak retains a low but discrete streak width. It is also clear, based upon relative streak intensities, that more particles remain in the two vertically mirrored streaks rather than the one closer to the wall indicating that this position is less stable or simply encompasses a smaller area of the cross section with respect to initial positions of the particles. A more detailed investigation of this breakdown and its corresponding spatial structure is necessary to determine the specific mechanism causing the behavior.

4.8 Conclusion

Inertial focusing dynamics and streak behavior in different width spiral microchannels are presented over a large parameter space. While the rich inertial focusing dynamics observed in curved channels will be advantageous for future generations of medical and scientific devices they also merit further study to elucidate the underlying physical mechanisms and their associated limitations. The most pressing concerns about the deformation at higher velocities and its unknown effect must be overcome in order to compare these experimental results to theory or simulations. Since the deformation may be the root cause of the breakdown it is impossible to tell if there truly is an upper limit on inertial focusing in spirals without a rigid device.

Chapter 5

Reynolds and Dean Number Effects

5.1 Overview

The decoupled effects of Reynolds and Dean numbers are examined in inertial focusing flows. A complex set of inertial focusing behavioral regimes is discovered for confined flows in curved microfluidic channels over a range of channel Reynolds numbers (8-419), curvature ratios (0-0.129) and particle confinement ratios (0.066-0.225). These regimes are segregated by the differential particle migration either towards or away from the center of curvature as the channel Reynolds number is increased. The transition between these two regimes is shown to be a set of conditions where single-point equilibrium position focusing of particles of different sizes is achieved. The mechanism describing the presented motion of particles in such flow is hypothesized as involving three competing effects: the secondary Dean flow drag on the particles, the redistribution of the main flow velocities by Dean flow and the variation of equilibrium position with Reynolds number.

5.2 Introduction

Inertial focusing is a counterintuitive phenomenon where suspended particles migrate across streamlines and order deterministically at equilibrium positions within confined flows in channels. This migration occurs under certain conditions due to inertial effects of the fluid motion around the particle and the interaction of this disturbed flow field with the walls of the channel [37, 38, 47]. Equilibrium positions arise from a balance between

two distinct effects; a shear gradient lift force directed towards the walls of the channel and an opposing wall effect [89]. This regime and associated particle motion have been entitled inertial focusing. Inertial focusing has generated significant interest in the realm of microfluidics because it combines high throughput capability with precision particle positioning and offers theoretical intrigue due to the seemingly endless surprises that accompany experimental results.

Through careful characterization of these flows much has been determined about the forces and parameter requirements for inertial focusing to occur. It is generally accepted that inertial focusing in straight channels is dependent on two main parameters: Reynolds number, Re_C and the particle confinement ratio, λ:

$$Re_C=\rho U_{Max} D_h/\mu \quad (5.1)$$
$$\lambda=a/D_h \quad (5.2)$$

where ρ is the fluid density, μ is the fluid viscosity, $U_{Max}\approx 3/2 U_{Avg}$ is the maximum velocity of the fluid and D_h is the hydraulic diameter of the channel defined as $D_h=2hw/(h+w)$ where h and w are the height and width of the channel cross section respectively, and the particle confinement ratio, λ, or ratio of the particle size, a, to the hydraulic diameter, D_h, of the channel.

Prior research has determined a minimum threshold for inertial focusing to occur such that $\lambda>0.07$ and the particle Reynolds number, $Re_P=Re_C\lambda^2$, is ≥ 1 [54]. The locations of the equilibrium positions within a channel have been shown to be determined by confinement and the shape of the channel cross-section in addition to the flow parameters and particle properties (e.g. size, shape, deformability) [55, 56, 59-61, 69, 107, 108]. For example, in a rectangular cross section there are equilibrium positions centered on each face of the rectangle, approximately $0.3w$ from the centerline in either lateral direction

and 0.3*h* in either vertical direction. The aspect ratio of the channel determines the likelihood of particles occupying each different equilibrium position due to both initial starting position and the asymmetry in the shear forces in both the vertical and lateral directions [107]. In contrast, for an aspect ratio $h/w \approx 0.5$, the equilibrium positions centered on the long faces of the channel are more preferred due to the blunted velocity profile in the longer dimension.

Channel length also plays an important role in ensuring that particles experience inertial forces for a sufficient amount of time in order to migrate to equilibrium positions. This critical channel length scales as $L_f \approx 20\pi D_h/Re_P$ for an aspect ratio $h/w \approx 0.5$ [54]. Since this parameter scales inversely with particle size, smaller particles require longer channels so that the diminished inertial forces can be compensated by prolonged residence times. However, this becomes unfeasible from a practical standpoint for smaller particles since the straight microchannel would have to be meters in length. For this reason, curvature was first added to inertial focusing channels as spirals are much more efficient in length of channel per unit area than straight channels. However, the key consequence of utilizing curved channels was the establishment of a secondary flow called Dean flow that appears at finite Re_C. Dean flow is a consequence of the momentum of the faster moving fluid in the center of a channel (parabolic flow) moving towards the outside wall of a curved channel [84]. This transfer of fluid in incompressible flow towards the outer wall is balanced by a recirculation of fluid along the top and bottom of the channel cross section. The strength of this secondary flow is characterized by the inertia of the fluid and the curvature of the channel, or the non-dimensional Dean number defined as $De=Re_C\delta$, where δ is the square root of the curvature ratio $\delta=(D_h/2r)^{0.5}$, where r

is the radius of curvature of the channel. This secondary flow causes an additional drag force on particles within the flow adjusting the number and locations of inertial focusing equilibrium positions [70, 73, 78, 89, 91, 92, 99, 100, 104, 106, 109-111].

Several studies have explored the parameter space for curved inertial focusing channels including different curve designs [70, 104], spiral configurations [111], scalability [110] and dynamics of the focusing behavior [78, 106]. The majority of these studies were based on some method of varying the ratio of inertial lift and Dean drag forces, primarily by changing flow rate [73, 90, 91, 100, 109, 110], but also by changing the cross section [78, 90, 92, 99], and investigating multiple lanes of a spiral with different curvature values [78, 106]. In effect, these previous studies have varied multiple important non-dimensional parameters simultaneously or measured the particle behavior for different residence times at a given flow rate, which has been shown to affect eventual focusing behavior [78]. The parameter ranges tested in these different papers are given in Table 5-1.

Table 5-1: Parameter ranges tested in literature their associated channel dimensions and the means of which the Dean number was varied. *Only a single particle sized used. Variation due only to change in cross sectional dimensions.

h (μm)	w (μm)	l (cm)	Re_C	δ	λ	Dean Variation	Ref.
100	300	271	15	0.046	0.070	Flow Rate	[110]
50	100	13	4	.086-.105	0.110	Flow Rate	[107]
50	250-1090	11.3	Up to 389	.066-.173	.024-.12	Flow Rate	[91]
90-140	500	20	Up to 169	.085-.104	.046-.091	Flow Rate, Channel Dimensions	[90]
55	160	16	Up to 71	.083-.108	.026-.059	Flow Rate, Consecutive Turns	[106]
50	50-400	6	Up to 355	.086-.129	.111-.198*	Flow Rate, Channel Dimensions, Flow Direction	[78]
80-130	600	40.2	Up to 368	.067-.094	.027-.186	Flow Rate, Channel Dimensions, Trapezoidal Cross Section	[92]
29	50	7.2	Up to 8.4	.096-.111	0.027	Flow Rate	[73]
50	150	16.6	Up to 150	.079-.104	.067-.133	Flow Rate	[99]
50	100	4	Up to 419	0-.129	.067-.225	Channel Radius, Flow Rate	Current

This chapter presents a systematic study of the decoupled effects of Dean number and Reynolds number on inertial focusing behavior for a range of different particle confinement ratios. These results are then interpreted in terms of the potential to separate

particles exposing different regimes of particle migration in curved channels. The transition between these regimes is then examined in more detail. This is followed by a summarizing discussion of the mechanisms behind the different regimes of migration.

5.3 Lateral Focusing at Varied Reynolds and Dean Numbers

Re_C maps are used to present the results of the parameter space exploration using the devices depicted in Chapter 3.2.2. These have been compiled by taking intensity line scans at the outlet position of each channel at different flow rates. Each line scan becomes a column of pixels in the Re_C map showing the inertial focusing behavior at the outlet across a large range of Re_C values. This process is described in greater detail in Chapter 3. The bottom of each Re_C map represents the inside wall of the channel closer to the center curvature (x/w=0) and the top is the outside wall, further from the center of curvature (x/w=1).

Figure 5-1 shows a compilation of the particle focusing behavior over the investigated ranges of the three key variables: channel Reynolds number, Re_C, average channel curvature ratio, δ, and particle confinement ratio, λ. The top row of Re_C maps shows the behavior of each particle size in a straight channel. As expected, the larger particles both focus to the center of the channel when Re_P values are greater than 1. For instance, when Re_C>45 and Re_C>20 for λ=0.149 and λ=0.225, respectively. In comparison, the smaller particles (λ=0.066) do not experience as strong lift forces since the shear gradient lift scales with a^3 and consequently the particles do not achieve as significant focusing over the same channel length [55]. The smaller particles achieve Re_P=1 at and Re_C value of 229, and show some focusing trends near the high shear regions near the sides of the channel at lower Re_C values.

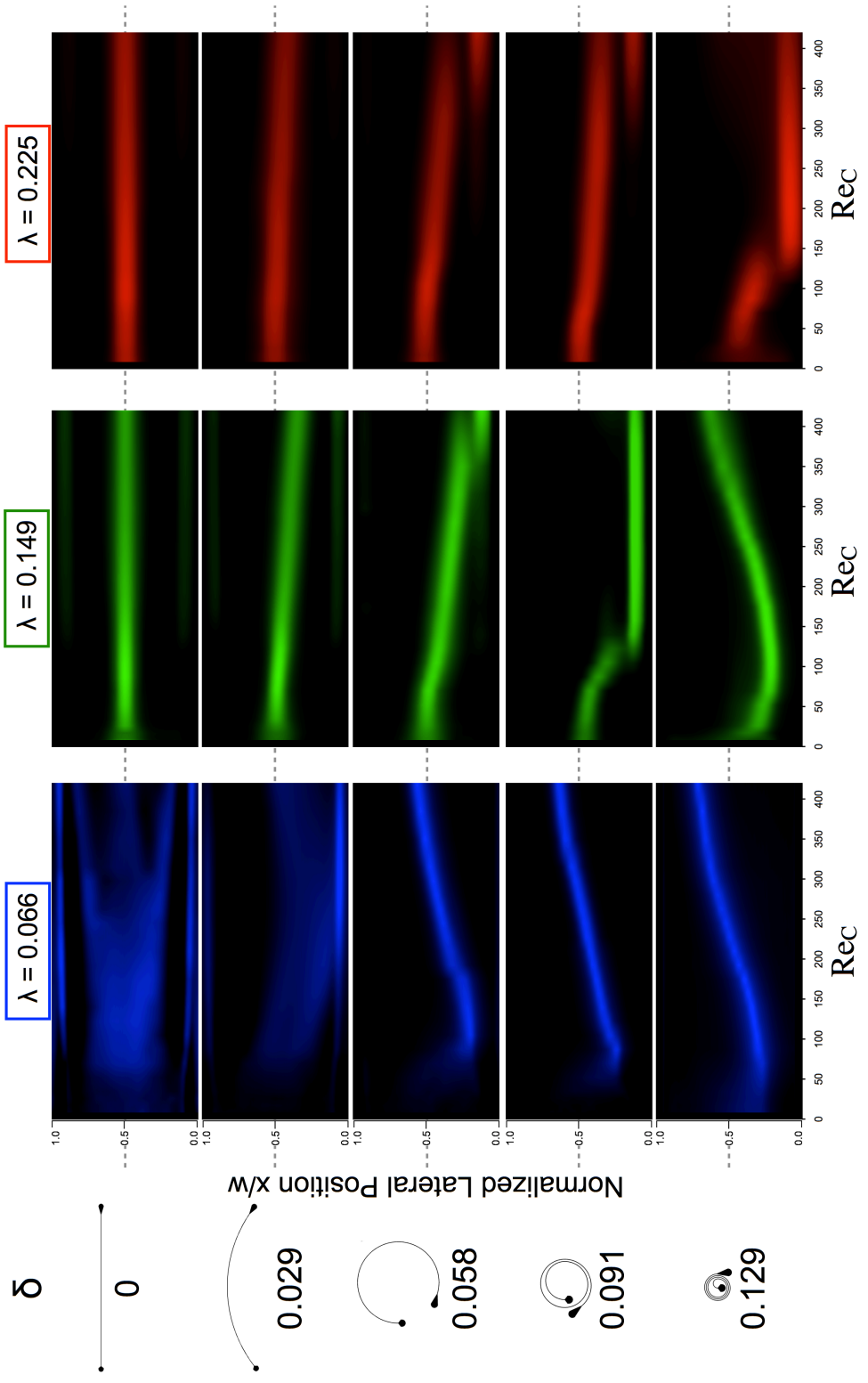

Figure 5-1: Re_C maps for each condition of curvature (increasing from top row to bottom row) and particle confinement (increasing from left column to right column). Each column of pixels compares equivalent Re_C at 5 different Dean numbers.

These high shear regions seem to retain a small fraction of particles near the sidewalls at increasing Re_C as λ increases, indicating that the lateral lift forces due to the shear gradient have become strong enough to resist edge effects from the side walls, at least over a channel length of 4cm. For example, at certain Re_C values that scale with $\sim\lambda^{0.4}$ (~105 for λ=0.066, ~140 for λ=0.149 and ~180 for λ=0.225). The existence of these side streaks is consistent with a decrease in positive lift coefficient found at increasing Re_C by Zhou and Papautsky [56]. The formation of these side streaks also indicates the limited distances over which the side wall lift forces are dominant.

The second row of Re_C maps are for the slightly curved channels and each consecutive row increases in curvature ratio, δ, to the tightest spiral on the bottom row. The Dean number in the tightest spiral device (δ=0.129) will increase fastest with respect to Re_C and more slowly as the δ decreases as shown in Figure 3-2. A direct comparison of the focusing behavior for each particle size at equivalent Reynolds numbers but different Dean numbers is accomplished by comparing a single column of pixels across the Re_C maps vertically.

For the smallest particles (λ = 0.066), the addition of a small amount of curvature and the resulting Dean flow causes advection of particles across the channel in a manner similar to Dean flow fractionation [90, 91]. This increases the number of particles found at an inner equilibrium position (~0.1x/w), but over the 4cm channel length does not produce a single lateral equilibrium position. At higher curvature values a single lateral focusing position emerges. At this low confinement ratio (λ = 0.066) the particles do not initially focusing to the center of the channel width. Instead, the initial focusing position is dependent on the curvature. At a Re_C of 104 the three highest curvature ratio channels

(δ = 0.058, 0.091, 0.129) have achieved single lateral point focusing and the streaks are located at x/w = 0.210, 0.292 and 0.314 respectively, increasing with ~$\delta^{0.5}$. Qualitatively, there also appears to be a weak trend that the minimum Re_C value to achieve single lateral point focusing decreases with increasing curvature, however, the minimum Re_C value only varies over the difference between two consecutive flow rates.

For the next larger particles in the center column of Re_C maps (λ =0.149), the focused stream initially forms at the centerline of the channel at low Re_C (~9) in all the channels except the highest curvature where the streak initially forms at x/w=0.36 at the same low Re_C (~9). As the curvature is increased the central streak shifts towards the inner wall as expected for particles focused to vertically mirrored equilibrium positions at the top and bottom of the channel. This high quality single lateral position focusing is achieved in the δ=0.091 device over the Re_C range of 157-384 and the streak is positioned at approximately x/w=0.1. In the highest curvature case, δ=0.129, the streak initially forms slightly closer to the inner wall of the curve rather than the centerline, approaches the inner most equilibrium position (minimum x/w=0.24) but then the streak moves away from the center of curvature towards the outside of the channel. The largest particles (λ = 0.225), act similarly to the middle sized particles (λ = 0.149) although the transition to the innermost equilibrium position is delayed in terms curvature ratio (δ = 0.129 for λ=0.225 rather than δ = 0.091 for λ=0.149).

Through the quantification of streak position, determined by the midpoint of the lateral area above a normalized intensity threshold of 0.05, two segregated regimes emerge: 1, Particles initially focusing at the center of the channel (x/w = 0.5) and migrate towards the inner wall of the curved channel (x/w = 0), and 2, Particles that initially focus

on the inner half of the channel (x/w < 0.5) and migrate towards the outer wall as Re_C increases. Figure 5-2 presents the two different scenarios (light gray highlights – focusing away from center of curvature versus towards – no highlights) and their associated streak position data grouped by particle confinement.

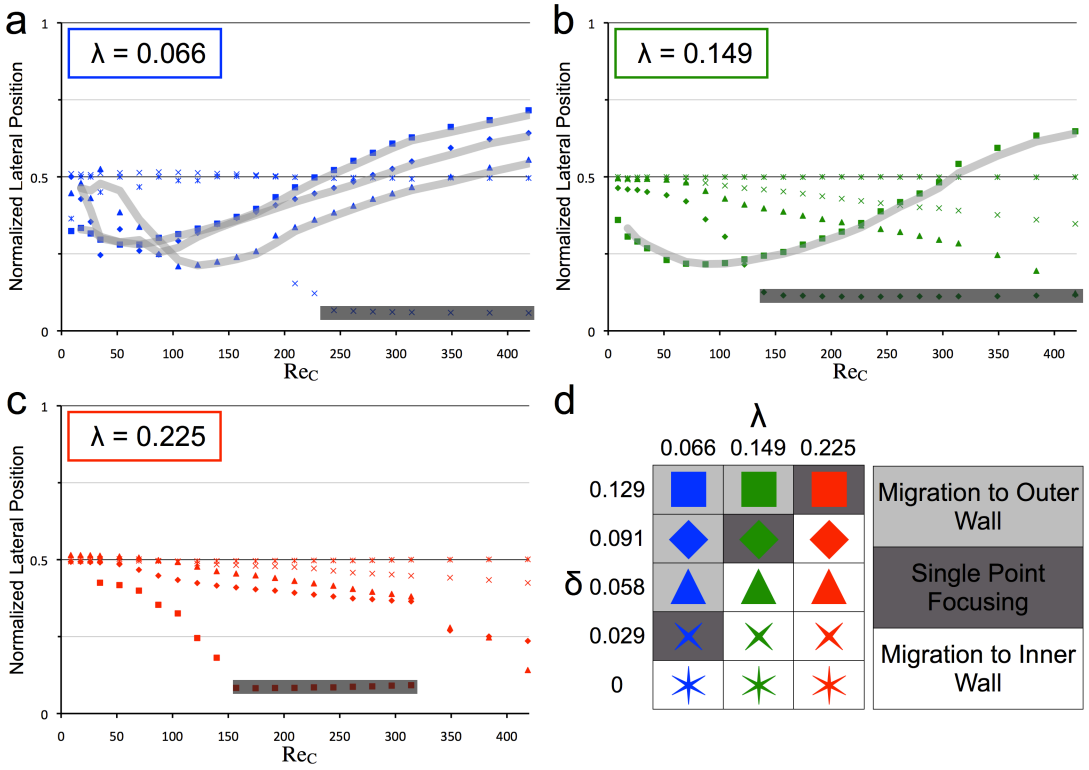

Figure 5-2: Streak position data for all channels plotted versus Re_C for (a) λ = 0.066 (blue), (b) λ = 0.149 (green) and (c) λ = 0.225 (red). In each plot the marker shape corresponds to the δ value (asterix = straight, x = 0.029, triangles = 0.058, diamonds = 0.091 and squares = 0.129) as shown in the legend (d). Light gray highlights indicate that the specified condition describes eventual migration towards the outside wall. Dark gray indicates single lateral point focusing at innermost equilibrium position.

Streak position is plotted versus Re_C for all of the parameters tested where (a) λ=0.066, (b) λ=0.149 and (c) λ=0.225. The light gray highlights indicate that the particle migration follows the second regime described (migration towards the outer wall) and the dark gray lines indicate the transition between the two stated regimes. This transition coincides with the flow conditions when the streak motion to the inside wall jumps to the inner most equilibrium position (~x/w=0.1) or never reaches the inner position before starting to move towards the outside wall of the channel as previously mentioned for the δ=0.091,

λ=0.149 case. This transition occurs at higher δ for larger particles (δ=0.029 for λ=0.066 and δ=0.091 for λ=0.149) and therefore only at high δ will the fractionation typically described for Dean flow assisted inertial focusing occur. One interesting note here is that if the closest approach of the streak to the inside wall (minimum streak position) is plotted versus the ratio of particle size to curvature it appears that the transition between regimes occurs at approximately a ratio of $\lambda/\delta \approx 2.5$ for the current set of devices.

Since the three main parameters were varied separately it is possible to use best-fit analysis to try to collapse the data using the independent parameters. Through this analysis it was determined that the streak position within the two separate regimes (inner and outer directed) could be nearly linearized. The motion of the streaks for each particle size towards the inner wall actually is best described in two separate fits segregating the cases where the innermost equilibrium position is achieved. For the majority of data at low Dean number the position of the streak is linear with Dean number, $Re_C\delta$, as shown in Figure 5-3. These nearly linear relationships with Dean number each had a distinct slope that was then fit to the particle confinement, giving a scaling of approximately $\lambda^{-1.52}$. There was a large discrepancy between this scaling and the subset of cases where the streak moved to the innermost equilibrium position (grayed area on Figure 5-2). These cases departed from the previous scaling at different flow conditions but each had a stronger dependence on Dean number. This was not able to be fit as the departure conditions varied in Re_C and δ, however, dependence was assumed to be related to the Dean flow velocities that scale with $\sim Re_C^2$, but are slightly dependent on the curvature of

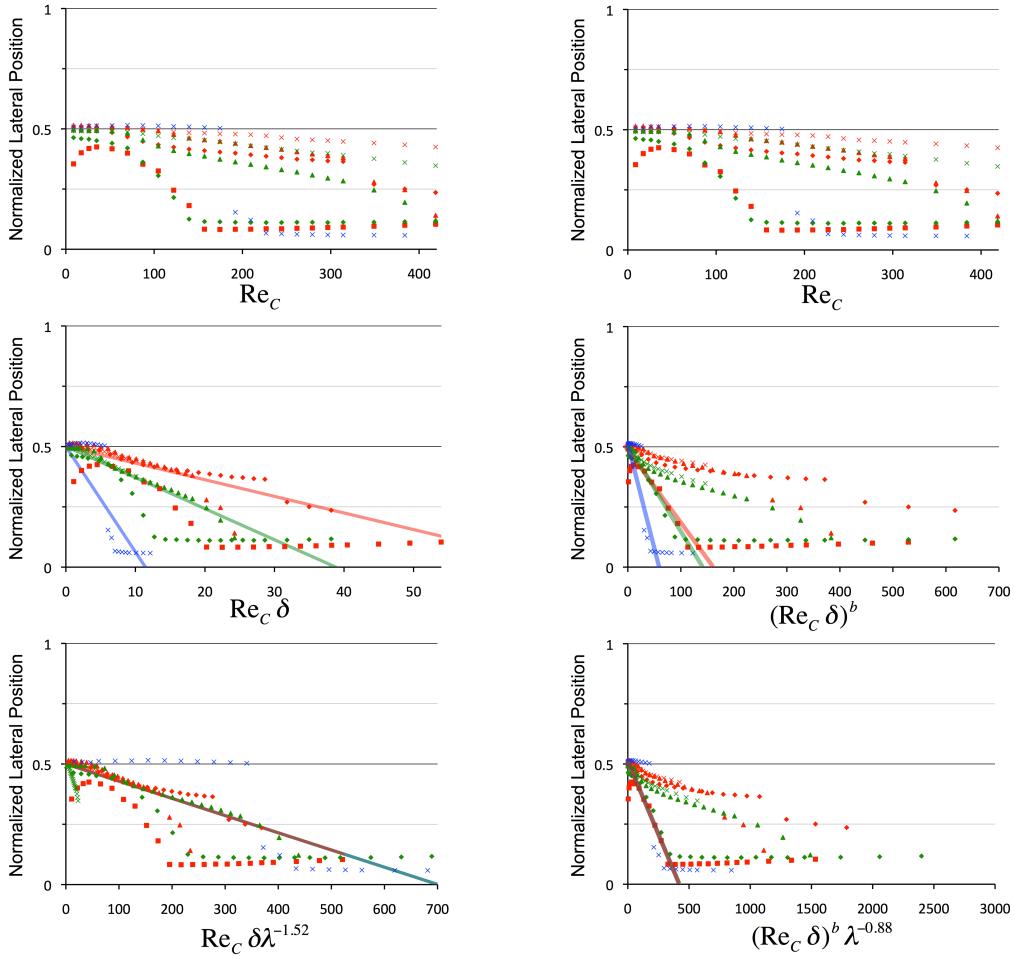

Figure 5-3: Best-fit analysis results for streak motion towards the center of curvature. Right side plots were used for fitting the conditions where innermost equilibrium position focusing is achieved and the left side were used when fitting for the other cases.

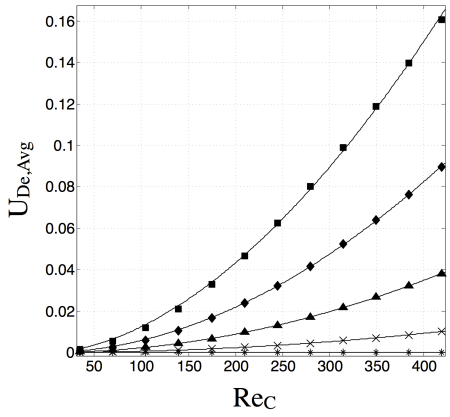

$$U_{De,Avg} = cU_{Avg}^{b}$$

δ	c	b
0.129	3.19E-06	1.796
0.091	8.60E-07	1.914
0.058	2.43E-07	1.982
0.029	5.76E-08	2
0	N/A	N/A

Figure 5-4: Power-law fits for simulated Dean flow velocities versus Re_C for different δ.

the different devices. Each device follows a different power law relationship between the Dean flow and the axial flow that are summarized in Figure 5-4. With this new scaling $(Re_C\delta)^b$, the cases in which innermost equilibrium position focusing is achieved become almost linear and were collapsed for all of the particle sizes using a nearly inverse relationship to the particle size, $\lambda^{-0.88}$ as shown in the right column of Figure 5-3. This makes sense with each particle size having a different balance between inertial lift and Dean drag. In other terms, the motion of the larger particles towards the inner wall requires higher Dean flow. The physical mechanisms for these different scalings are not known at this time. However, a useful tool at least for the current cross sectional shape is an approximate condition for achieving focusing at the innermost equilibrium position, when $(Re_C\delta)^b\lambda^{-0.88}\sim700$ and the previously mentioned condition of $\lambda/\delta \approx 2.5$.

The second regime was less clear in terms of generating a scaling parameter partially due to only having a single δ case for λ=0.149 and none for λ=0.225 and partially due to the complex nature of the forces changing with position of the particles throughout the cross section. However, the motion of the streak in all cases seem to follow similar paths relative to Re_C but start at different initial positions dependent on λ and δ (λ=0.149 δ=0.129 minimum x/w=0.216, λ=0.066 δ=0.129 minimum x/w =0.260, λ=0.066 δ=0.091 minimum x/w =0.248, λ=0.066 δ=0.058 minimum x/w =0.210). The slope of the linear portions (near where the streak crosses the centerline of the channel x/w=0.5) when plotted versus Re_C were not correlated with δ (λ=0.066 δ=0.129 slope 0.00135, λ=0.066 δ=0.091 slope 0.00174, λ=0.066 δ=0.058 slope 0.00123) and only slightly dependent on particle size (λ=0.149 slope 0.00149 versus λ=0.066 average slope 0.00125). Obviously, this cannot be conclusive with the low number of data points. Therefore, the data was

collapsed using the point at which each streak position plot crossed the centerline (x/w=0.5) of the channel. The approximate scaling generated is shown sequentially in Figure 5-5 was able to collapse the data such that the parameter value for when the particles cross the centerline of the channel after focusing were all equal, $Re_C\delta^{1/2}\lambda^{-0.33}$~200.

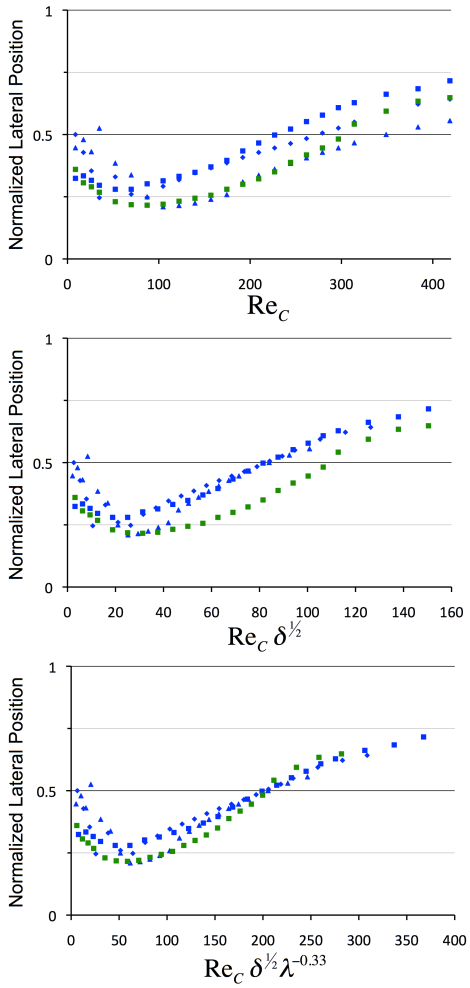

Figure 5-5: Best-fit analysis results for the flow conditions and particle sizes where the eventual streak motion is away from the center of curvature.

This scaling indicates a less pronounced dependence on particle size and channel curvature for the motion of the streak towards the outer half of the channel. It is also apparent that the higher δ values cause equilibrium positions closer to the outside wall of

the channel curvature at equivalent Re_C values. This is shocking because if the particles are at equilibrium positions mirrored at the top and bottom of the channel at consistent height locations the increased Dean flow at equivalent Re_C value should be pushing the particles back towards the center of the channel curvature. The final approximate scalings for the different regimes of focusing are summarized in Figure 5-6.

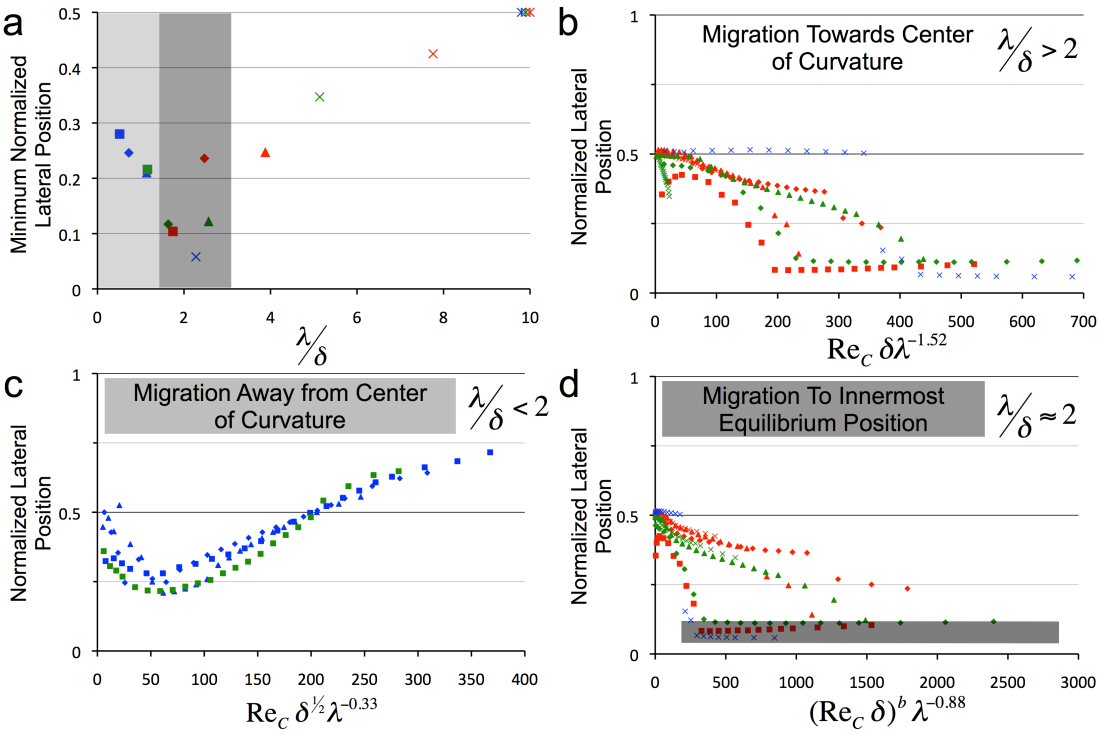

Figure 5-6: Summary of best-fit analysis for the different regimes of inertial focusing. (a) Minimum streak position for each device and particle combination (any Re_C value) showing highlighting the possible threshold value of $\lambda/\delta \approx 2.5$. (b) Final plot of cases where the streak eventually moves towards the center of curvature but not achieving the innermost equilibrium position. (c) Final plot of cases where the streak eventually moves away from the center of curvature. (d) Final plot of cases where the streak moves towards the center of curvature and achieves the innermost equilibrium position.

All of these behaviors are were confirmed over a 3.5 log difference in length fraction, fraction of a distance on a single line taken up by particles if all particles co-located on a single line along the channel. There may be a maximum concentration where the innermost equilibrium positions become locally saturated with particles and a decrease in streak quality is detected but these behaviors due to particle-particle interactions

especially between different sizes are of significant interest for further investigation. There is also a discrete distance over which the particle streak jumps when transitioning into the innermost equilibrium position which is ~1.5 particle diameters (1.52*a* +/- 0.09*a*).

5.4 Separation Potential and Regimes of Separation

An intriguing consequence of the two different regimes of focusing is the change in spatial arrangement across the channel width with particle size. Not only does this indicate a more complex scaling of forces than provided in the literature but there are also implications of these spatial arrangements in terms of the ability to separate particles. The overlaid images in Figure 5-7 graphically show the streak positions of the different sized particles over the entire parameter range. At different flow conditions these intensity distributions are either distinct, able to be separated, or overlapping, not able to be separated. The three highlighted examples (A, B and C) present three distinct cases where the particle streaks are changing in spatial arrangement from the inside to the outside wall as each size changes focusing behavior from inner to outer motion of the streak with increasing Re_C. In the δ=0.091 device alone two different arrangements may be achieved by simply changing flow rate. At Re_C=140 the arrangement of particles from inside to outside is λ=0.149, λ=0.066 and λ=0.225 (Figure 5-7 case A). However, at Re_C=314 the arrangement of particles changes to λ=0.149, λ=0.225 and λ=0.066 suggesting that the larger particles continue to migrate closer to the inside wall and the smaller particles are shifting towards the outside (Figure 5-7 case B). Finally, in the δ=0.129 device, both the smaller particle sizes trend towards the outer half of the channel and the largest particles

shift into the innermost equilibrium position allowing for the final arrangement of particles λ=0.225, λ=0.149 and λ=0.066 at Re_C>227 (Figure 5-7 case C).

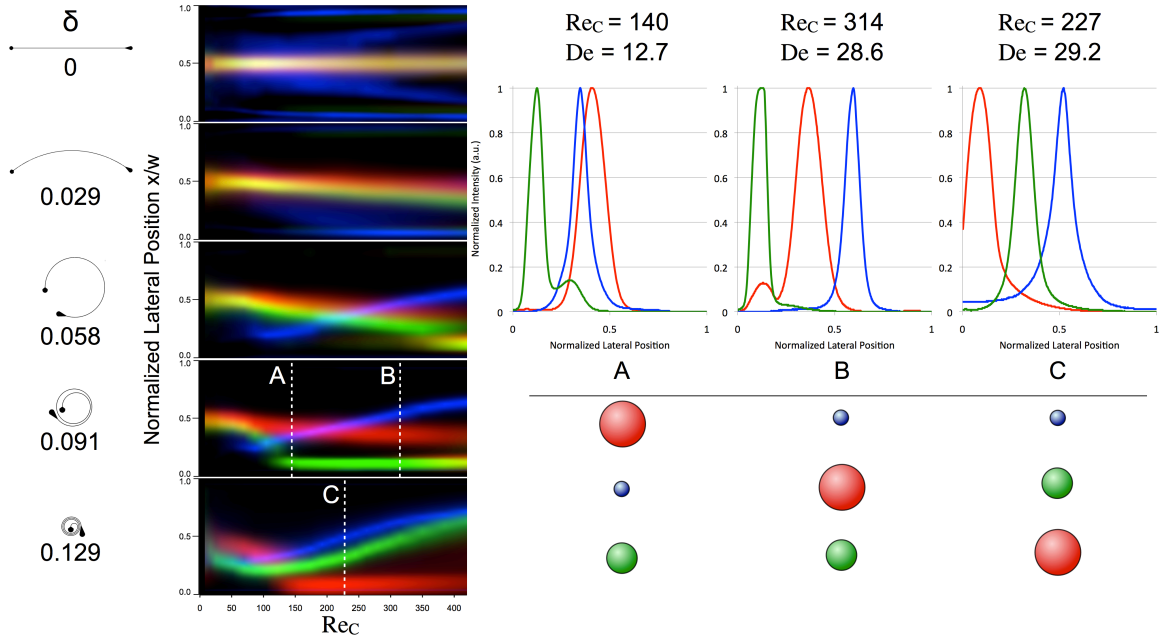

Figure 5-7: This figure merges the previous Re_C maps for each device for more direct comparison of the effect of particle confinement. Intensity line plots for selected flow conditions where the ordering of particle sizes from inside wall to outside wall are changing, and cartoons of the different orders of separation where the bottom particle is the innermost streak position and the top particle is the outermost streak position.

A more quantitative assessment of the potential for the separation of the particle sizes presented here is summarized in Figure 5-8 using a correlation coefficient ($1-R^2$) between the intensity profiles for each particle size at each of the flow conditions. A value of 1 indicates that the two distributions have no correlation and thus high separation potential and a value of 0 indicates that the two distributions are identical and therefore no separation potential. Excellent separation is defined as when the separation potential value is greater than 0.9 (grayed area).

The graphs from left to right (first row then second row) in Figure 5-8 increase in curvature value and have three lines depicting the separation potential between the different combinations of particles (green with red dash represents the separation

potential between λ=0.149 and λ=0.225, blue with green dash represents the separation potential between λ=0.066 and λ=0.149, and red with blue dash represents the separation

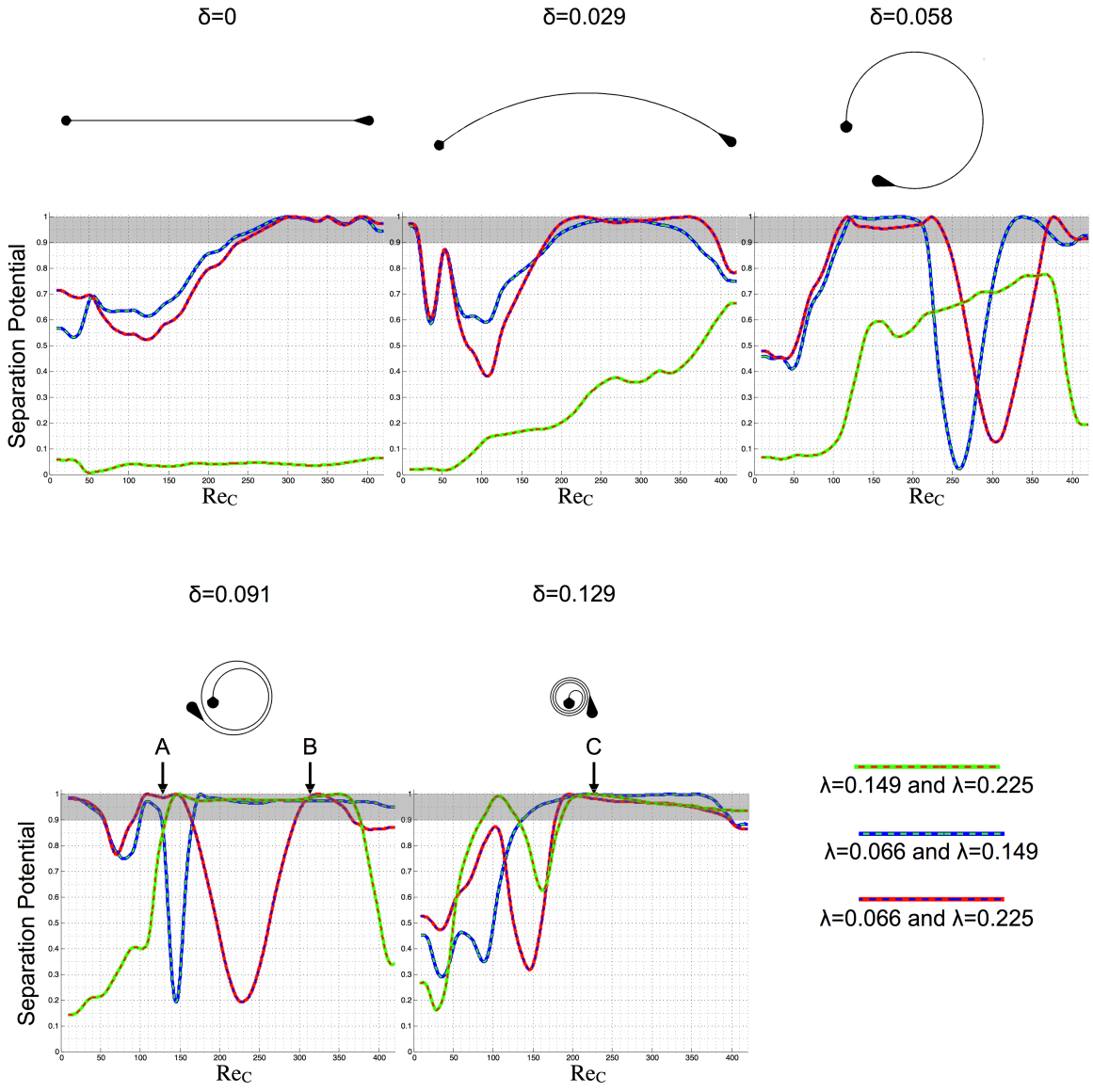

Figure 5-8: This figure presents the separation potential values for each device as Re_C is varied. Flow conditions where all three separation potential values are high indicate a regime where all three sizes can be separated and correspond to the regimes highlighted in Figure 2 (specific conditions marked A, B, C).

potential between λ=0.066 and λ=0.225). The straight channel (δ=0) allows for minimal separation between the larger particles since the focus to the same locations at the center of the channel width. The separation between the small particles and both larger particles

are therefore closely related. They only reach a significant value at higher Re_C when the small particles begin to exhibit five lateral streaks, four of which do not intersect with the distributions of larger particles and thus there is a higher separation potential although the equilibrium positions are overlapping.

When δ is 0.029, the high separation value is improved since small particles begin to exhibit single point lateral focusing near the inside wall. At higher Re_C, the small particles not focused into the innermost equilibrium position begin migrating to the outer half of the channel and overlap with the larger particle streaks leading to a dip in separation potential. Further increasing the curvature to δ=0.058 causes the smaller λ=0.066 particles to focus initially on the inner half, shifting to the outer half of the channel further with increasing Re_C. This occurs simultaneously with the migration of the larger particles towards the inside wall. The separate dips in separation potential between the λ=0.066 and λ=0.149 particles and at slightly higher Re_C between the λ=0.066 and λ=0.225 indicate the regimes where the streaks shift past one another trending in opposite directions. In this same flow regime the separation potential between the two larger particle sizes is increasing as the ratio of forces (inertial lift to Dean drag) is different between the two sizes.

The dips for the passing streaks (λ=0.066 with both other sizes) shift to lower Re_C values with the next increase in δ to 0.091. This device is the first device that exhibits excellent separation potential between the λ=0.149 and λ=0.225 particles as the λ=0.149 move into the innermost lateral equilibrium position and the λ=0.225 do not make that jump until the highest Re_C values. Finally, at a δ value of 0.129 you have high separation potential between all three sizes as the λ=0.149 particles now start shifting towards the

outer half of the channel and the λ=0.225 particles moving into the inner most lateral equilibrium position. The best separation between all of the particles at the same flow conditions occurs in the regime of the δ=0.129 device above a Re_C value of about 200. The other specific separation examples depicted in Figure 5-7 (A, B, and C) are marked on the respective plots.

Case C in Figure 5-7 depicts the previously understood fractionation style of Dean flow assisted inertial focusing separation [90, 91]. The other two arrangements of particle lateral positions A and B cannot be described by a simple balance of two forces (inertial lift and Dean drag).

5.5 Three-Dimensional Behaviors and Single-Point Focusing

The motivation for this section originates from the lack of a satisfactory answer for the change of equilibrium position with δ at a fixed Re_C value and λ. The current understanding of this motion dictates that particles equilibrate to the positions of z/h=±0.3 and stay at these height locations due to the stronger shear gradient along the vertical axis compared to across the width. The motion of the streak outwards is therefore the consequence of the effect of the inner wall as Reynolds number increases faster than the Dean flow. This makes sense up to a streak position near the centerline but moving past the middle would presumably be stopped by the same effect of the outer wall. Also, if we assume that the wall force is only affected by the confinement and Re_C, the motion of the streak in both directions with increasing delta (constant Re_C and λ), first inward towards the center of curvature and then outward at the highest delta values, should not be possible. One possible explanation would be if the particles were changing vertical positions within the channel thereby altering the Dean drag by being exposed to

significantly different Dean flow velocities and even different direction. For this reason, a qualitative investigation of the positions of the particle streaks along the height of the channel was performed using high-speed imaging. Particles that are in focus appear as a dark ring around a bright center. A particle further from this focal plane becomes darker in the center the further away it is located until it goes out of focus. Using this concept, the focal plane was set when the top stream of particles came into focus (at the lowest flow rate where focusing was achieved) and images were captured at several different flow conditions for each device. While the analysis is very qualitative it was able to tell the difference between a single streak along the vertical axis versus two distinct streaks.

The dark gray highlighted results in Figures 5-2 and 5-3 turned out to be conditions of note as they are not only the closest approach of the streak to the inside wall of the channel but are indeed conditions at which single z-position (height) focusing is achieved. This type of high quality focusing is important for not only the high precision positional focusing but also due to the correlation between this single point focusing and consistent longitudinal ordering between particles [66, 73]. For the current data set these single point focusing conditions also represent the minimum streak width over the entire parameter space for each particle size (λ=0.066 – Streak Width~1.36a, λ=0.149 – Streak Width~0.91a, λ=0.225 – Streak Width~1.01a). Figure 5-9 presents exemplar high-speed imaging still frames at different flow conditions to verify the single z-position nature of particle focusing. For λ=0.225, the transition to single point focusing is most evident in the δ=0.129 device at $Re_C \approx 150$, for λ=0.149 in the δ=0.091 device at $Re_C \approx 150$, and for λ=0.066 in the δ=0.029 device at $Re_C \approx 200$. Not all of the small particles are forced to a

single point in this device as previously mentioned. However, the existence of the streak near the inner wall indicates that the equilibrium position is present but perhaps the

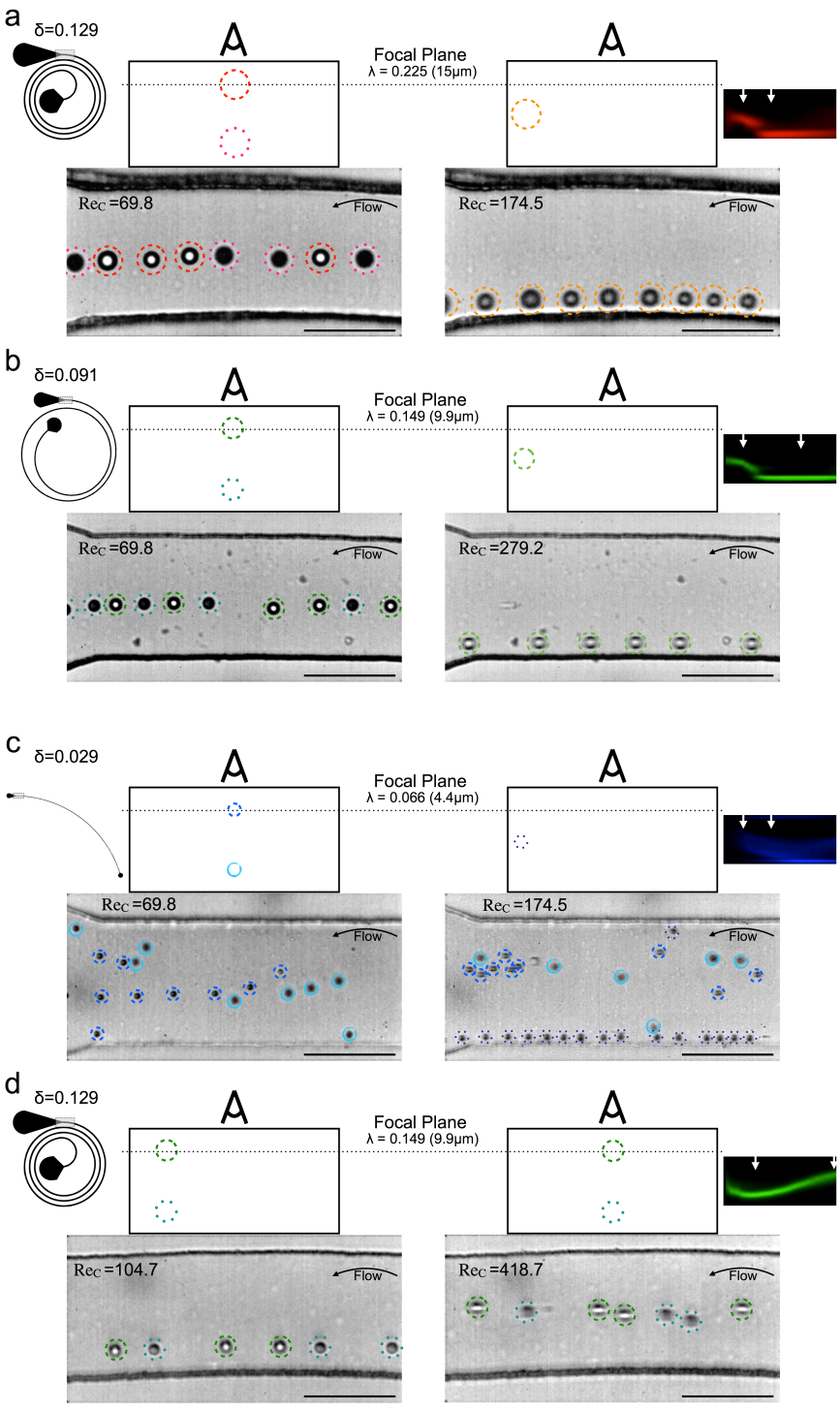

Figure 5-9: This figure shows example high-speed video stills (2μs exposure time) for different flow conditions before (left) and during (right) single point focusing is achieved at the inside wall for each of the three particle sizes (a) λ=0.066, (b) λ=0.149, (c) λ=0.225 with associated schematics of the channel cross-sections with assumed vertical positions. (d) Example high-speed video stills for the λ=0.149, δ=0.129 case where the single point focusing position is bypassed and two vertical equilibrium positions always exist.

channel was not long enough for all particles to traverse to this position. It is also possible the curvature ratio is slightly less optimal. Figure 5-9d presents similar high-speed imaging data for the case of λ=0.149 and δ=0.129 where the streak of particles instead of continuing to the innermost equilibrium position begins to migrate towards the outer half of the channel never actually changing from two mirrored vertical equilibrium positions.

The vertical positions of the streaks may be changing less than what is detectable using the high-speed video analysis. Therefore, another method was utilized to investigate smaller changes in this position that may be occurring even without Dean flow [108]. This was accomplished using a straight channel of opposite aspect ratio (100μm tall and 50μm wide) and investigating the fluorescent streak behavior. Figure 5-10 summarizes the results from this experiment, which shows that the streaks are actually changing in position in the shorter dimension as Re_C is varied. The equilibrium position here is defined as the average distance from the centerline of the channel to the center of the particle streak. The λ=0.066 particles start at z/h=0.26 move towards the wall until Re_C =140 and z/h=0.30, which is equivalent to the well known 0.6*radius given by Segre and Silberberg [37], then decreases with increasing Re_C to z/h=0.21 at Re_C 419. The λ=0.149 particles start at z/h=0.28 move towards the wall until Re_C=209 and z/h=0.30, then decreases with increasing Re_C to z/h=0.27 at Re_C=419. The z-position of the λ=0.225 particles show the least dependence with Re_C start at z/h=0.24 move

inconsistently towards the wall until Re_C =174 and z/h=0.25, then decreases slightly with increasing Re_C to z/h=0.22 at Re_C =419.

While the streak position measured using the analysis described in section 3.6.1 seems strange since the smaller particles equilibrated closer to centerline than larger particles, oppositely of what was expected, the location of the peak intensities for the different streaks, as in Figure 5-10c (dashed lines), more closely resembles that of Di Carlo (2009) marked with the colored arrows on the right side of the plot. One difficulty with this analysis, and the possible reason for the difference in streak position measurements, is the appearance of side streaks (located at the z/h=0) as Re_C increases as seen in Figure 5-1 in the straight channels [54]. These streaks were subtracted out using a parabolic background subtraction algorithm in order to investigate the streak positions at the center of the larger channel dimension more clearly. Despite this subtraction, there was some bias towards z/h=0 of the intensity profiles which make come across as a streak shift in the z-direction. This background fluorescent was lower in magnitude for the smaller particles as they are more out of focus and generally less intense in fluorescence (scales with volume of particle at equivalent exposure) than the larger particles.

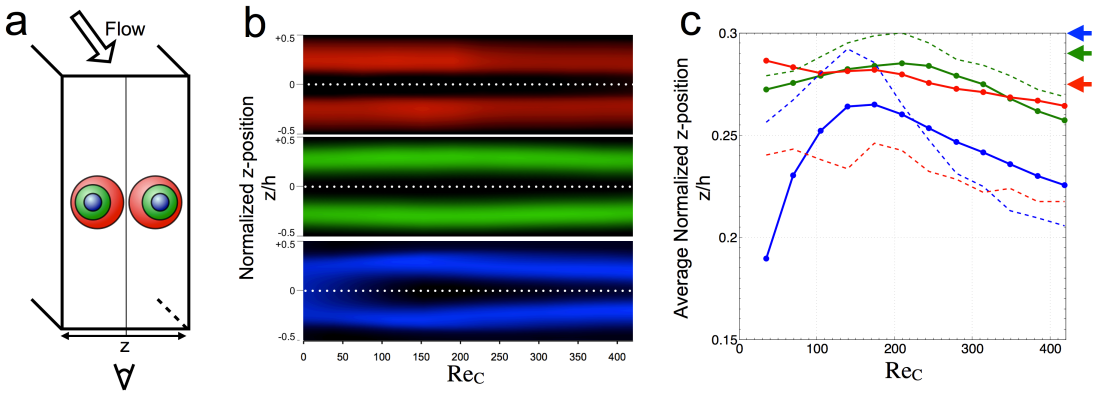

Figure 5-10: Measured streak positions in z-direction using 100µm high and 50µm wide straight (δ=0) channel. (a) A schematic of the channel orientation and expected particle positions. (b) The ReC map for

the z equilibrium position behavior and (c) a summarizing plot of the average z_{eq} of each pair of streaks where the solid line indicates the streak position as the middle of the streak width and the dashed line is the position of peak intensity. Note: A parabolic background subtraction was used to remove the additional intensity caused by the side streaks appearing at higher Re_C which was located at z/h=0.

Through the separate variation of Reynolds number, Dean number and particle confinement ratio we were able to detail new regimes of inertial focusing based separation utilizing the competing effects of the three distinct parameters. These new separation regimes indicate that it is possible with simple curved channels to separate particles of an intermediate size (bandpass filtration) and isolate a particle size of choice by varying flow rate. It is also of note that we show that single point particle focusing is possible in simple curved channels not requiring the more complicated structures required for the other known techniques for sheathless alignment of particles [70, 80, 81, 112].

Most significantly, we have visualized two separate regimes of particle focusing for which single point equilibrium positions are a transition between the two regimes. This previously undetailed nature of inertial focusing incorporates a complex balance of forces at the lateral and vertical equilibrium positions within the cross-section that are a function of all of the parameters investigated.

5.6 Mechanism of Transition Between Inner and Outer Focusing

The positional variation of inertial lift and Dean drag forces will always be a complicating factor for the generalization of results from inertial focusing experiments in curved channels [49, 54, 56]. While the complete description of the mechanism behind the transition from inner to outer focusing requires more precise vertical measurement of

particle position within the cross-sections of curved devices and either locally dependent lift coefficients or numerical simulation, we offer our hypothesis given the current results.

The addition of curvature to microchannels not only adds Dean drag to the force balance but also changes the shear gradient through the redistribution of the velocity profile [86]. This redistribution caused by Dean flow is present at the Dean numbers tested in the majority of similar published investigations of separation in Dean flow assisted inertial focusing, De>10. This redistribution is occurring at the same time as the vertical particle equilibrium positions are changing with Re_C as shown in Figure 5-11. There have been conflicting results on the variation of the vertical equilibrium position, which had been previously theorized in pipes [50] and rectangular cross sections [52]. However, both investigations in rigid channels, including the current report, have shown some type of variation in this equilibrium position with Re_C [108]. There is also numerical evidence of this phenomenon in pipes although their model predicts larger particles will transition to an inner annulus at lower Reynolds numbers than smaller particles, the opposite of what is seen in the current channel flow [51]. The evidence in PDMS channels indicates that this motion of the particle streak away from the center of curvature happens without a vertical position change and is simply due to the scaling of Dean drag, $U_{Avg}^{\sim 1.8}$, being lower than the scaling of inertial lift U_{Avg}^2 [78, 92, 113]. There is also evidence that the inertial lift may not increase with U_{Avg}^2 due to a decrease in the lift coefficient with $Re_C^{0.5}$ [49, 56, 114]. In our hypothesis, we predict that both effects, vertical position change with Re_C and the balance of Dean drag and inertial lift accounting for the velocity redistribution can explain the behaviors presented.

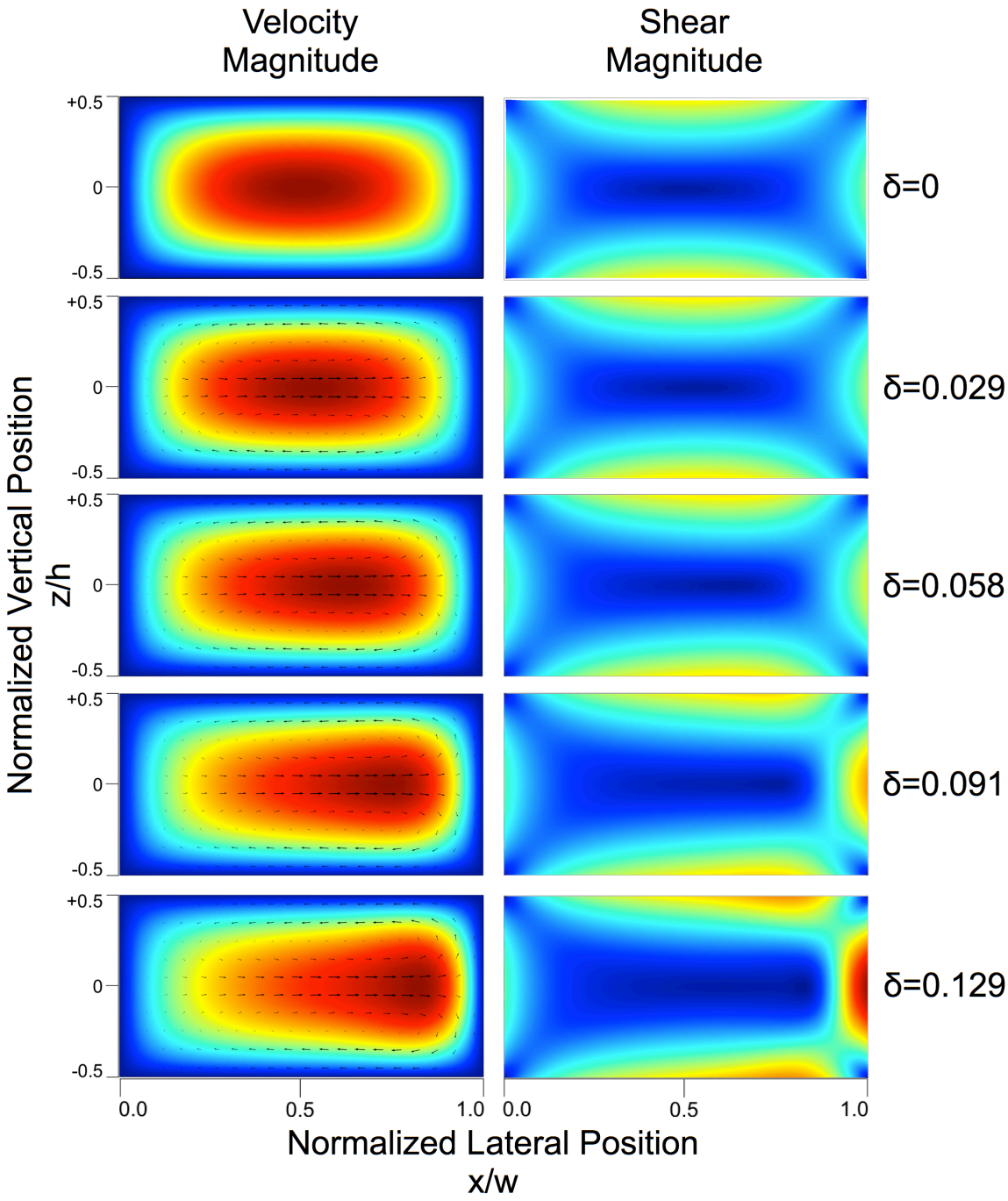

Figure 5-11: Simulated velocity profiles with normalized Dean flow vectors are given (left) as well as the corresponding normalized shear gradient surface plots (right). The flow conditions presented are for Re_C=419.

Figure 5-12 summarizes these effects and the transition between regimes of focusing behavior by extrapolating the lateral and vertical equilibrium position results (Figure 5-1 and Figure 5-10) to the different curvature ratio devices. In general, the mechanism

depends significantly on the previous understanding of inertial lift but improves our understanding of the three-dimensional variation of the forces in curved channels. Figure 5-11 shows the velocity profiles for the different δ values at Re_C=419. Overlaid on these profiles are normalized Dean flow vectors indicating the direction of the Dean flow and the magnitude relative to the maximum value for each δ although the actual Dean velocity magnitudes increase with $\sim\delta U_{Avg}^2$. The next column of plots shows the local shear gradient magnitude for each of the curvature cases. As the velocity profile morphs with increasing curvature, the shear gradient on the inner third (left) of the channel drops. This drop combined with the increased wall effect lift at higher Reynolds number allows particles to have a vertical equilibrium position closer to the centerline at or beyond the zero Dean velocity line at ±0.2z/h. After this switch in vertical position the particles are exposed to Dean velocities or wall effect forces directed away from the center of curvature with only the shear gradient lift as a counter balancing force. Considering the decreased shear gradient on the inner third of the channel, compared to the parabolic profile in the δ=0 case, the wall effect and Dean drag cause the streak to move outwards away from the center of curvature until the shear gradient becomes high enough to counter the Dean drag force. This regime would tend to act as the early descriptions of Dean flow assisted inertial focusing fractionation. In the other regime where the streaks move towards the center of curvature with increasing Re_C, the particles are exposed to Dean flow directed towards the inner half of the channel. The motion of particles here should scale differently as the countering forces are mostly due to the wall effect rather than a non-parabolic velocity profile.

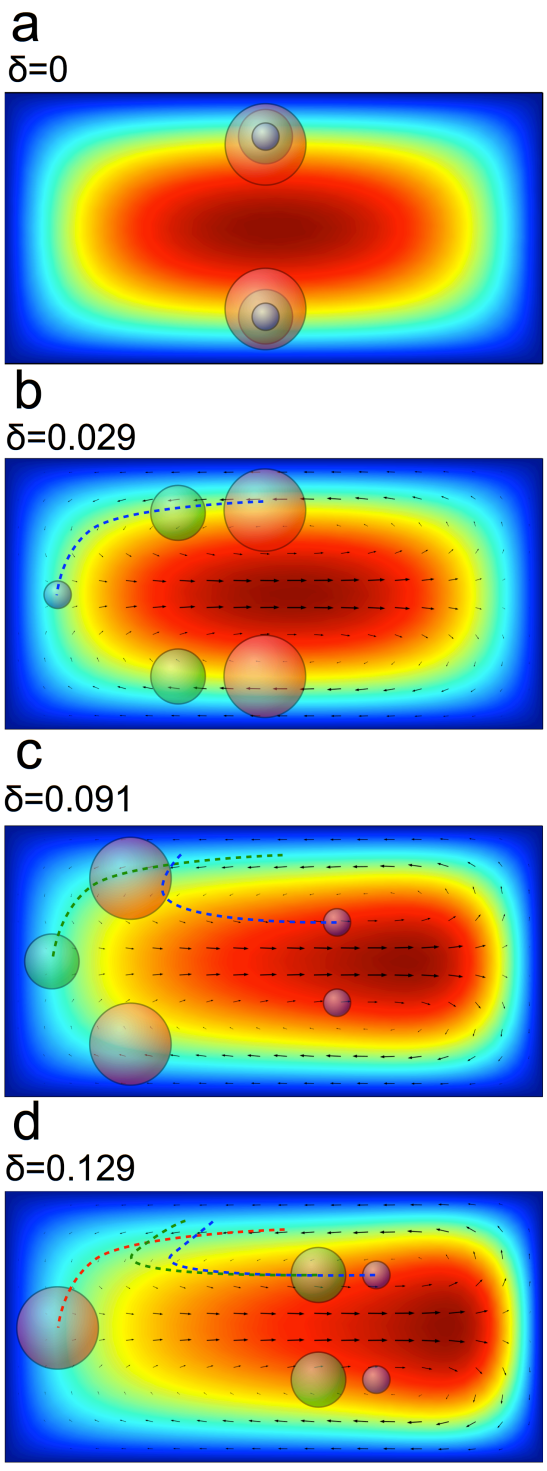

Figure 5-12: A series of 4 cases showing the idealized focusing (a-d) of the three different sizes of particles (λ=0.066 blue, λ=0.149 green, λ=0.225 red) in a straight channel (δ=0) and increasing in curvature from top to bottom showing the three single point focusing cases and the hypothesized shifting of the equilibrium positions with increasing Reynolds number based upon the data presented in Figure 5-1 and 5-12 (dashed lines).

The dependence of this hypothesis on size is also intriguing and is presented graphically in Figure 5-12 a through d. The motion away from the walls at higher Re_C in the vertical dimension would cause the smaller particles to first move into the oppositely directed Dean flow causing them to move towards the outer half at lower δ values than the larger particles. The larger particles require a higher δ value such that the velocity profile is redistributed enough to decrease the vertical shear gradient lift force in such a way to allow for a large enough shift in vertical equilibrium position to have the particles be exposed to the Dean flow directed away from the center of curvature. This will eventually happen for the largest particles as well but did not occur within the current parameter space. The range of conditions where single point focusing is achieved is still difficult to explain without more vertical position information or greater δ resolution but could be a small subset of the regime where the shear gradient lift towards the wall is still high enough to force a trajectory of a migrating particle to this innermost equilibrium position. At some point the Dean drag in addition to increased wall effect force then destabilizes these trajectories and causes the equilibrium position to begin shifting outwards at a different vertical position. It is curious that there seems to be such a large set of operating conditions where this single point focusing behavior is prevalent.

5.7 Conclusion

The description of two separate motions of particles in different focusing regimes is a significant advancement of the understanding of inertial focusing in curved channels. Not only does this have implications for the design of future devices for separation applications but the ability to significantly confine an arbitrarily sized particle to a single equilibrium position in a simple curved channel also will be useful for studying inter-

particle forces in curved channels. Knowing these optimal regimes of inertial focusing will allow for the study the effect of concentration of particles on the focusing efficiency and equilibrium spacing between particles at this single equilibrium position and how these values are adjusted by Re_C. With further improvements to this data set for the inclusion of three-dimensional positioning of the particle streaks within the curved channels will hopefully be able to verify the mechanism for the different focusing regimes described here.

Chapter 6

Modeling of Inertial Forces in Curved Channels

6.1 Overview

In order to investigate the driving mechanisms and relative effects of the forces in curved channels, especially in three dimensions, it is necessary to study idealized systems where the individual components of the forces are able to be measured unlike in experimental systems. This has been accomplished historically through the investigation of the Navier-Stokes equations of motion for fluids. While analytical solutions for the forces can be developed in simple geometries, each makes certain assumptions and simplifications that affect the applicability of the results, such as using an infinitesimal point particle that does not affect the flow field or assuming the system is two-dimensional (pipe flow or flow between parallel plates). However, the data presented in Chapters 4 and 5 are in regimes where these assumptions are invalid. Direct numerical simulation of the Navier-Stokes equations allows for the calculation of the forces and flow velocities involved without making these assumptions. This chapter presents an improved finite element model of curved channel inertial focusing systems as well as preliminary results of the force fields that determine equilibrium inertial focusing behavior [55]. The major improvement over the previous model upon which this work is based is the incorporation of the redistributed velocity profile caused by Dean flow and its effect the force measurement on a particle in a confined flow.

6.2 Background

As described in Chapter 2, both theoretical and numerical approaches have been applied successfully to inertial focusing flows. While theoretical methods require restrictive assumptions numerical methods offer full simulation of the Navier-Stokes equations as long as computational power is available [43]. These results have helped build an intuitive understanding of the forces which cause inertial focusing in straight channels. With the wealth of experimental data for the surprising behaviors in curved channels it is only logical to attempt to gain similar intuition for these flows and understand the dominant cause behind the switch in focusing behavior described in Chapter 5. Without direct evidence of the vertical equilibrium positional shift in curved channels due to velocity redistribution, numerical modeling of the forces is one way to investigate the differences in equilibrium position between redistributed normal velocity profiles.

There has only been a single model built for inertial focusing in curved channels. In this model, a flow field was solved for a given 3D channel geometry and flow parameters. Then a transient particle tracing simulation was run in which force equations are solved for given the instantaneous velocity of the particle and the adjacent fluid flow. The force equations known as the BBO equations (Basset, Boussinesq and Oseen) assume the particle to be small and thereby having minimal effect on the surrounding flow [115]. The particle is placed at an initial position and is updated over time given the force calculations which include buoyancy, centrifugal, added mass, Stokes' drag and pressure gradient effects are summed and applied to the particle. Over time these particles

will equilibrate to an equilibrium position within the flow. These simulations were accomplished at Re_C=10 and De<1 [100, 115].

The model presented here investigates the steady state forces on a finite sized particle through direct numerical simulation of the flow field with a particle including the effect of the particle on that flow field which has been shown to significantly affect the associated inertial forces [55]. The next section will describe the numerical model and solution procedure utilized herein.

6.3 Model Description and Process Flow

The procedure for solving for the forces on a finite sized particle in a curved channel is actually comprised of two separate models and two iteration loops as summarized in the process flow diagram in Figure 6-1. In general, the solution procedure follows similarly to Di Carlo et al (2009) using COMSOL Multiphysics 4.3a finite element software [55]. Both models solve the Navier-Stokes equations with the continuity equation in different forms. The first model, referred to as the flow model, is used to obtain the Dean flow solution for a channel with a given radius of curvature, *r*, width, *w*, and height, *h*, as well as an average flow velocity U_{Avg}. This two-dimensional axisymmetric model solves the incompressible Navier-Stokes equations given a volumetric force, f_{Vol}, applied to the fluid perpendicular to the cross section.

$$\nabla \bullet \mathbf{u}_1 = 0 \tag{6.1}$$

$$\rho(\mathbf{u}_1 \bullet \nabla \mathbf{u}_1) = -\nabla p + \mu \nabla^2 \mathbf{u}_1 + f_{Vol} \tag{6.2}$$

The boundary conditions are $\mathbf{u_1}$=0 at the walls ($x = r \pm w/2$ *and* $z = \pm h/2$) where r is the radius of curvature, and *h* and *w* are the height and width of the cross section respectively. The walls will vary with distance from the central axis of symmetry

effectively changing the curvature ratio of the channel being modeled. To ensure the flow rate applied is equivalent between cases of different curvatures, it was necessary to use an adjustment parameter, α, which multiplies the volumetric force to account for the higher flow resistance of higher curvature channels [85, 116]. The α_{Final} value was approximated using a cubic interpolation of the measured average fluid velocity $U_{AvgMeasured}(\alpha)$.

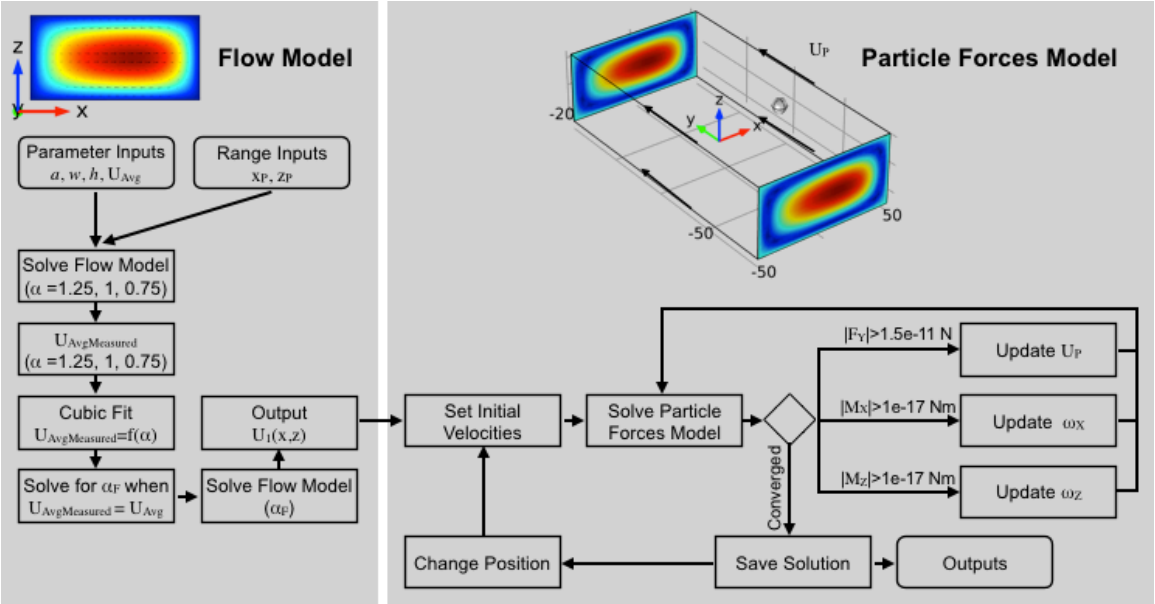

Figure 6-1: Process flow diagram for the current numerical model solution procedure. Process begins on top left with the input of parameter values and ranges and is completed when all particle positions have converged solutions on the bottom right.

This final value was then used in producing the final velocity profile, $\mathbf{u_1}(x,z)$. The y-directional or axial components of $\mathbf{u_1}$ were then used as an inlet and outlet condition for the second model, referred to as the particle forces model. The x and z components of the velocity, the secondary flow, are saved for later use. In this manner, the effects of the redistributed velocity profile are retained in the particle forces model. The reason for this necessary simplification is discussed later.

The particle forces model solves the three-dimensional incompressible Navier-Stokes equations taking an Eulerian frame of reference of a single suspended neutrally buoyant particle whose location is fixed within a short section of a straight channel. The equations

of motion are identical to Equations 6.1-6.2 except now in three-dimensional Cartesian coordinates and without the volume force. The section of channel in the particle forces model was set to be 20 times the particle diameter in length and the origin of the model is placed at the center of the channel section. The walls of the channel move at the presumed particle velocity U_P, and the steady state axial velocity profile for a given curved channel $u_{1y}(x,z)$ is applied as the inlet and outlet boundary conditions minus U_P. The initial value for the particle velocity, $U_{P,0}$, is taken to be the free stream velocity of the fluid if the particle were not in the model $u_{1y}(x_P,z_P)$. These boundary conditions are summarized in Equations 6.3-6.5.

$$\mathbf{u_2}(x, y = -10a, z) = U_{P,0}(x_P, z_P) - \mathbf{u_{1}}_y(x, z) \tag{6.3}$$

$$\mathbf{u_2}(x, y = 10a, z) = U_{P,0}(x_P, z_P) - \mathbf{u_{1}}_y(x, z) \tag{6.4}$$

$$\mathbf{u_2}(x = \pm w/2, y, z = \pm h/2) = U_{P,0}(x_P, z_P) \tag{6.5}$$

A spherical particle is placed as a void in the mesh of diameter *a*, at a specified particle position (x_P, z_P) within the cross section equidistant from the inlet and outlet (y_P=0). The particle is allowed to rotate using the following surface velocities as a boundary condition at the particle surface Equations 6.6-6.8 which are given an initial values as shown in Equations 6.9- 6.11 [55]. This completely defines our boundary conditions.

$$\mathbf{u_{2}}_x\Big|_{sphere} = (y - y_P)\omega_z - (z - z_P)\omega_y \tag{6.6}$$

$$\mathbf{u_{2}}_y\Big|_{sphere} = (z - z_P)\omega_x - (x - x_P)\omega_z \tag{6.7}$$

$$\mathbf{u_{2}}_z\Big|_{sphere} = (x - x_P)\omega_y - (y - y_P)\omega_x \tag{6.8}$$

$$\omega_{x,0} = \left(0.6\frac{z_P - h/2}{h/2}\right)^2 \frac{4\,\mathrm{Re}_C\, U_{P,0}}{D_h/2} \tag{6.9}$$

$$\omega_{y,0} = 0 \tag{6.10}$$

$$\omega_{z,0} = \left(0.6\frac{x_P - w/2}{w/2}\right)^2 \frac{4\mathrm{Re}_C U_{P,0}}{D_h/2} \tag{6.11}$$

Along the length of the particle forces model section of channel it is expected that the applied velocity profile slowly morph back into the straight channel solution for the given channel geometry but this change was limited by the channel length and the same applied velocity profile at the outlet. Both model geometries are shown in Figure 6-1 with an example solution from the flow model (left) being applied at the inlet and outlet of the particle forces model (right).

After the initial solution is complete, the force measurements are accomplished through the integration of surface forces over the element boundaries that make up the sphere in the model. In this manner, both shear and pressure derived forces are counted into a resultant force vector (F_X, F_Y, F_Z) and moment vector (M_X, M_Y, M_Z). The force in the y-direction, F_Y, is then used to update the wall velocity, U_P, and the moments about the x and z axes, M_X and M_Z, are used to update the particle rotational velocities in those directions, ω_X and ω_Z. These updates are accomplished using a damped iterative procedure with the goal of achieving force free translation (F_Y=0) and torque free particle rotation (M_X=M_Z=0). The particle rotational and translational velocities are updated and the forces are recalculated until the values converge based upon a minimum force ($1.5\text{x}10^{-12}$ N) or torque value ($1.0\text{x}10^{-17}$ Nm). The final particle conditions U_P, ω_X, and ω_Z, allow for the lateral inertial forces to be measured (F_X and F_Z). The particle position is then changed and the iteration procedure begins again.

Once these forces are calculated at all the positions within the channel cross section, a separate Matlab routine is used to account for the drag induced on a particle by the

secondary Dean flow. The velocities from the flow model are used to calculate the drag on a sphere assuming Stokes' drag on a point particle as defined in Equation 6.12.

$$\vec{F}_{DeanDrag} = 6\pi\mu a\vec{U}_{Dean}(x_P, z_P) \tag{6.12}$$

This does not take into account the effect of finite particle size on the secondary flow field. An example solution image is shown in Figure 6-2 for a δ=0.091 and Re_C = 100 case where the integrated forces on the surface of the particle are highlighted.

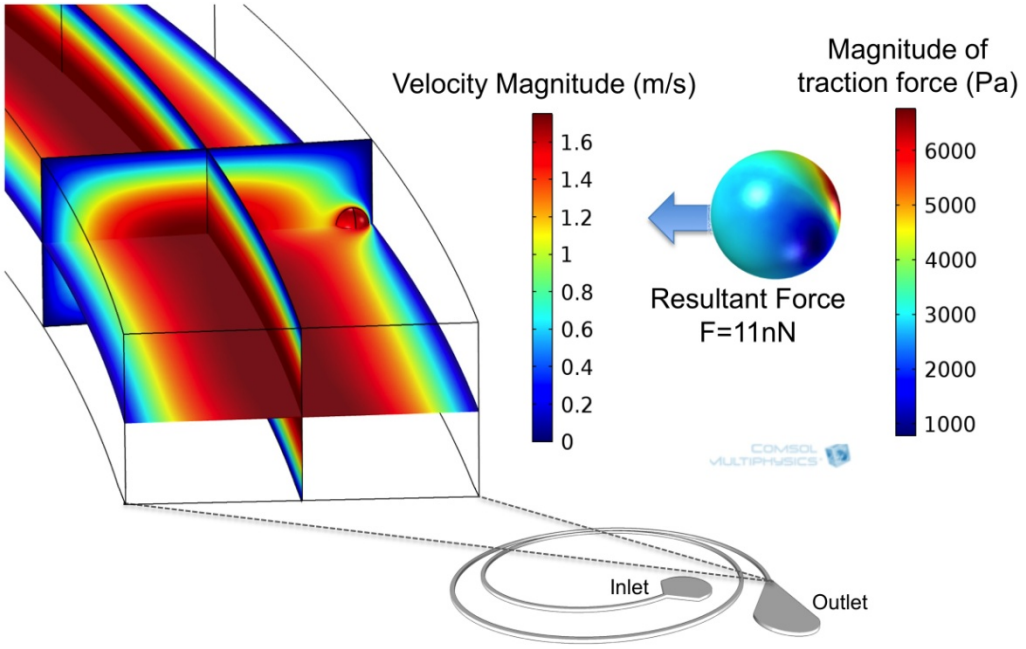

Figure 6-2: Velocity profiles (left) and surface traction forces (right) on a particle at non-equilibrium position where the wall effect is dominant.

6.4 Model Validation

The model was first validated against an established solution for straight channel flow in a 50µm square cross section channel [55]. In this case, the equilibrium particle positions are known to be centered on each face of the square and 10µm away from the walls for a 10µm diameter particle at a channel Reynolds number of ~20. Both the magnitudes and equilibrium positions were consistent with the prior result as shown in

Figure 6-3. The variation with Reynolds number is also similar to numerical results given by Asmolov [1999] as the equilibrium position shifts towards the inside wall and the magnitude decreases with increasing Re_C [49]. The data is presented in non-dimensional force defined in Equation 6.13.

$$f_L = F_L \rho U_{Max}^2 a^4 / D_h^2 \tag{6.13}$$

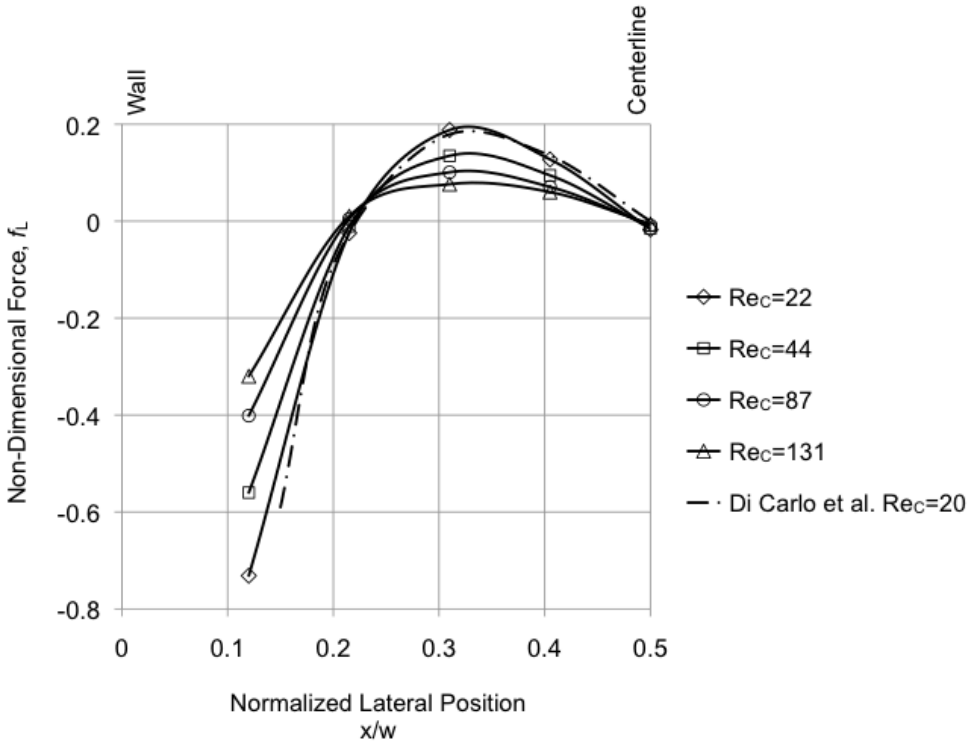

Figure 6-3: Comparison of Di Carlo et al. (dotted and dashed) to the results from the current model (solid) [55]. Different Reynolds number results are differentiated by marker.

It was also necessary to check the validity of the application of the boundary conditions for the second model. For this verification the particle was removed from the second model and the velocity profile was measured at y=0. This was compared to the boundary condition ($u_{1y}(x,z)$) for several different Re_C and curvature values. While the profile did change proportionally to the Reynolds number and curvature as expected the short section length allowed for less than a 20% change in velocity at any position at any

flow conditions. While not ideal, the velocity profiles are still redistributed relative to the straight channel solution in each case.

6.5 Results and Discussion

We then compared the model predictions to experimental measurements for both straight and curved channels that are 50μm tall, 100μm wide and 4cm long. Figure 6-4 shows straightened images from experimental data and cross sectional simulation results for a channel Reynolds number of 100 and three Dean numbers: 0, 6 and 9 (the channel is straight when the Dean number is zero).

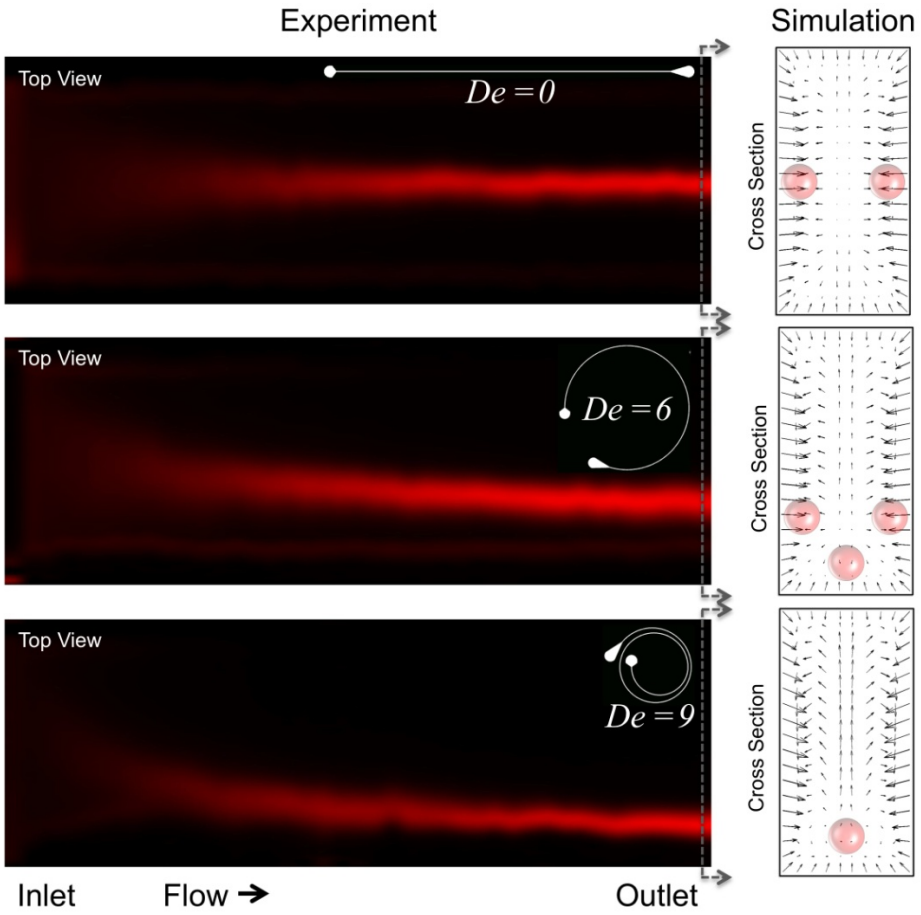

Figure 6-4: Experimental fluorescent microscope images (left) of the longitudinal section of the microchannels showing the distribution of particles along the channel. The cross-section plots (right) show the simulated resultant forces on the particles. The simulated equilibrium positions are marked by the particles and they closely match the experimental results. The data is shown for the same Reynolds number in three microfluidic devices of different curvatures. The curvature of the device is indicated in the inset seen in the upper right corner of the fluorescent images.

For each case, we show the particle distribution along the channel length collected using fluorescent streak microscopy and the force field calculated for that cross section with the equilibrium positions (net force = 0) highlighted. The simulation results are in fairly good agreement with experimental measurements for all three cases, and illustrate the dependence of the equilibrium positions on the channel curvature.

With this model we then investigated a number of different solutions for specific flow conditions from Chapter 5, each requiring a significant amount of computational time depending on the positional resolution and minimum force thresholds (increasing time with increasing positional resolution and decreasing minimum force thresholds). Figure 6-5 shows a set of results for Re_C=174 and the different curvature values used in Chapter 5. The color indicates the magnitude of the normalized force field to a power of 0.3 ($\left|\vec{F}\right|^{0.3}$) accentuating the true force minima (blue). Only the bottom half of the channel was simulated as the top half is the mirror image.

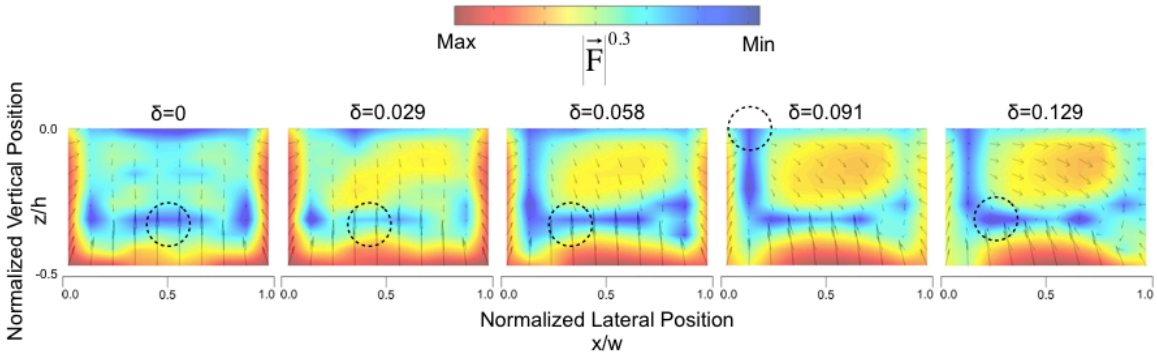

Figure 6-5: Force fields for Re_C=174 and each of the different curvature values investigated in Chapter 4 (from left to right, δ=0, 0.029, 0.058, 0.091 and 0.129). The color indicates the normalized magnitude of the summed forces on a particle at each position and the vectors indicate the magnitude and direction of the summed forces at the different positions. The dashed circle indicates the location of the expected equilibrium position at the given flow conditions extrapolated from Chapter 5.

The left of each force field is the inside wall of the channel curvature. The straight channel (δ=0) looks as expected with the 8 force minima (plus the centerline of the

channel) like those showed by Chun and Ladd [52]. It is not elucidated here why the corner positions are not seen experimentally at Re_C=174. The corner positions may represent metastable states where particles are only present for short durations before shifting to more stable equilibrium positions at the center of each channel face.

The minimum force zones are continuous rather than at discrete positions when investigated closely and either a more refined mesh, lower minimum force thresholds or increased positional resolution are required to perfectly define the simulated equilibrium positions.

The loss of the equilibrium position at the center of the bottom wall is unclear at increasing curvature. However, the sensitivity to vertical location is seen to increase slightly as the regions where the force is at a minimum at this location seem to shrink with increasing curvature (left to right). The widening of the force minima at the inside wall does seem to reflect the transition of particle focusing to the inner most equilibrium position but the corresponding transition to outer half particle focusing is not as obvious at this moderate Re_C value.

6.6 Most Recent Update

While the simulation as presented takes into account a portion the redistributed velocity profile and the effect of particle confinement on this profile, the Dean force is calculated assuming a point particle (drag velocity is the transverse velocity at the center of the particle) rather than taking into account the particle's effect on the Dean flow. At higher Dean numbers this effect could become significant as the Dean flow velocities are in the range of velocities (~0.3m/s) where the particle Reynolds number based upon this velocity is now approaching unity. While we do not see this effect apparent on the

particle equilibrium positions it may have an effect on the z position locations as well as the dynamics of the particle equilibration.

The most recent improvement to the code incorporates a rotating reference frame with an additional volume force accounting for the coriolis and centrifugal forces. This allows for the full direct numerical simulation of the flow through a curved channel with the reference frame rotating opposite the particle motion to take the viewpoint of the particle. This was accomplished through the addition of a volume force dependent on the particle velocity (reference frame rotation rate) and the fluid velocities.

6.7 Conclusions

There is a clear need for better understanding of the balance of forces behind the motion of the equilibrium position with Reynolds and Dean numbers. The tool developed here is one step towards this better understanding and improved design for biomedical applications. This is a first attempt to comprehensively modeling the effect of channel curvature on the inertial forces imposed on a particle with direct numerical simulations. Continued development and investigation of the results from this model will be able to explain the results from Chapter 5 in terms of both the z-position variation and Dean number, hopefully, elucidating a dominant component.

Further improvements around the model itself will be necessary for its future success. The code, in its current form, is unfortunately biased towards a particle size of 10μm. For understanding and modeling particles of different sizes and channels of different cross sections this reliance on absolute thresholds must be changed to a non-dimensional form. The effect of these thresholds across the current results can be seen in the variations in the straight channel result. There are clear asymmetries that should be diminished with

improved position and mesh resolution. The current meshing parameters were chosen by investigating the point of diminishing return in terms of solution time per position and memory.

Chapter 7

Conclusion and Outlook

The field of inertial focusing is continuing to grow at a rapid pace. Since the 2007 article by Di Carlo et al, more than 27 research groups worldwide have published at least one journal article about inertial focusing. These papers not only include improvements to the theory of inertial focusing but also some advanced and transformative uses of inertial focusing flows in biomedicine. These include the isolation of extremely rare circulating tumor cells from patient samples [117, 118] and the hydrodynamic stretching and mechano-phenotyping of cells for the detection of cancer and other maladies [65]. The field of inertial focusing is capable of having an even greater impact on the field of biomedicine and in order to do so a better understanding of the flows and forces at work is required.

This dissertation presents data on the inertial focusing behaviors in curved channels. An adjusted ratio of forces factor is defined using more accurate Dean flow velocities that improved the accuracy of the ratio for predicting the onset of inertial focusing in different width microchannels. An upper limit is indicated such that for a given channel length there is a maximum width above which focusing may not be achieved. This is presented through the fact that as channels increased in width, the operational parameter range within which focusing is achieved decreased in size.

The dynamics of inertial focusing along a spiral microchannel are also detailed. The streak width is found to be less dependent on the Dean number across many flow conditions but the streak position was greatly influenced by the Dean number. In general,

the focusing dynamics appear similar between an increasing and decreasing Dean number spiral. However, the formation of a particle free region at higher Dean numbers is made more evident through the comparison of the two cases.

Multiple regimes of inertial focusing behavior are detailed through the systematic study of inertial focusing by changing the three most relevant non-dimensional parameters; channel Reynolds number, particle confinement ratio and curvature ratio. The behaviors change with increasing curvature ratio starting with mid-channel focusing in straight channels followed by focusing towards the center of curvature, then by a regime of single point focusing and then focusing away from the center of curvature. The dependence on particle size is found to be different in these different regimes indicating the need for particle motion in the vertical dimension to account for the changes in behavior, essentially determining that inertial focusing in curved channels is a 3D phenomenon.

The transition between inner and outer directed focusing is determined to be a regime of single-point focusing in both the vertical and lateral dimensions and occurring at increasing curvature ratio with increasing particle confinement. This type of focusing of particles is normally achieved through the use of complex 3D structures and the ability to use a simple geometry to achieve the same type of focusing is an important result.

The motion towards and then away from the walls along the shorter dimension of a low aspect ratio microchannel are observed with increasing Reynolds number for different particle sizes confirming the results of Ciftlik et al [108]. This observation conflicts with previous numerical simulation that inner equilibrium positions are established at lower Reynolds number for larger particles [51].

Finally, it is discussed that a possible mechanism for the range of behaviors in curved channels is the summed consequence of both the Reynolds number variation in vertical position and the decrease in vertical inertial lift forces due to the redistribution of the velocity profile in curved channels. By moving further from the top and bottom walls due to this combined effect, the particles experience diminished or even oppositely directed Dean drag forces. A finite element model for measuring and discerning the separate force components due to the wall effect, Dean drag and shear gradient lift is presented for the validation of the proposed mechanism.

The intricate balance of forces at work for generating the discovered behaviors form the basis of a generalized concept that utilizes the reshaping of both the secondary and axial flow to adjust particle equilibrium positions in three-dimensions at high speeds. Additionally, the ability to control the dependence of these behaviors on particle size in different flow regimes can be applied not only to bandpass filtration shown here, but also to other examples of particle motion including size *independent* inertial focusing. These concepts can be extended to new types of flows and channel geometries in order to achieve novel flow patterning of high-speed particles. With further scientific exploration, the versatility of inertial microfluidics illustrated here can be morphed into the solutions for current and future biomedical engineering challenges.

As is typical of scientific research, this dissertation leaves more questions to be answered considering the conclusions and hypotheses stated herein. The clear next steps are to continue the development of a theory that can explain the different regimes of inertial focusing together or separately. Experimental validation of such a theory will require a technique such as digital holographic microscopy or confocal microscopy to

verify the vertical changes in equilibrium position within the curved channels. The motion of smaller particles away from a wall at lower Reynolds numbers than larger particles should also be more critically examined as this is the first evidence of such a behavior and opposite of that predicted theoretically. Finally, the variation of curvature along the length of a channel should be investigated. This type of variation and the associated understanding of the dynamics of focusing have the potential to provide size independent particle focusing at extremely high throughput. More generally, explorations into the control of shear gradients across a channel using electro-osmotic flow and viscosity gradients are intriguing possibilities for achieving true flow patterning of particles in inertial flows.

The applications of inertial focusing should be pursued concurrently with these proposed theoretical improvements. The ability to replace cumbersome biological fluid handling processes in hospitals throughout the world and even replacing centrifuges in resource limited settings could improve healthcare worldwide. The creation of optimized volume reduction inertial focusing devices enables new types of cancer and infection detection as rare and dilute cells become more accessible. Improved abilities to focus particles in three dimensions at high speeds without sheath flows should enable further improvements in cytometry systems as long as detection capabilities can improve simultaneously. However, these advancements in applications should not be limited to just the world of biomedicine. Numerous industries from wastewater treatment to ethanol production could benefit from particulate removal with the concepts of confined inertial flows. Inertial focusing is not just a microfluidic phenomenon and can have as large of an impact as the creativity of those willing to apply it in new ways.

Appendix A

Epoxy Fabrication Procedure with Images

Materials:

- PDMS microchannels for replica molding
- PDMS Sylgard 184 Kit – both elastomer and base (Ellsworth Asdhesives)
- PEEK Tubing 1/16 inch outer diameters and 0.03 inch inner diameter (Sigma-Aldrich)
- 0.75mm Harris Unicore punch (Ted-Pella)
- Teflon cord (.031 inch diameter) or Teflon coated wire (.028 inch outer diameter) (McMaster-Carr)
- Tridecafluoro – 1,1,2,2 – (tetrahydrooctyl) trichlorosilane (Gelest)
- Epoxacast 690 – Parts A and B (Smooth-On)
- Coarse grain sand paper
- Glass microcope slides (Fisher Brand)
- Disposable bulb pipette

Procedure:

Replica Molding with Silanization

1. Cut and remove PDMS microchannels from SU8 patterned silicon wafer (Figure A-1)
2. Dice into separate devices
3. Plasma treat PDMS microchannel mold templates for 30 seconds

4. Place plasma treated templates in a vacuum dessicator with 100µL of silane (Figure A-2)
5. Pull vacuum and leave for 15 minutes
6. Release vacuum and removed devices carefully without touching channel surface especially
7. Place silanized templates in a Petri dish at least 1cm from each side
8. Pour mixed PDMS over these silanized templates (Figure A-3)
9. Pour mixed PDMS on a flat wafer as well
10. Degas uncured PDMS and templates until all bubbles are gone
11. Cure at 65ºC for at least 12 hours

Tubing Assembly Manufacture

12. Cut Tygon tubing or PEEK tubing to 14 inch long sections with a razor blade
13. Roughen 2 inches of length on one end of the PEEK tubing using coarse sandpaper
14. Cut teflon coated wire into 16 inch long sections for each PEEK tubing assembly desired
15. Cut 0.5 inch sections of teflon coated wire for Tygon tubing assembles
16. Insert teflon coated wire into PEEK and Tygon tubing leaving approximately 1mm of teflon coated wire out of tubing (Figure A-4 and A-5)

Mold Preparation

17. After PDMS with templates is cured remove from oven and separate slab from the petri dish (Figure A-6)
18. Separate templates from molds by bending PDMS slab until seams appear

19. If a thin film of PDMS does not allow the separation of molds from templates, cut the film carefully
20. Remove and discard templates (Figure A-6 and Figure A-7)
21. Dice the slab into separate molds
22. Inspect molds for imperfections and discard any with non-uniform looking channel surface
23. Punch holes at inlets and outlets in the molds (Figure A-8)
24. Cut out and set aside PDMS slab from the flat wafer

Epoxy Device Production

25. Mix epoxy and degas molds, flat PDMS slabs and mixed epoxy for 30 minutes
26. Prepare molds by inserting tubing assemblies at inlets and outlets leaving <1mm of teflon wire showing between donut port and PEEK or tygon tubing (Figure A-10 and Figure A-11)
27. If tubing assemblies do not stay in place secure them with tape to taller nearby objects
28. Using bulb pipette, fill molds with epoxy until epoxy is level with the top of the mold (Figure A-12)

Epoxy Coated Slides Production

29. Lay flat PDMS slabs wafer side up on a surface
30. With a bulb pipette, draw Ts of epoxy approximately the size of the glass slides being coated (Figure A-13 and Figure A-14)
31. Slowly lower glass slides onto epoxy Ts starting from the wide end of the T shapes (Figure A-15 and Figure A-16)
32. Allow devices and coated slides to cure for another 27.5 hours.

Epoxy Device Assembly

33. At 28 hours after mixing the components of epoxy, remove glass slides from the PDMS slab (Figure A-17)
34. Place epoxy coated sides epoxy up on a 55ºC hot plate (Figure A-18)
35. Place epoxy devices and molds in a freezer for 3 minutes (This step can be skipped but reduces deformation of inlets and outlets)
36. After 3 minutes remove devices from freezer and pull out teflon coated wire from the end of PEEK tubing away from the devices (Figure A-19)
37. Remove epoxy devices from molds (Figure A-20)
38. Pull out short teflon wire sections if tygon tubing was used (Figure A-21)
39. Gently press epoxy devices against epoxy coated slides on the hotplate (Figure A-22)
40. Leave assembled devices on hotplate for 5 minutes (Figure A-23)
41. Inspect devices for complete bonding adding gentle pressure where necessary (Figure A-24)
42. Allow devices to completely harden for another 24 hours before use

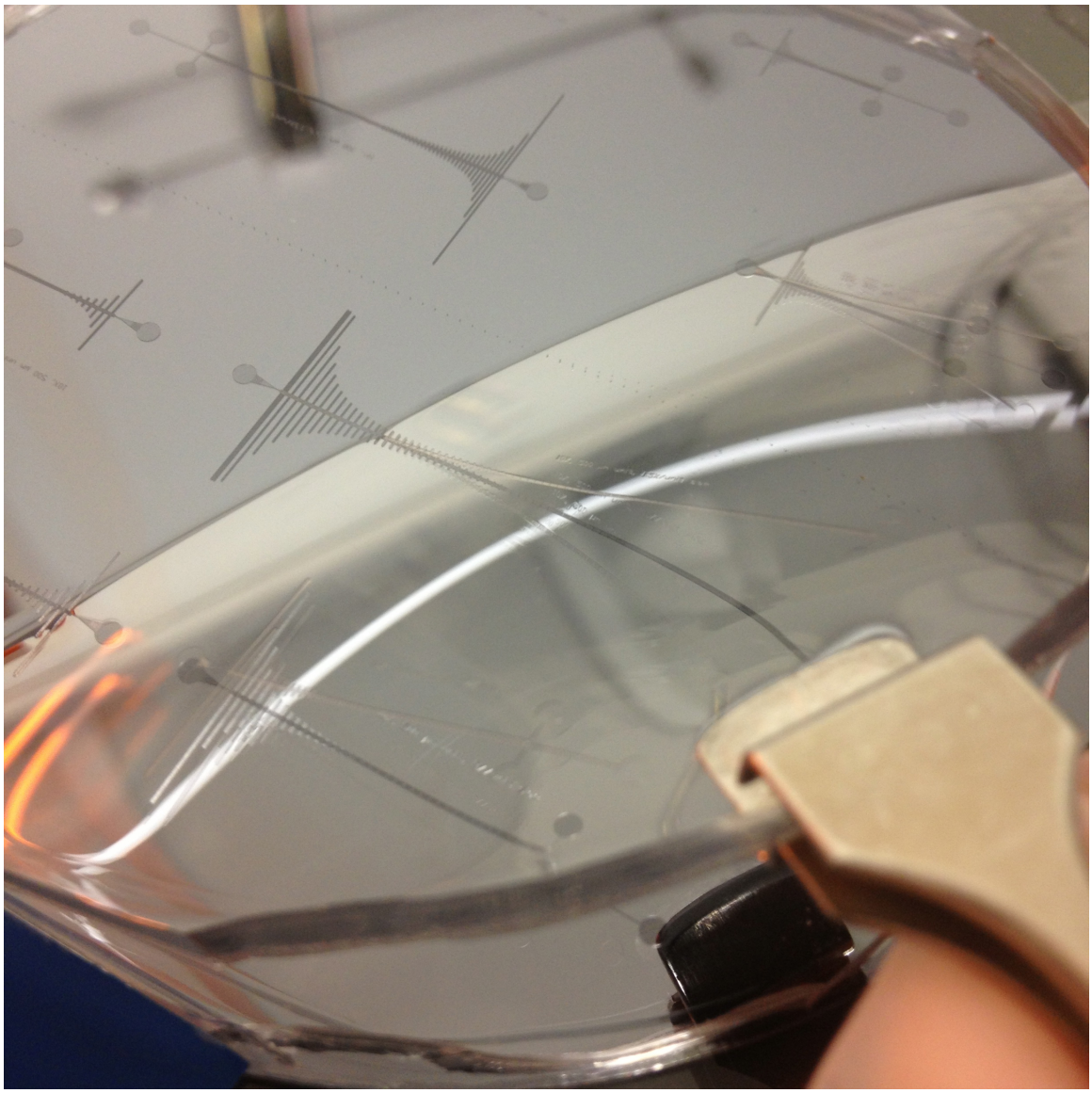

Figure A-1: SU8 patterned silicon wafer with PDMS channels being removed.

Figure A-2: Oxygen plasma treated PDMS channels in vacuum dessicator with small amount of silane in aluminum foil dish on level below. PDMS channels are facing up.

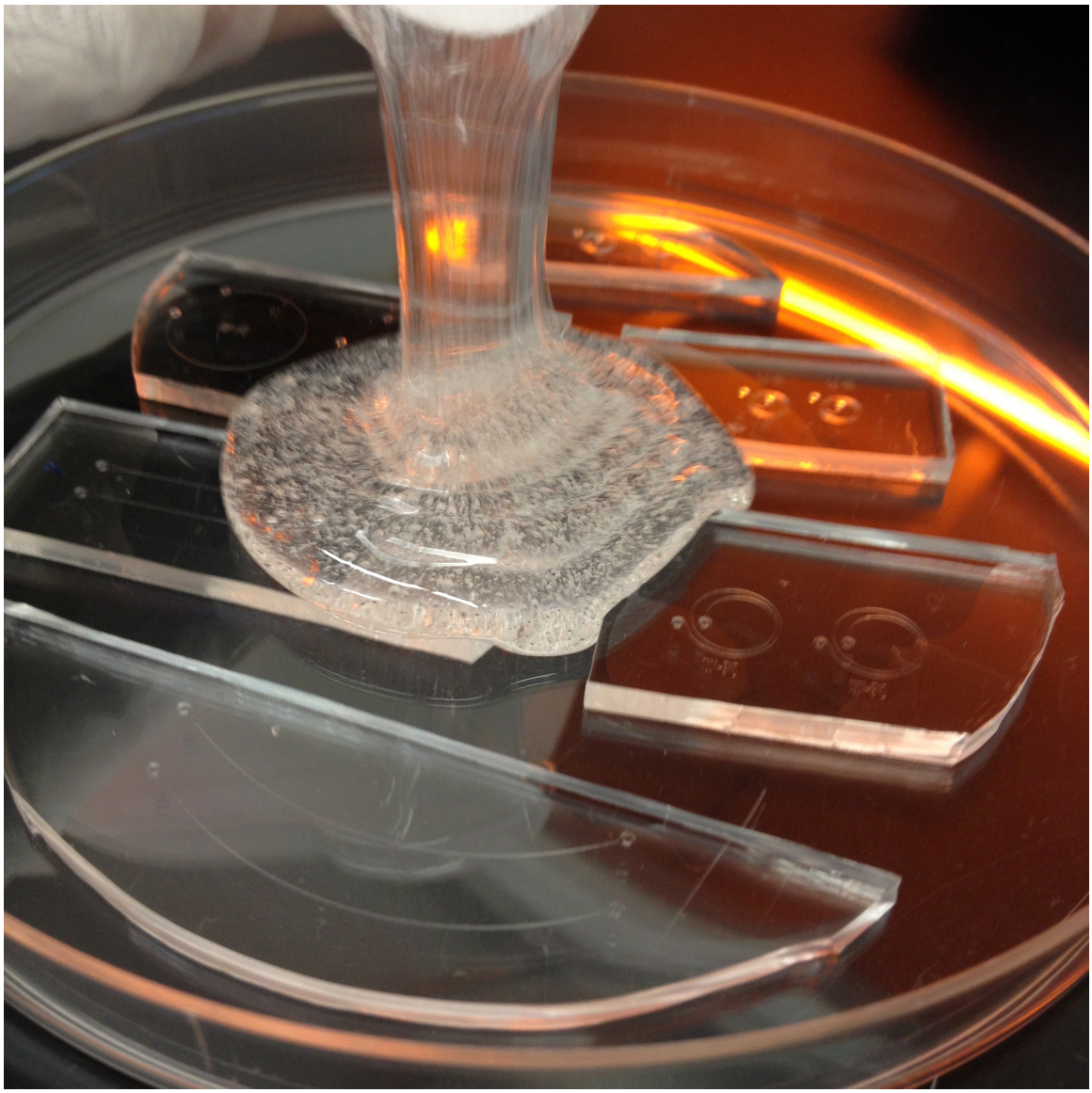

Figure A-3: Silanized PDMS channels in a petri dish, channels up being covered with uncured PDMS for mold generation.

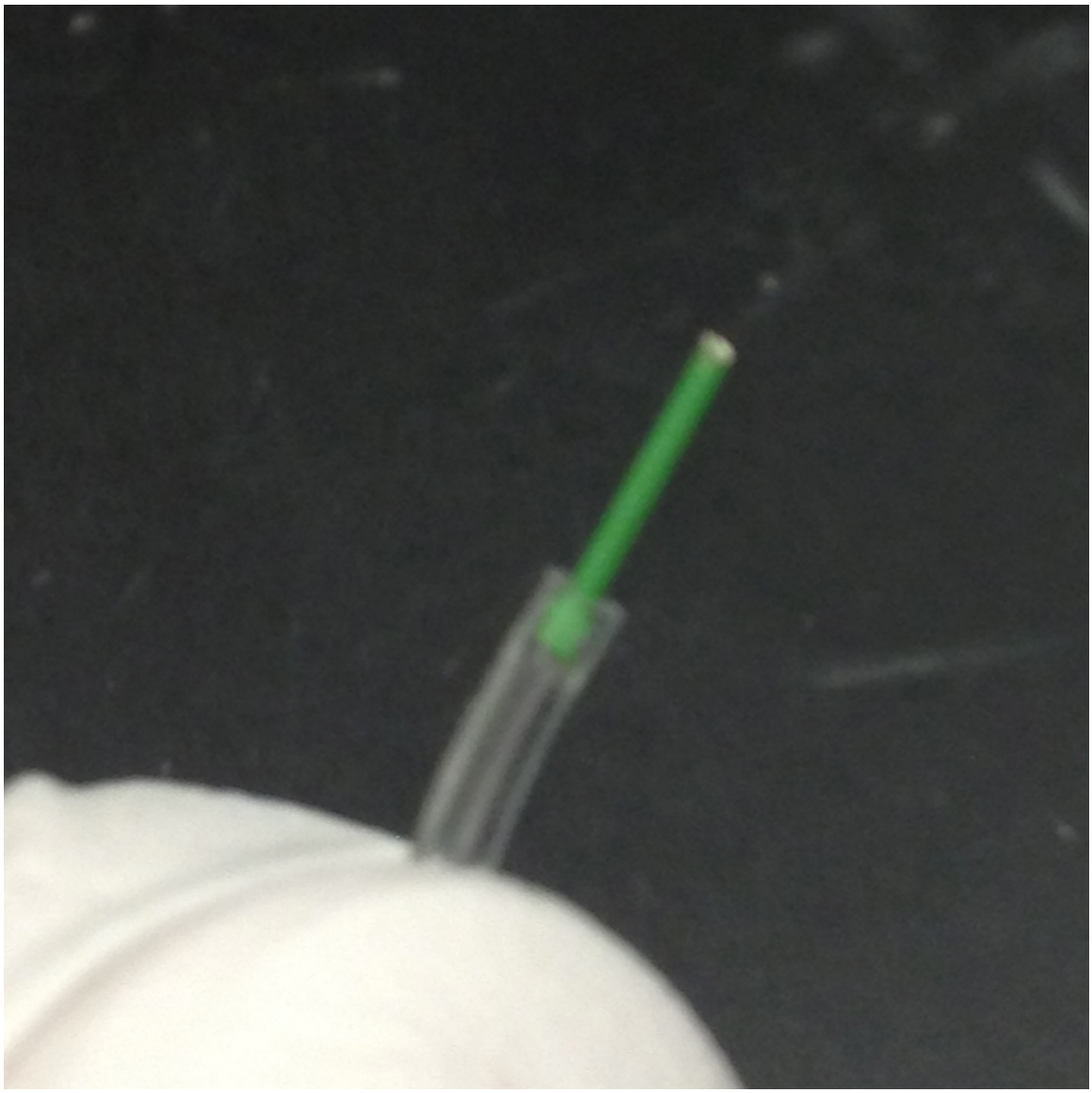

Figure A-4: Tygon tubing (translucent) with teflon coated wire (green) used as an outlet tubing assembly.

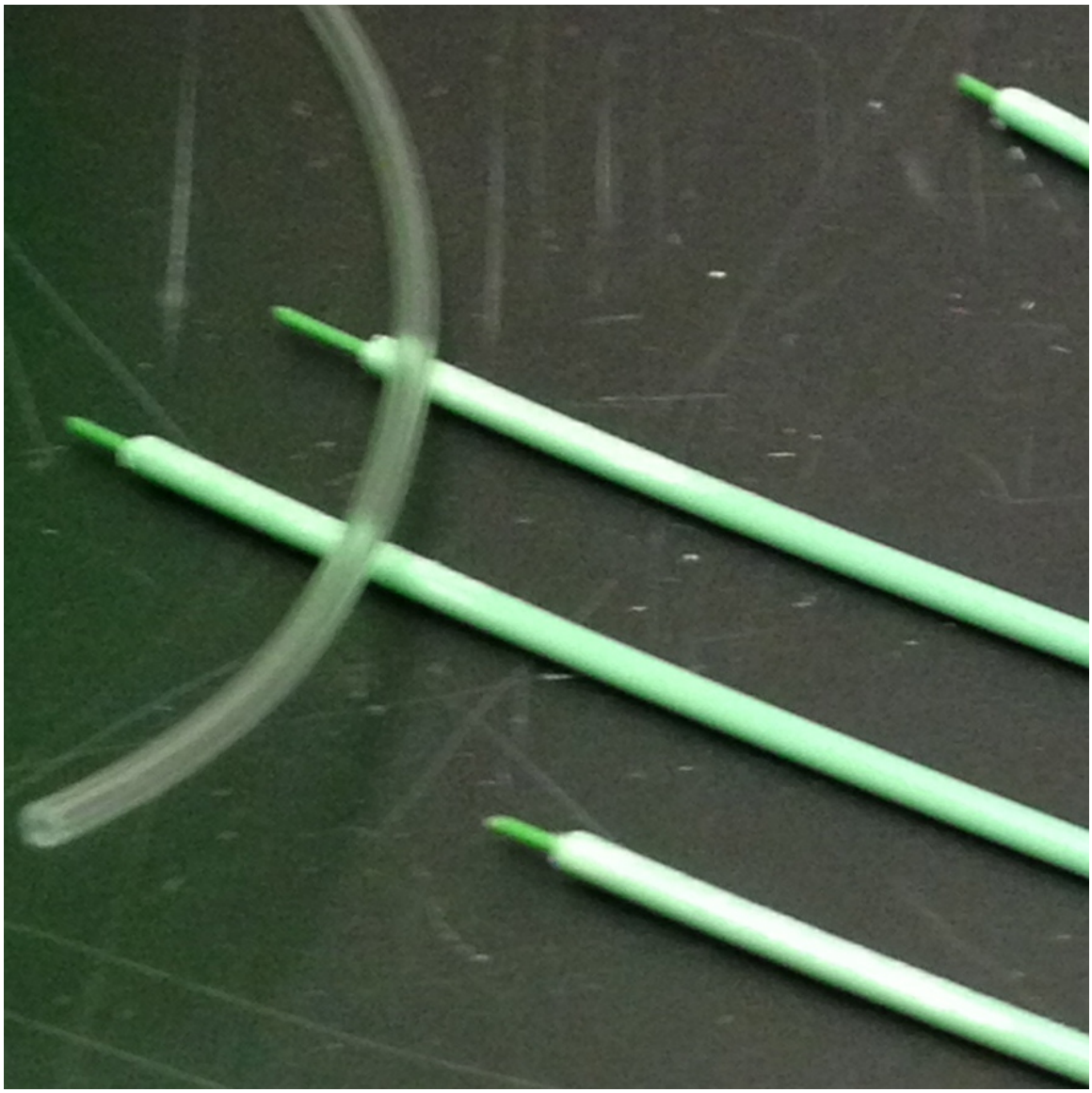

Figure A-5: PEEK tubing (light green) and teflon coated wire (dark green) for inlet tubing assemblies.

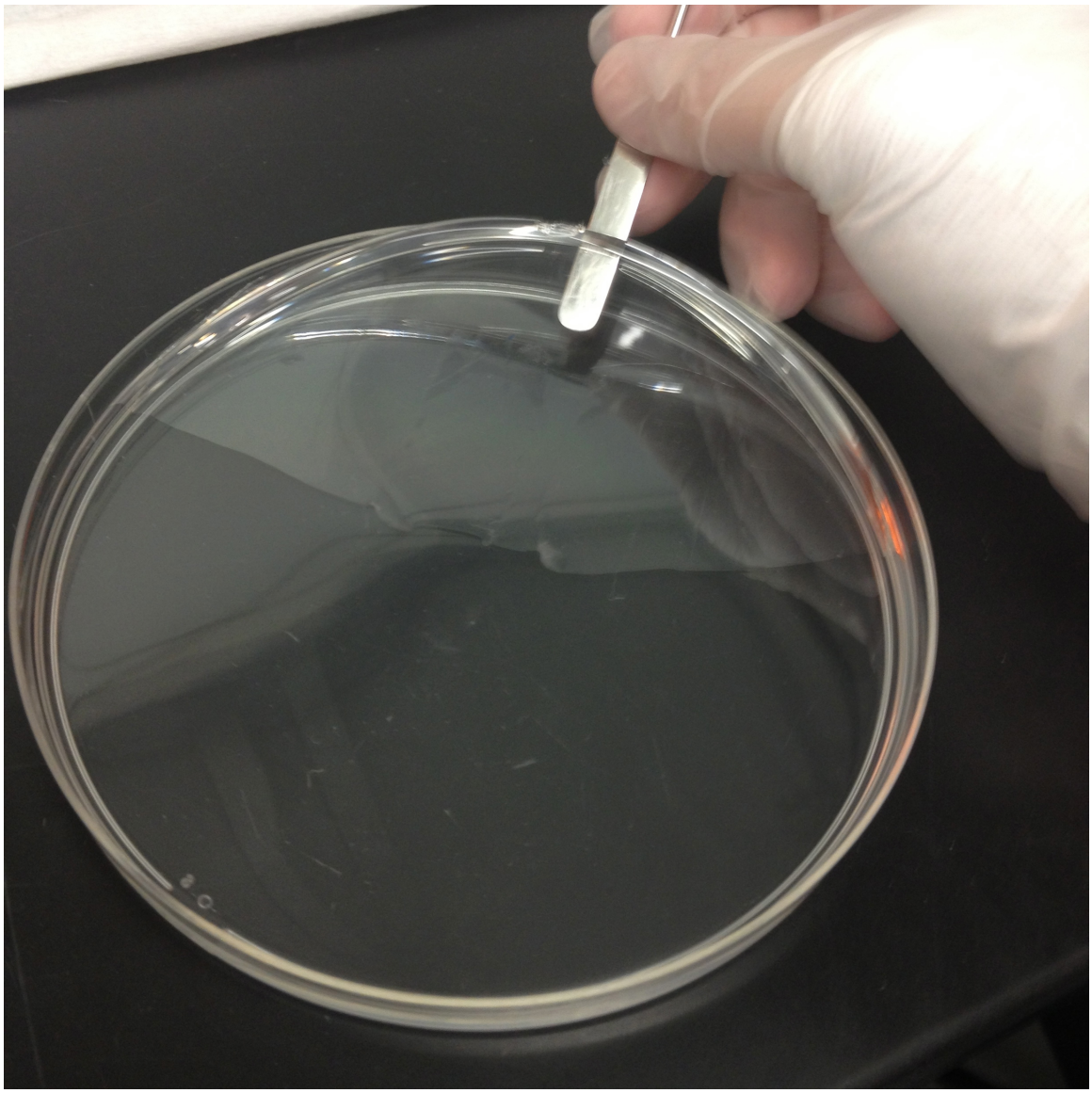

Figure A-6: Cured PDMS molds prior to removal of silanized templates.

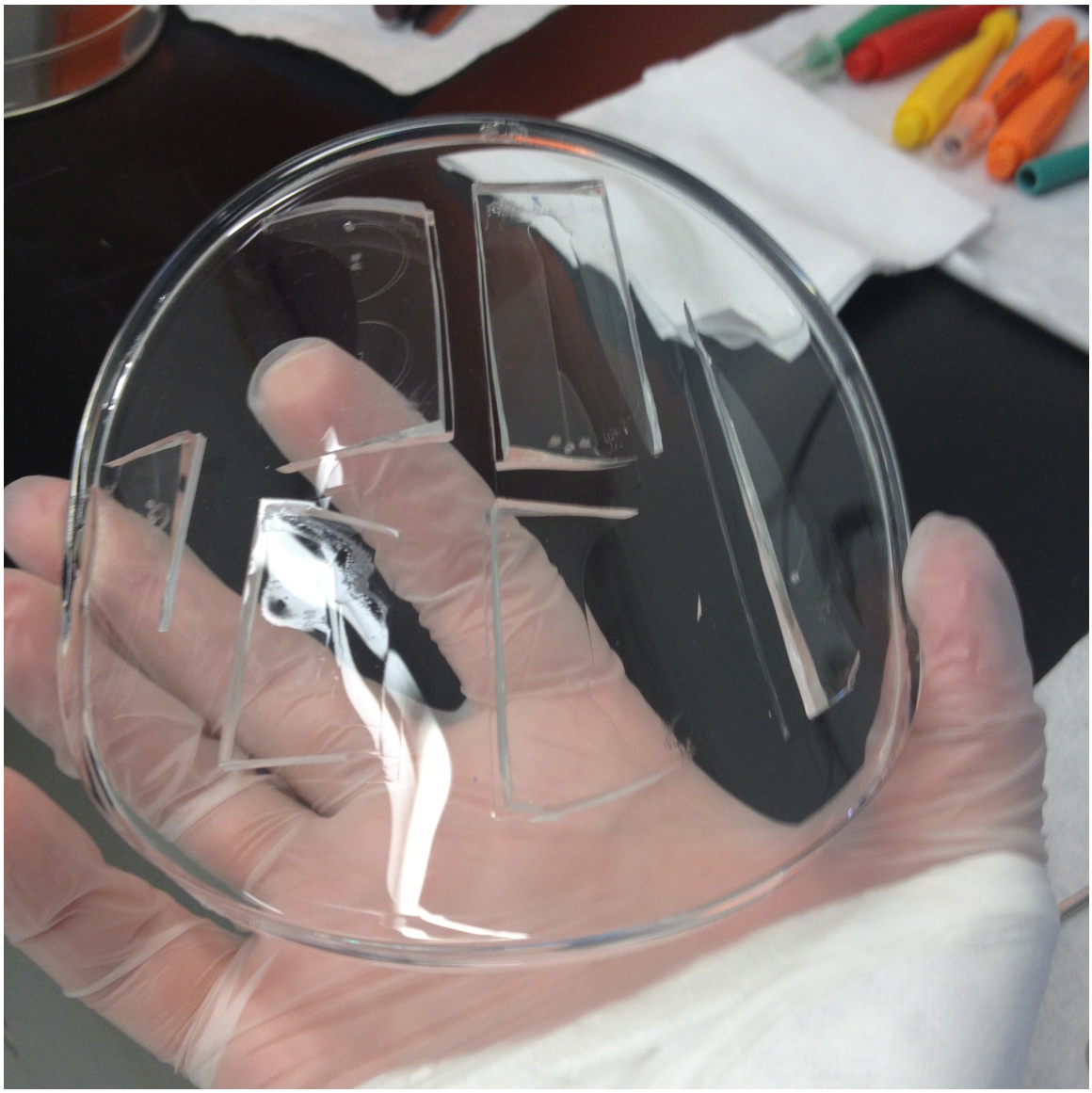

Figure A-7: Partial separation of silanized templates. Sometimes thin films of PDMS must be punctured to start seam splitting. Edges of devices should be vague but present in the correct angle of light.

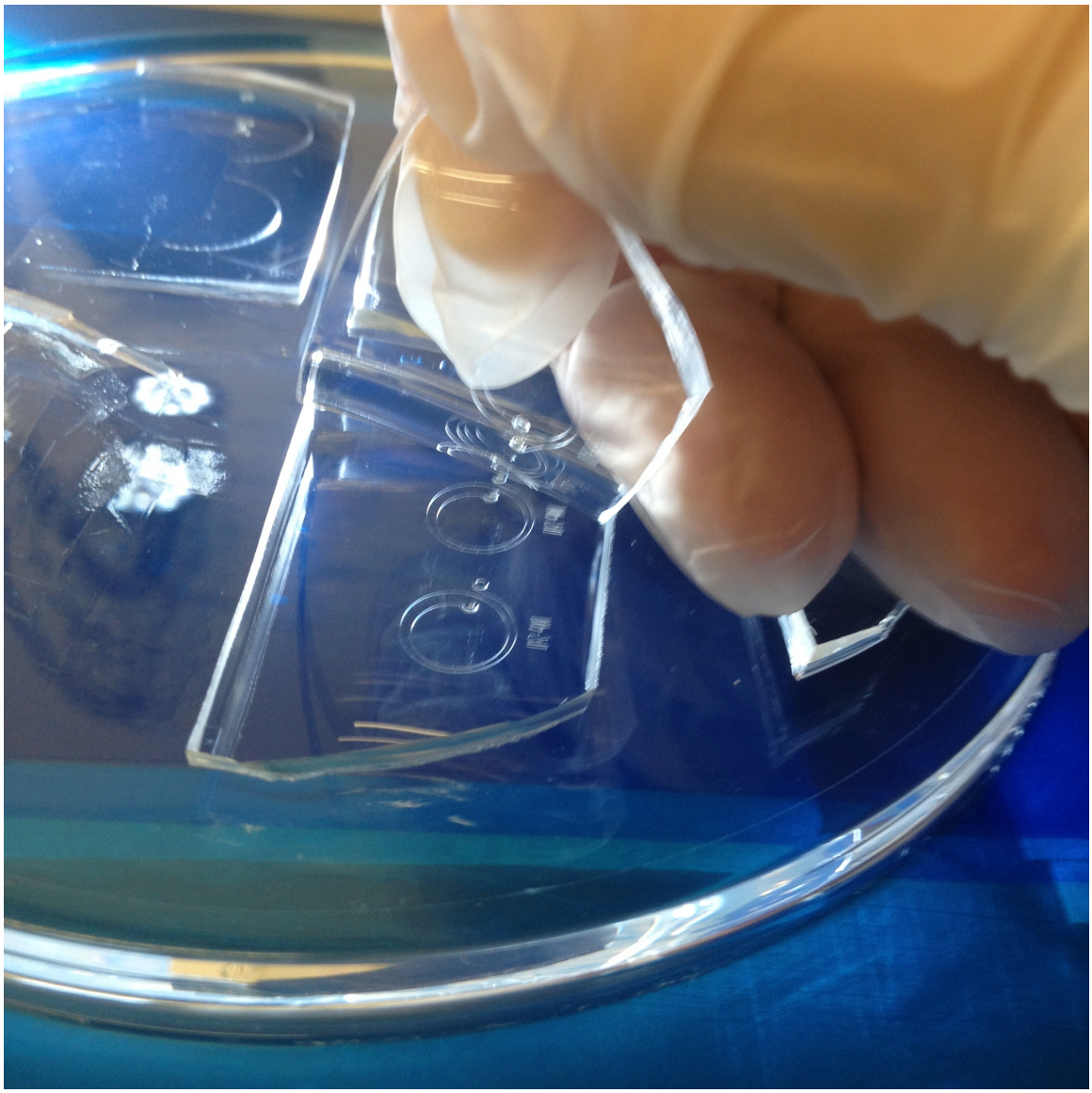

Figure A-8: Removal of silanized PDMS templates leaving a positive, raised mold version of the same channels.

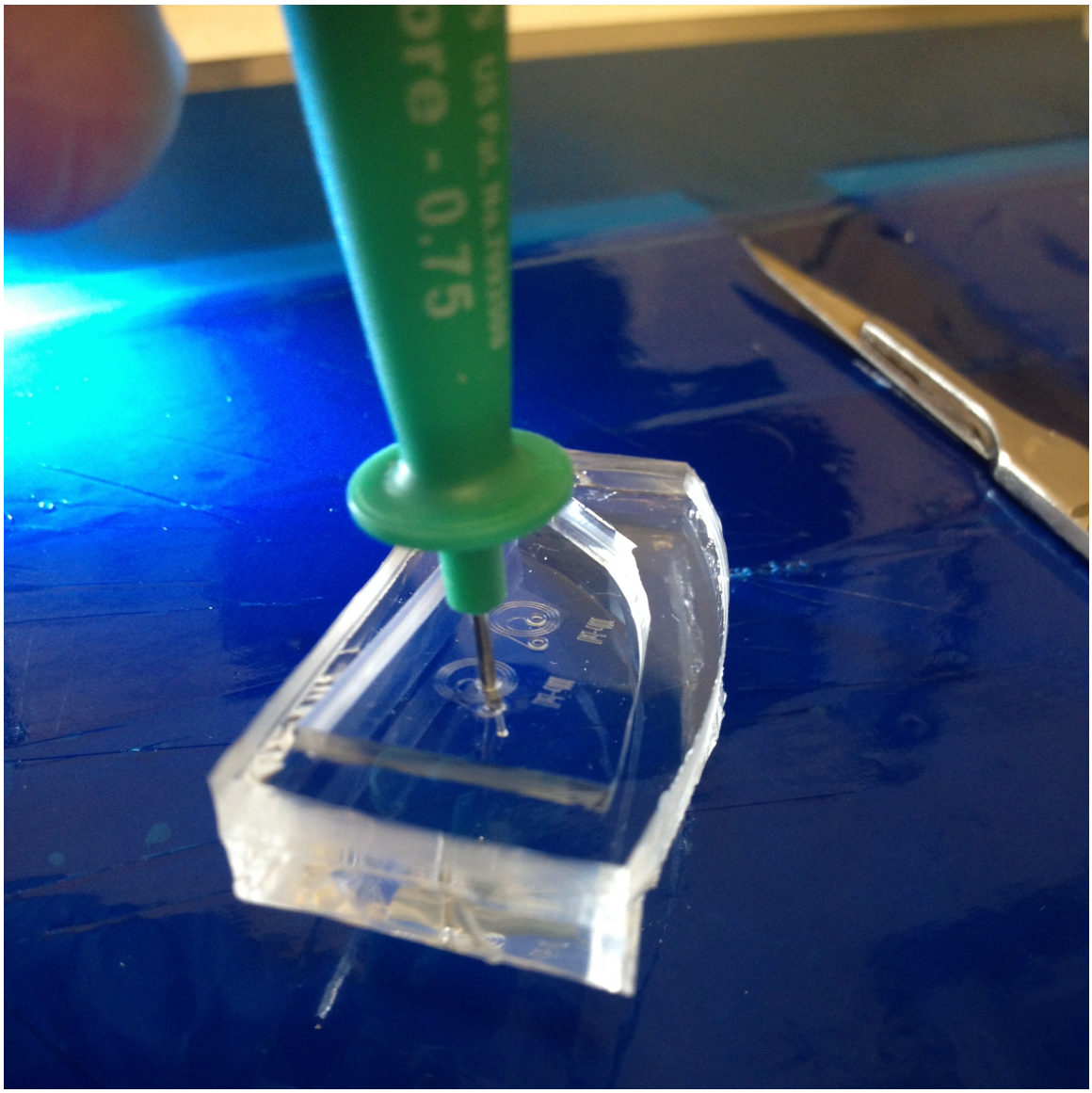

Figure A-9: Punched holes are created within donut ports at both the inlet and outlet for each device.

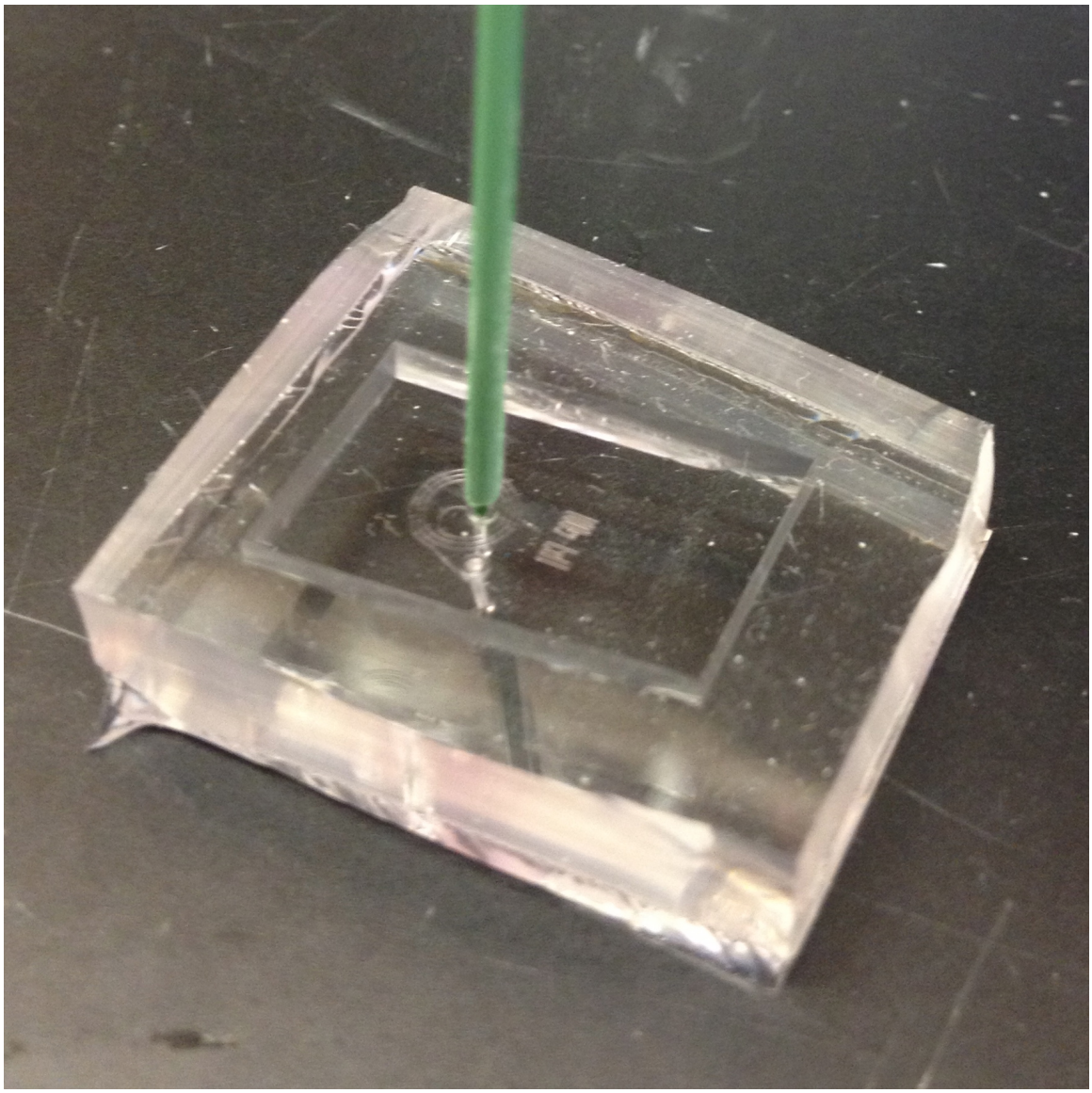

Figure A-10: Inlet tubing assembly is inserted and about a 1mm gap between the PEEK tubing and donut port is left.

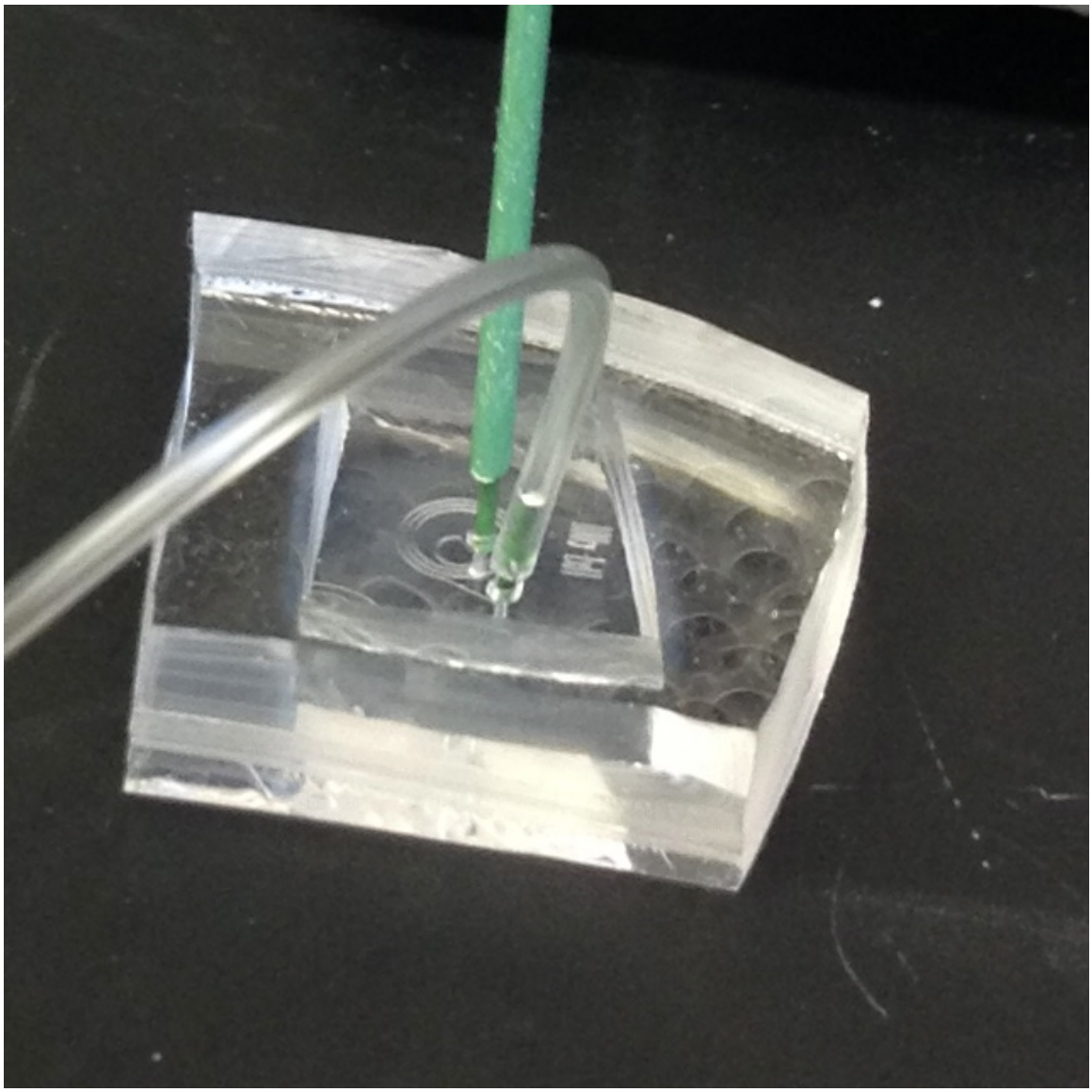

Figure A-11: Inlet and outlet tubing assemblies inserted.

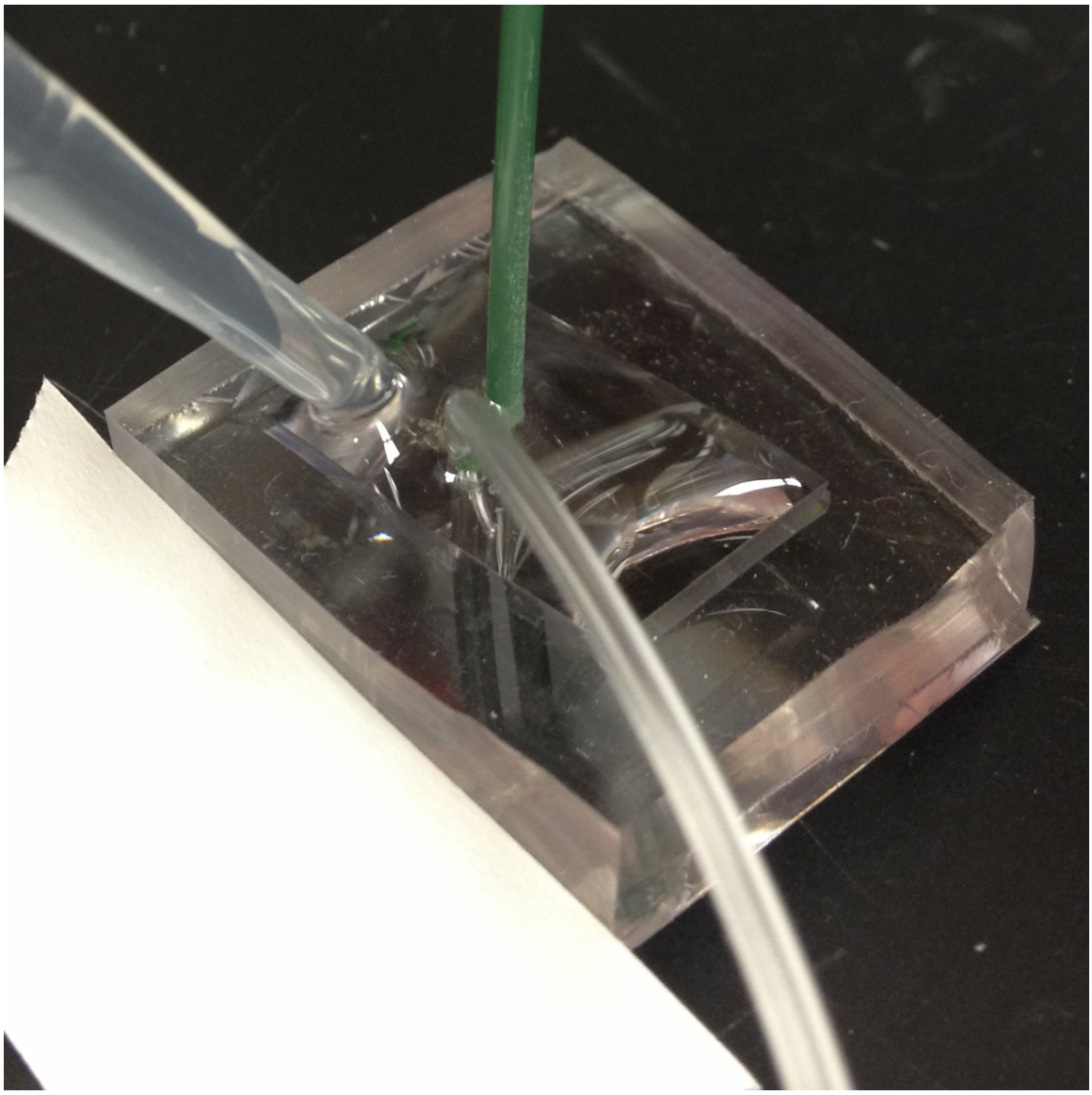

Figure A-12: Bulb pipette injecting degassed epoxy slowly into a mold with tube assemblies.

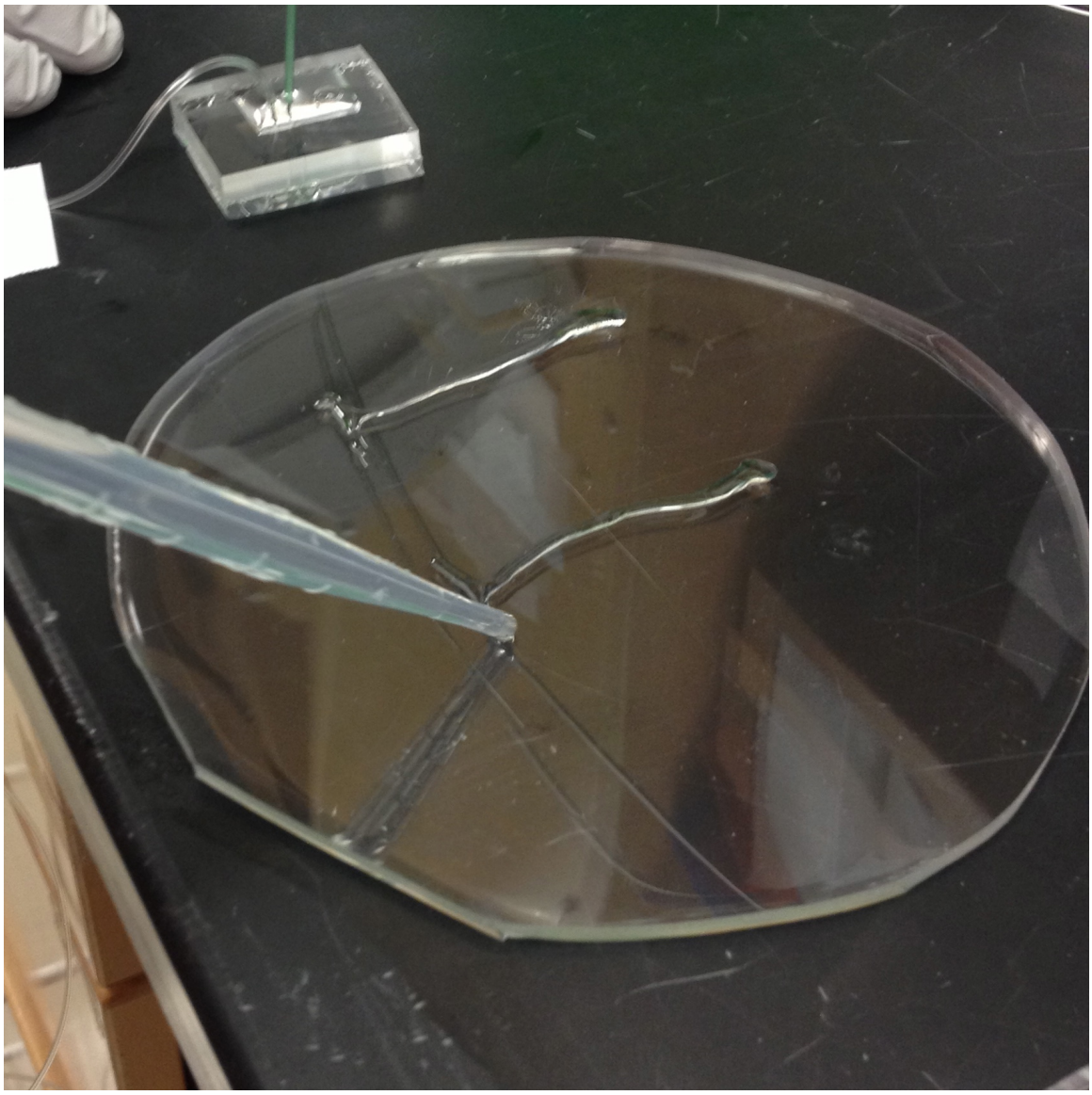

Figure A-13: Bulb pipette used to draw epoxy Ts for coated slide fabrication. Note: Epoxy cannot be spun on as it will not cure fast enough before dewetting.

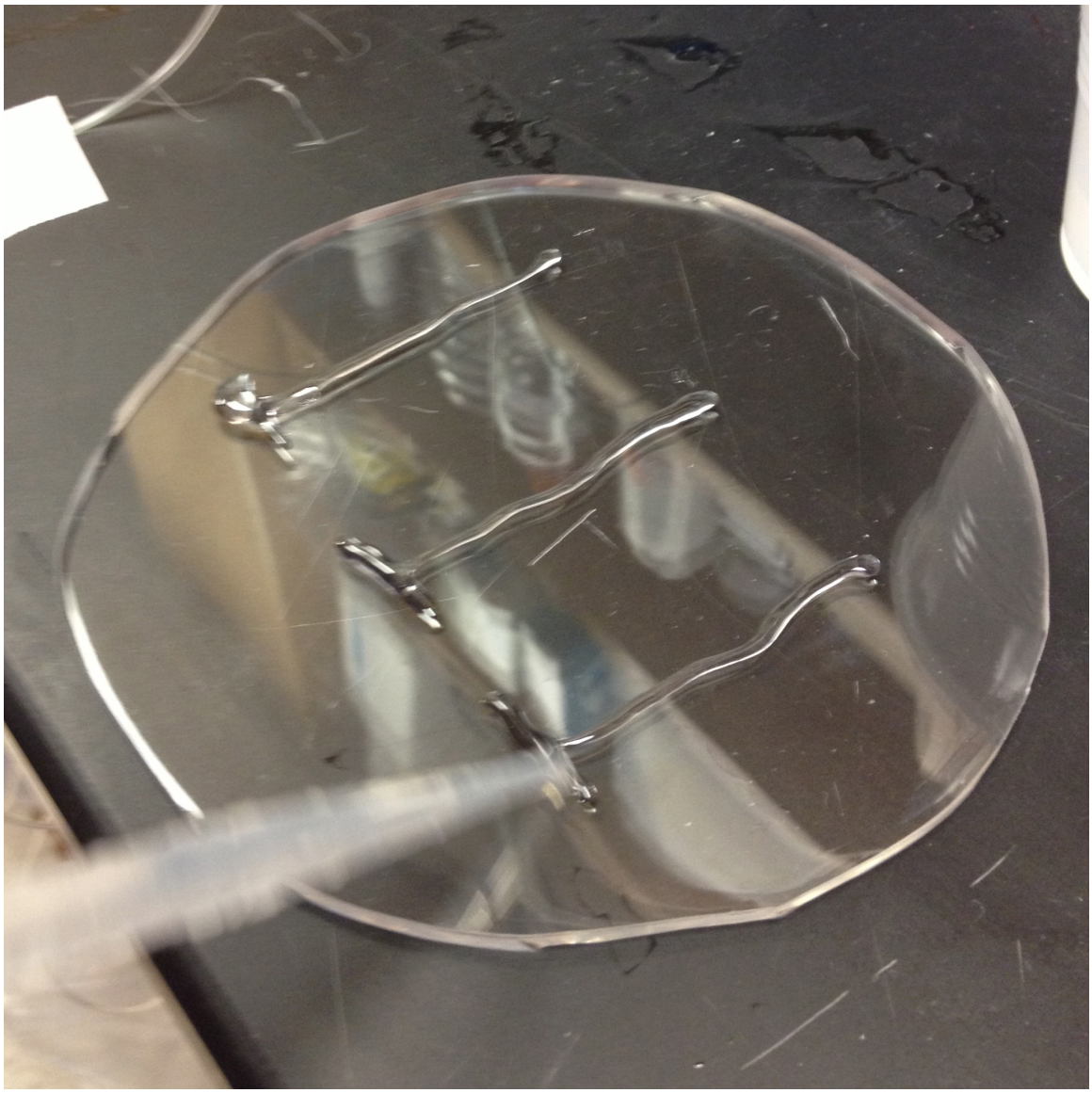

Figure A-14: Three Ts drawn on a degassed PDMS slab.

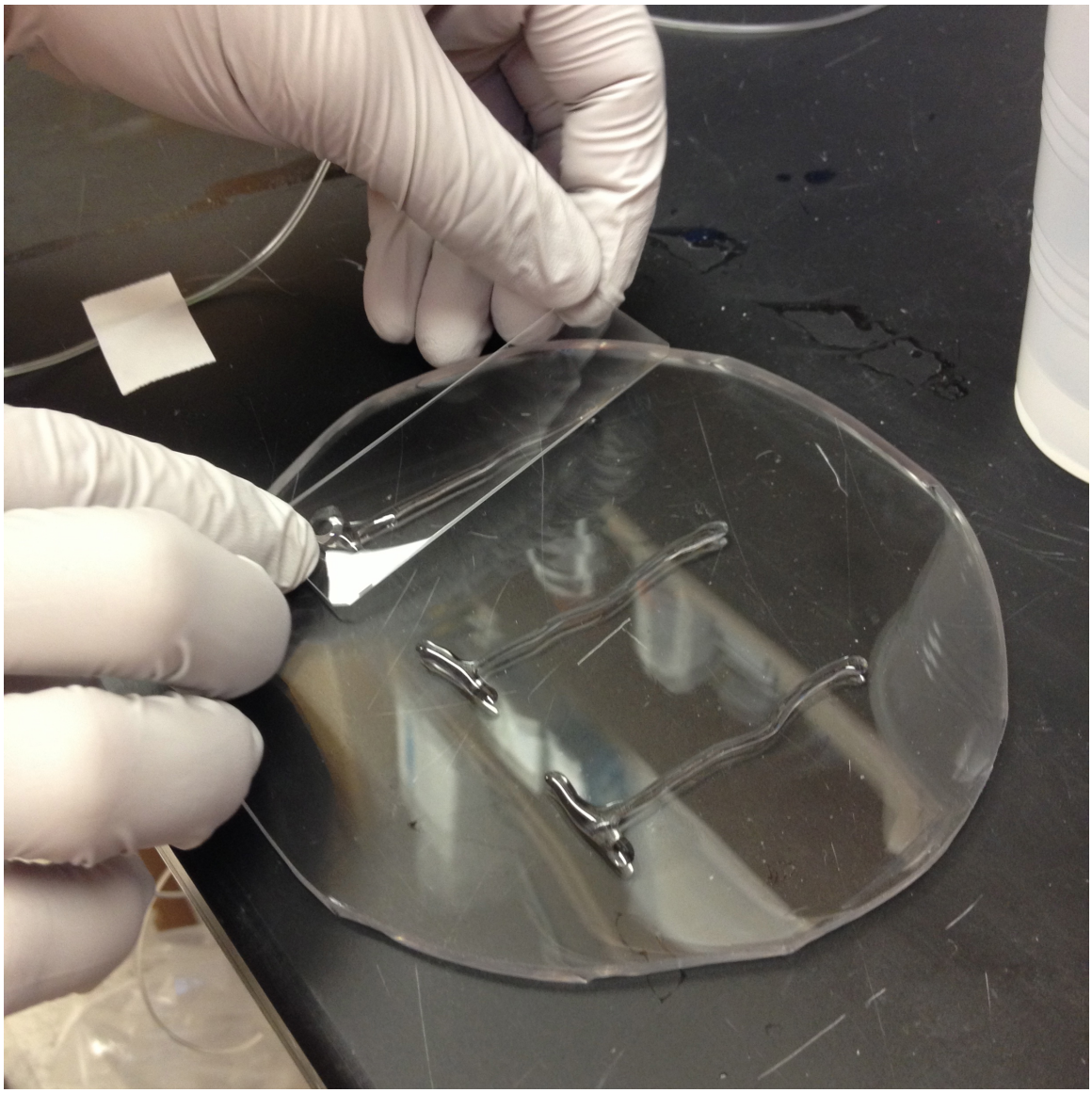

Figure A-15: Laying down of a glass slide onto one of the epoxy Ts.

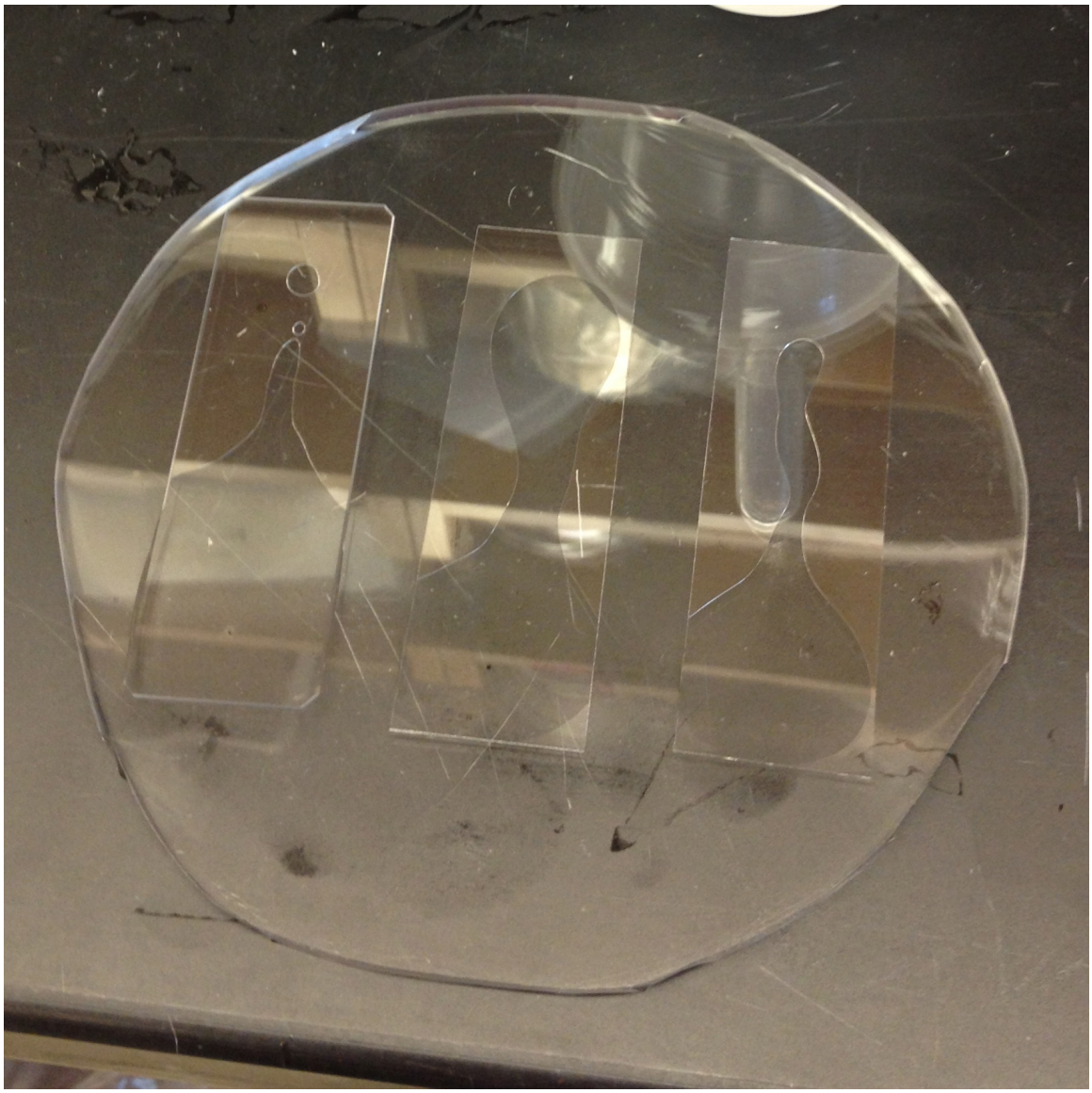

Figure A-16: Glass on epoxy Ts. The epoxy will spread over time.

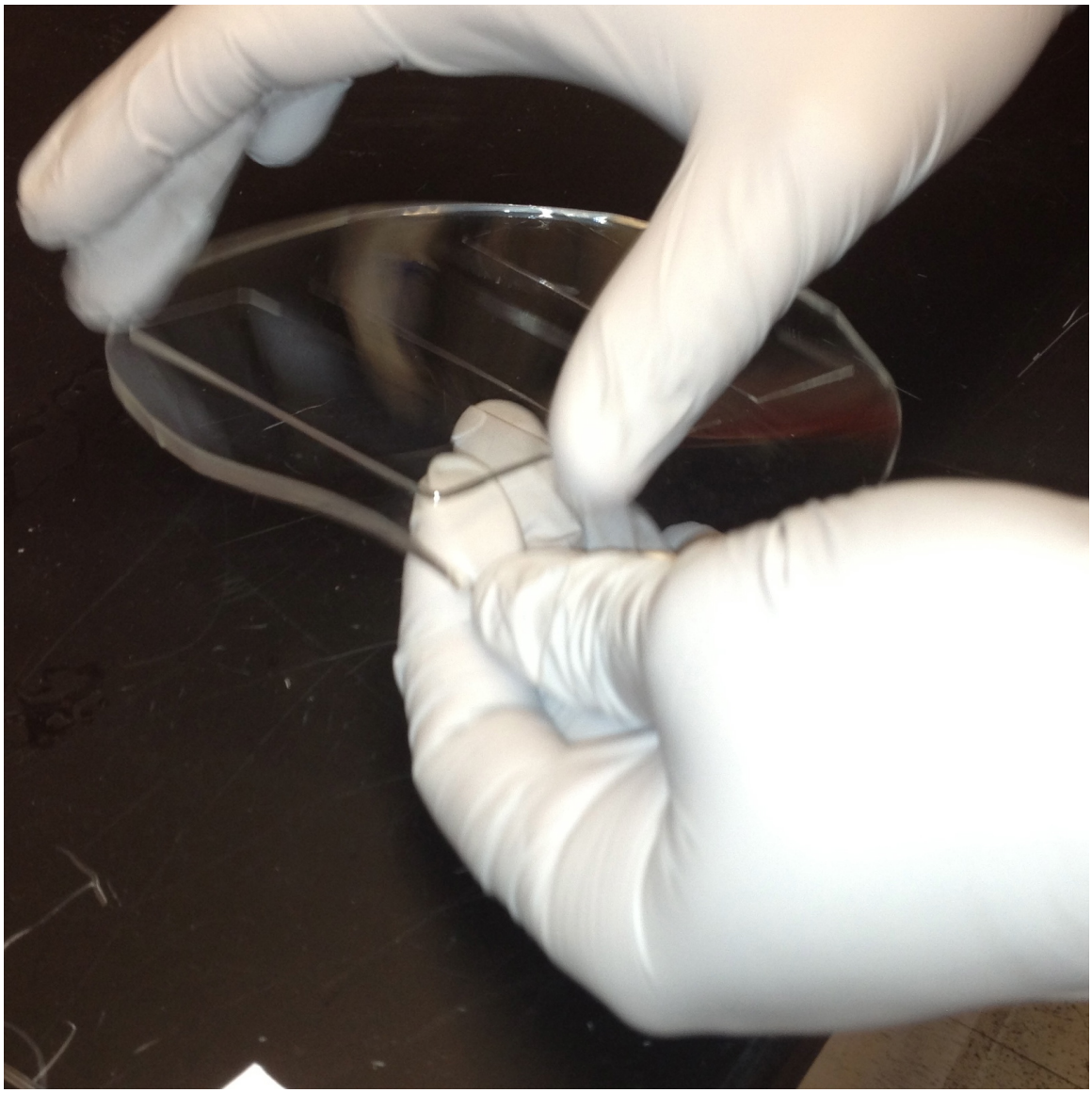

Figure A-17: After 28 hours since mixing the components of epoxy. The coated slides are separated from the PDMS slabs.

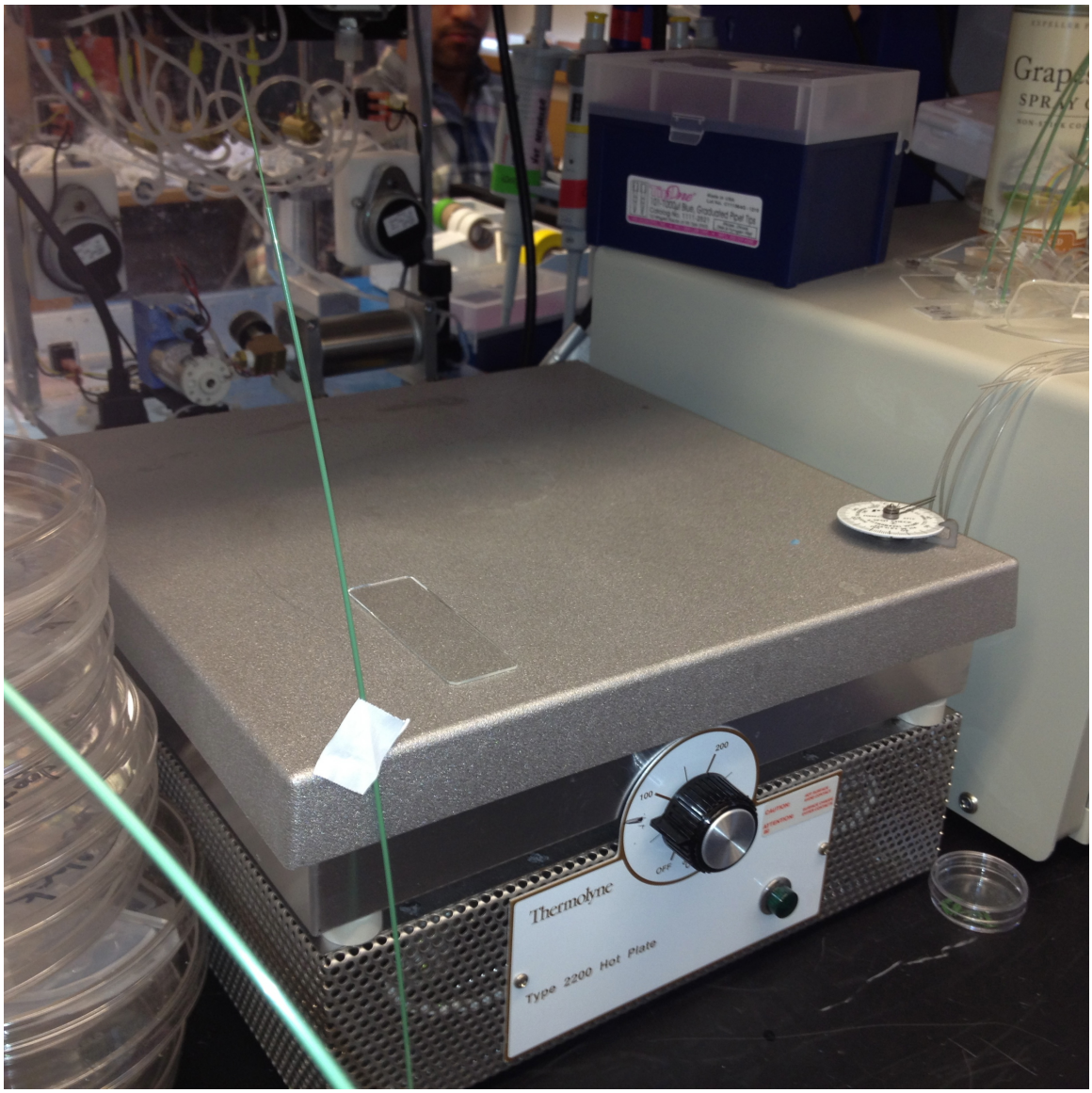

Figure A-18: The partially cured and coated slides are placed epoxy up on a hot plate at 55ºC.

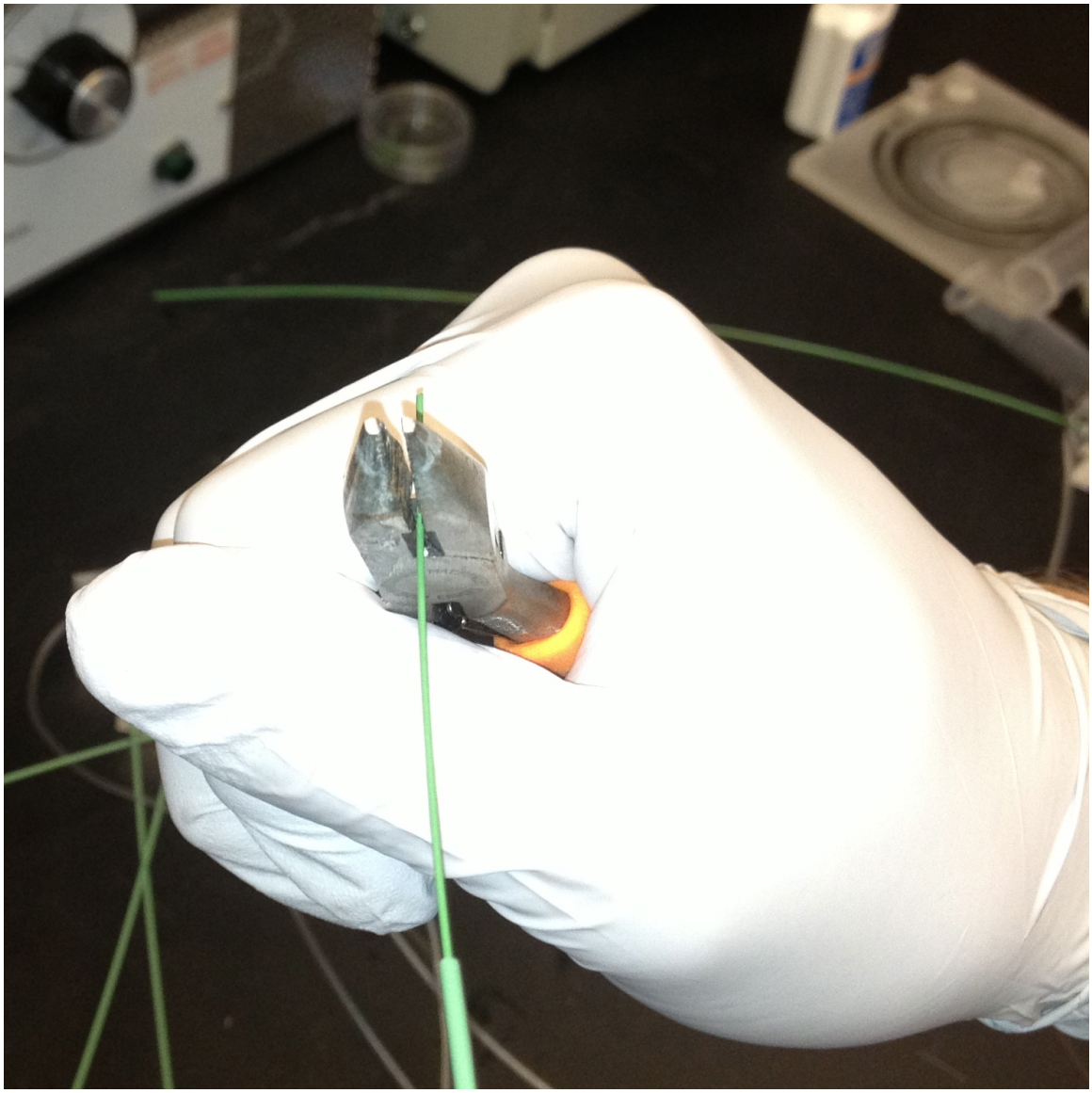

Figure A-19: After cooling partially cured devices. Teflon coated wire is removed from the end of the tubing assembly away from the device.

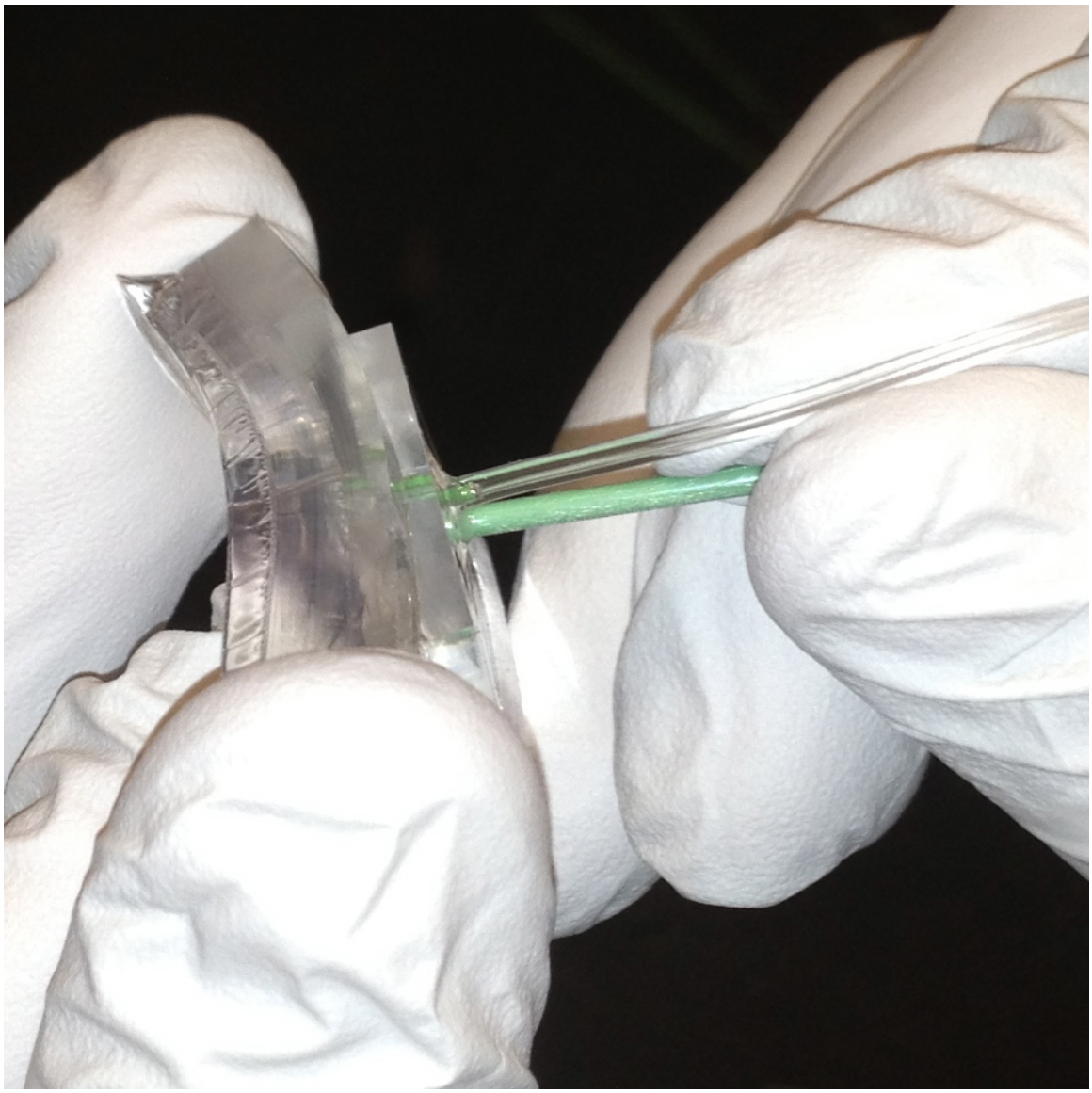

Figure A-20: Epoxy device being separated from the mold.

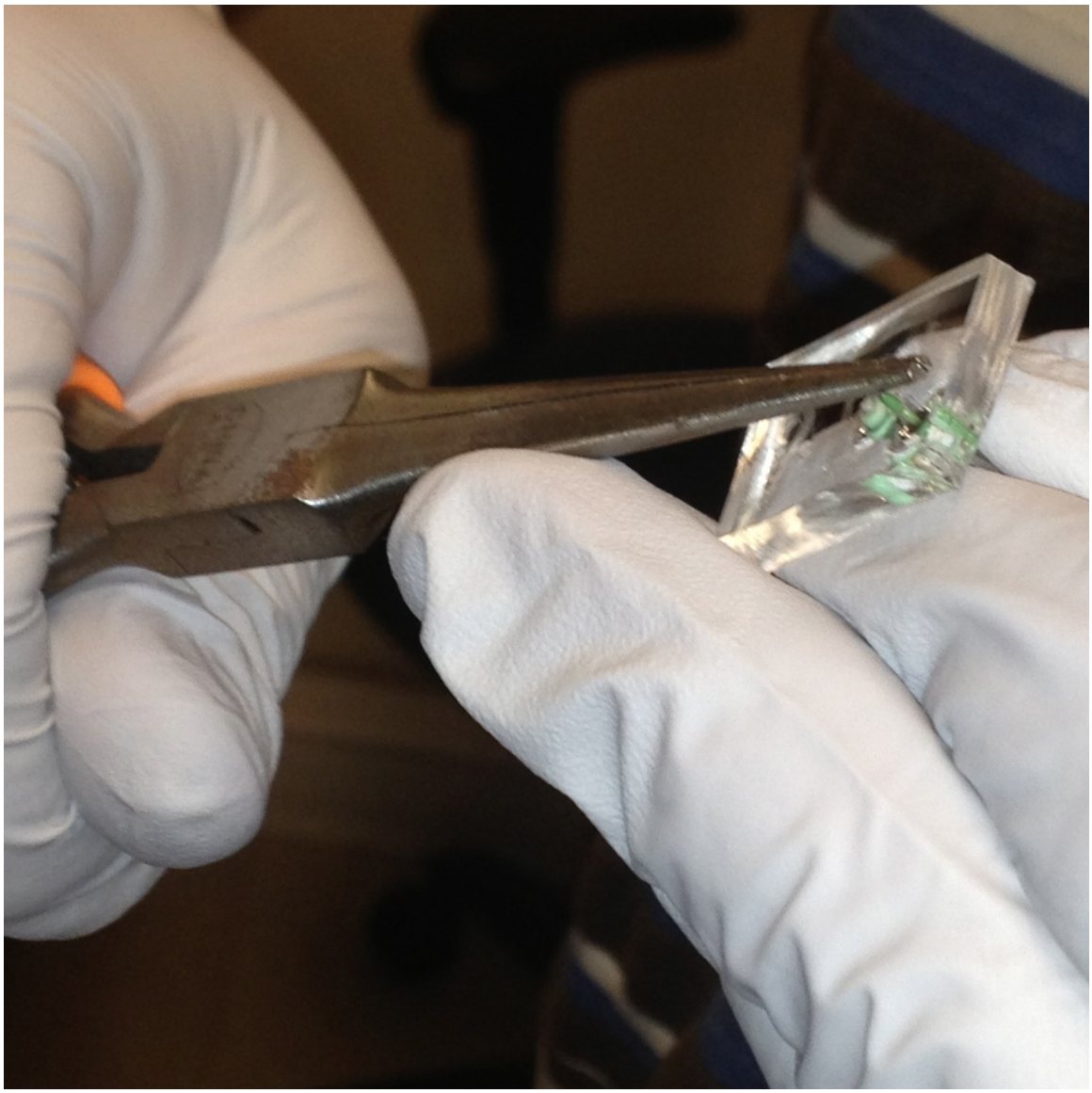

Figure A-21: Teflon wire being removed from the outlet where Tygon tubing was used.

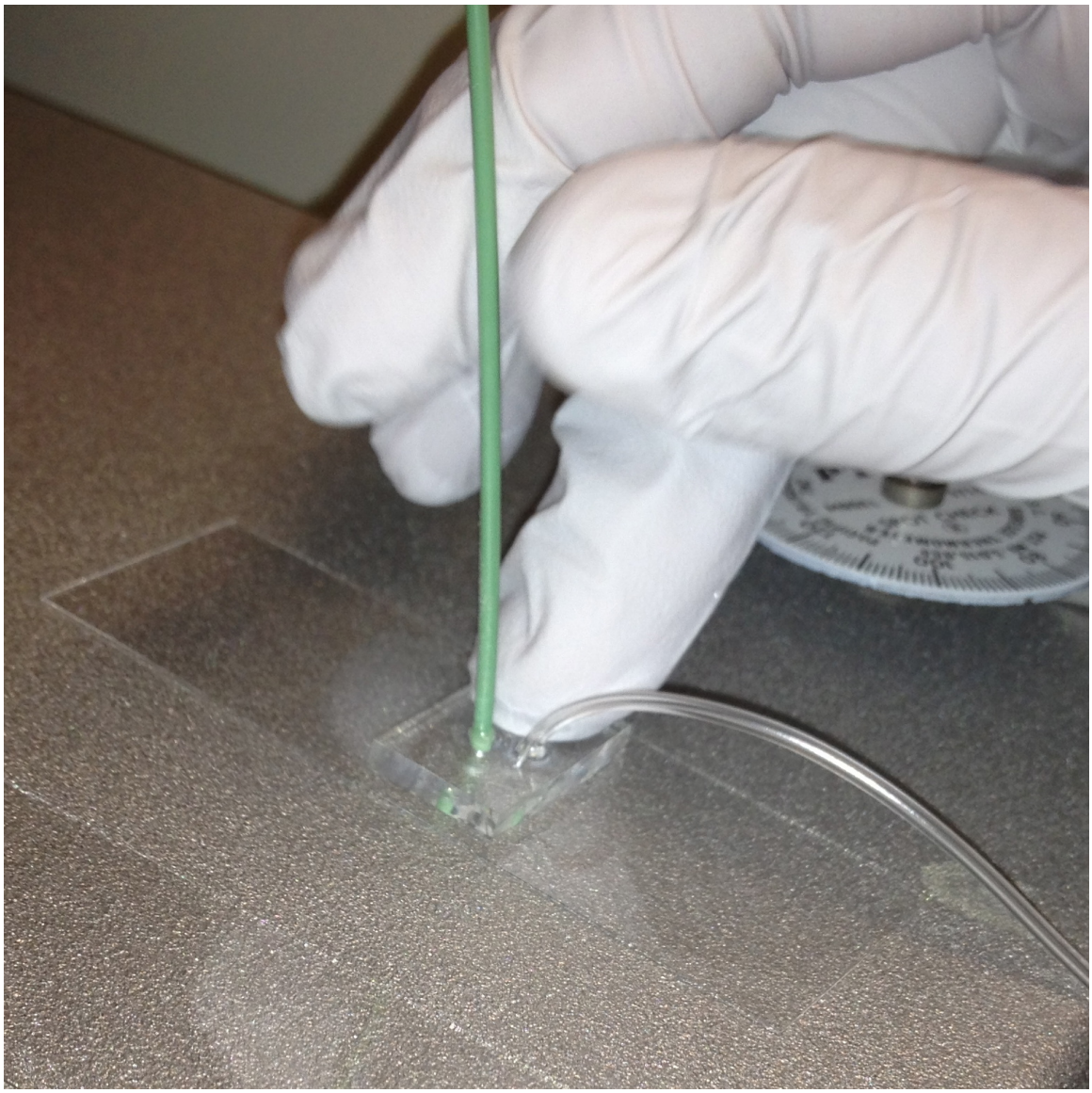

Figure A-22: Epoxy device is pressed gently against the warm epoxy coated glass.

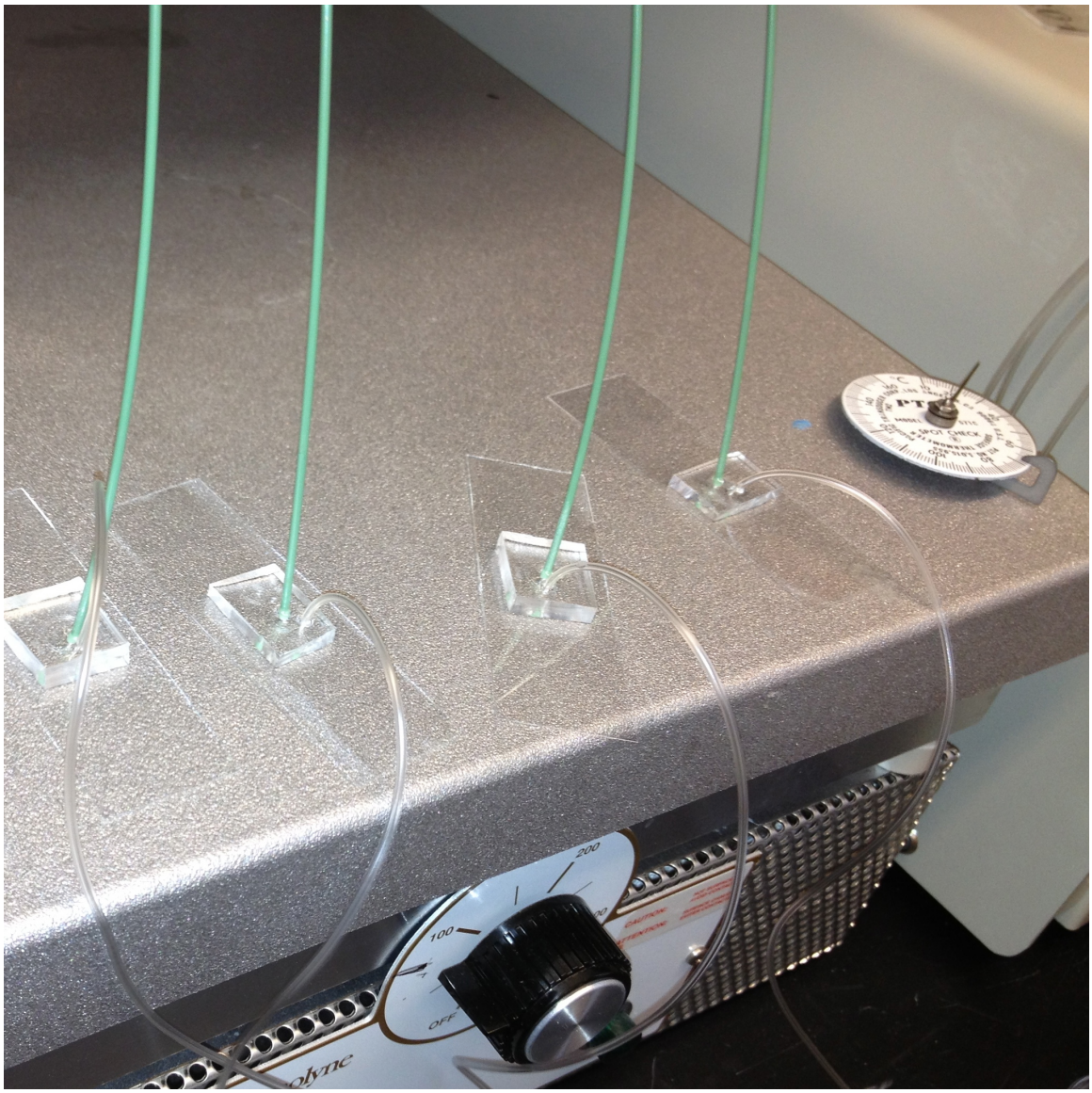

Figure A-23: Device is left on hotplate for 5 minutes.

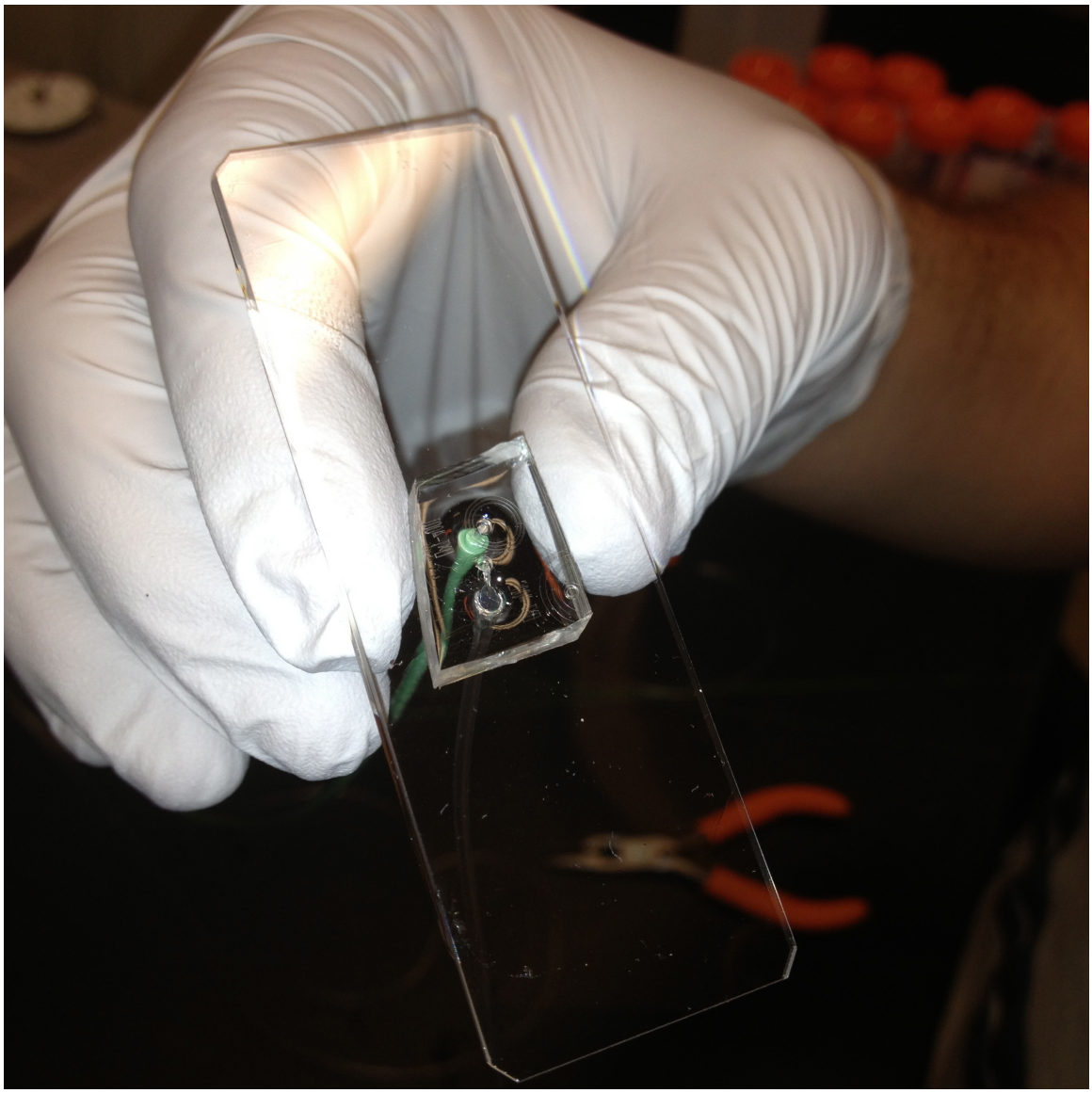

Figure A-24: Device is inspected and pressure applied if needed to ensure bonding. These are then allowed to cure for another 24 hours before use.

Appendix B

Straightened Images – Complete Set

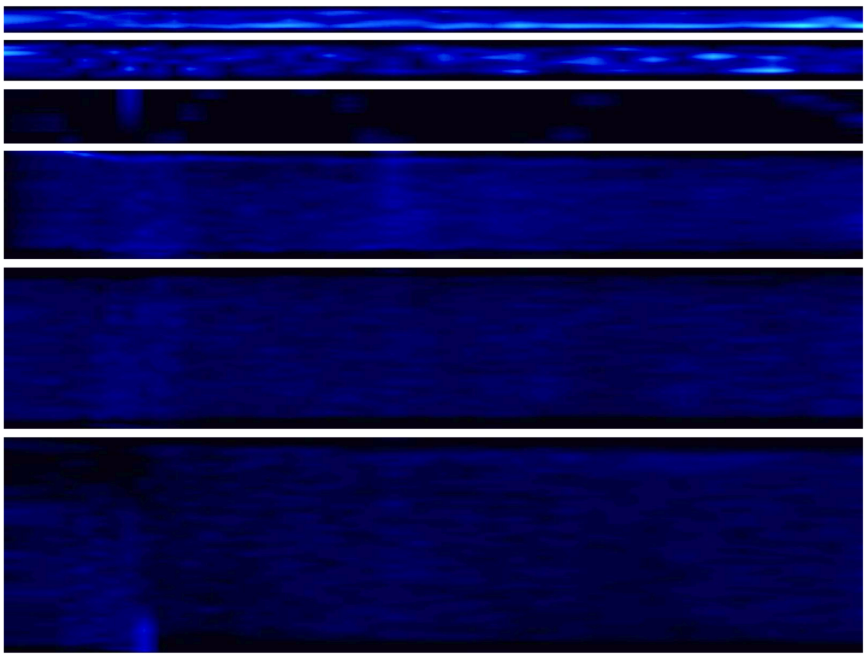

Figure B-1: Straightened images for U_{Avg}=0.067m/s. Dark blue is low intensity and red/white is high intensity seen when a focused streak is formed. All images are for decreasing Dean number devices.

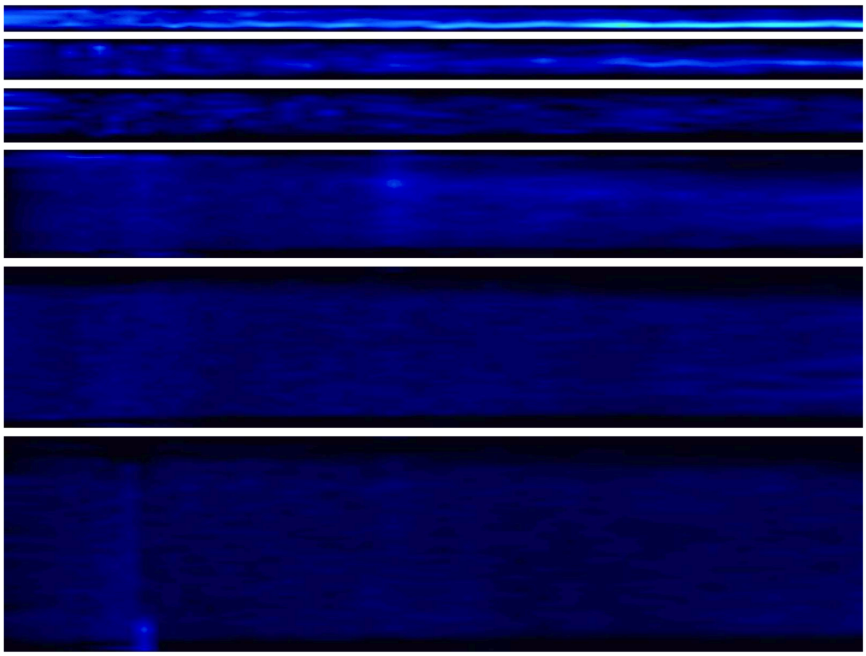

Figure B-2: Straightened images for U_{Avg}=0.133m/s. Dark blue is low intensity and red/white is high intensity seen when a focused streak is formed. All images are for decreasing Dean number devices.

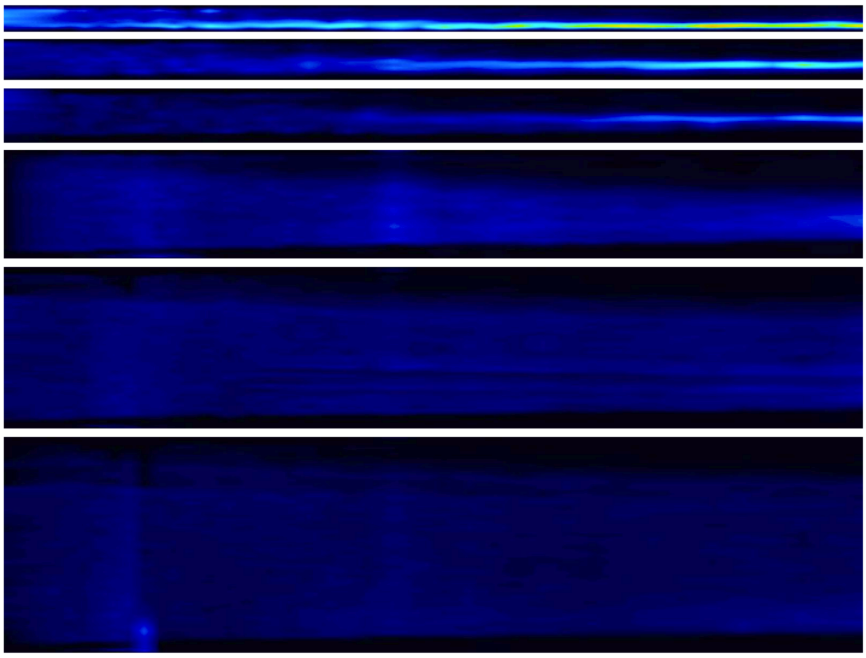

Figure B-3: Straightened images for U_{Avg}=0.267m/s. Dark blue is low intensity and red/white is high intensity seen when a focused streak is formed. All images are for decreasing Dean number devices.

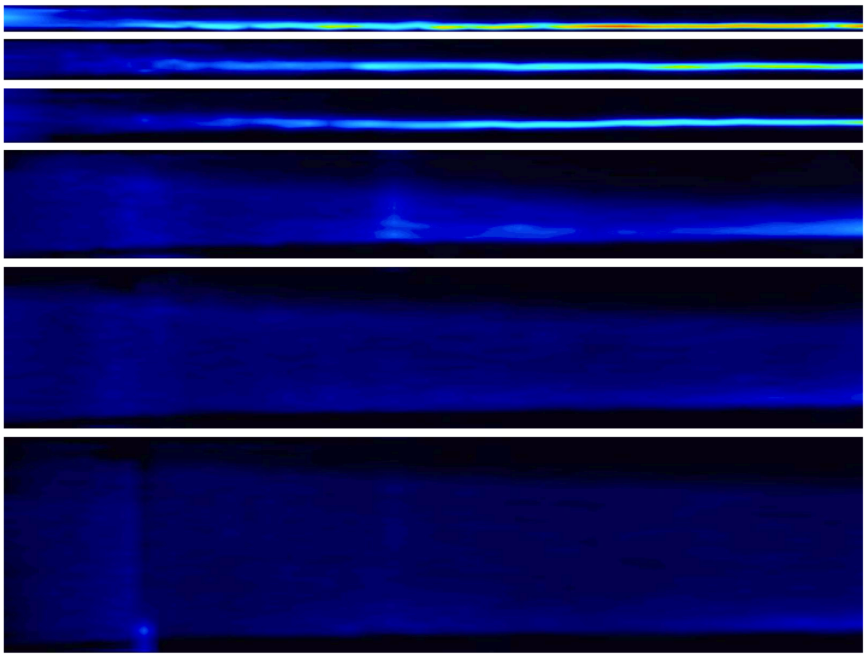

Figure B-4: Straightened images for U_{Avg}=0.367m/s. Dark blue is low intensity and red/white is high intensity seen when a focused streak is formed. All images are for decreasing Dean number devices.

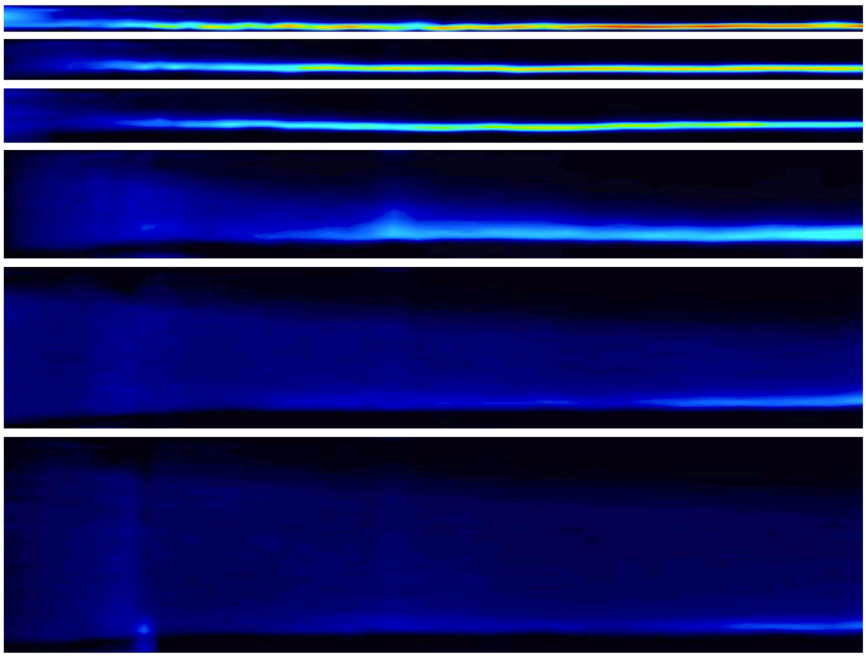

Figure B-5: Straightened images for U_{Avg}=0.516m/s. Dark blue is low intensity and red/white is high intensity seen when a focused streak is formed. All images are for decreasing Dean number devices.

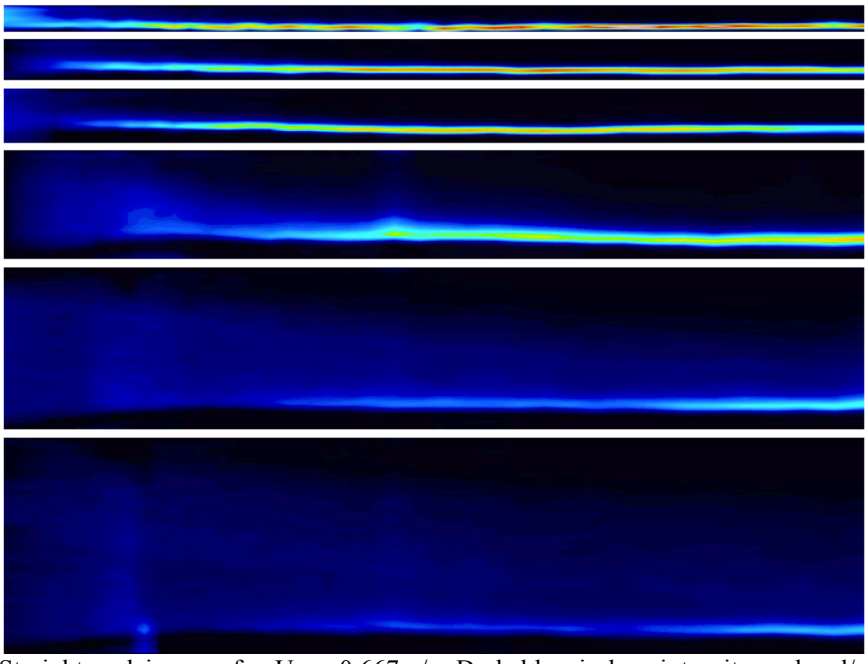

Figure B-6: Straightened images for U_{Avg}=0.667m/s. Dark blue is low intensity and red/white is high intensity seen when a focused streak is formed. All images are for decreasing Dean number devices.

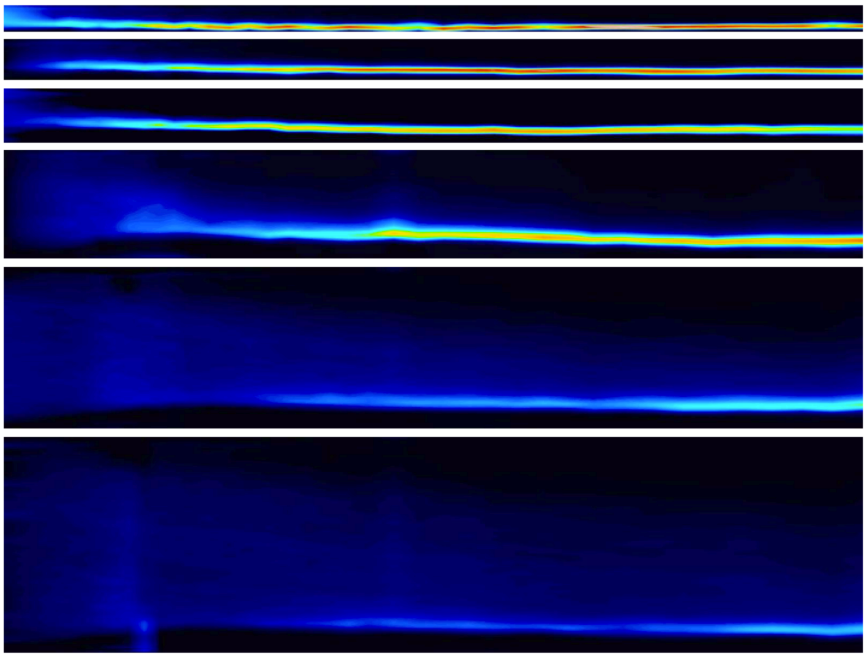

Figure B-7: Straightened images for U_{Avg}=0.733m/s. Dark blue is low intensity and red/white is high intensity seen when a focused streak is formed. All images are for decreasing Dean number devices.

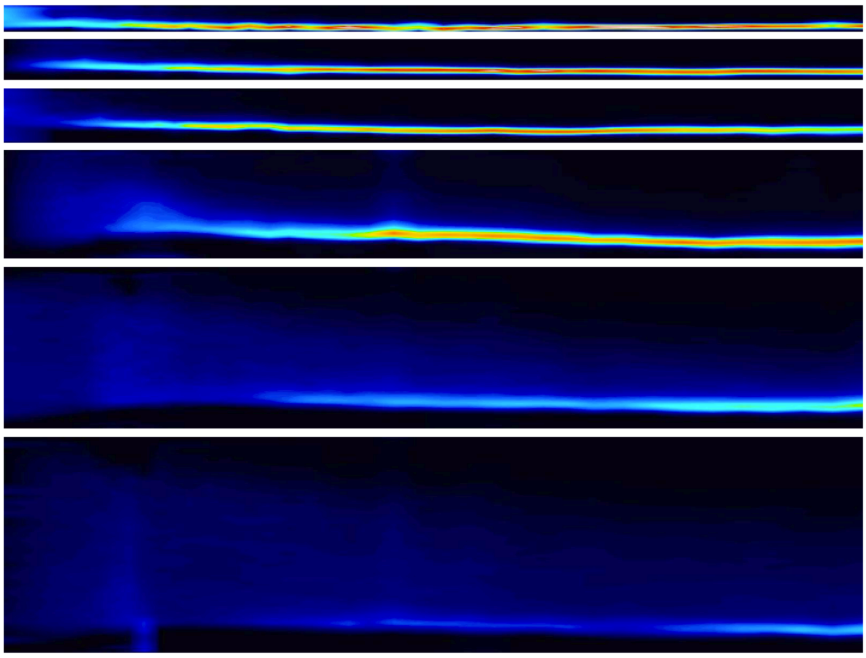

Figure B-8: Straightened images for U_{Avg}=0.774m/s. Dark blue is low intensity and red/white is high intensity seen when a focused streak is formed. All images are for decreasing Dean number devices.

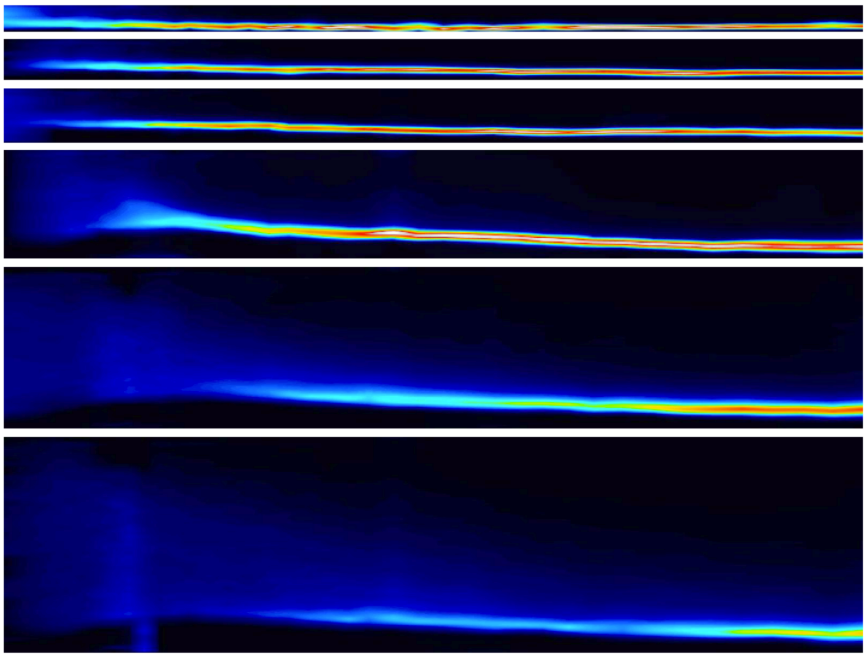

Figure B-9: Straightened images for U_{Avg}=1.000/s. Dark blue is low intensity and red/white is high intensity seen when a focused streak is formed. All images are for decreasing Dean number devices.

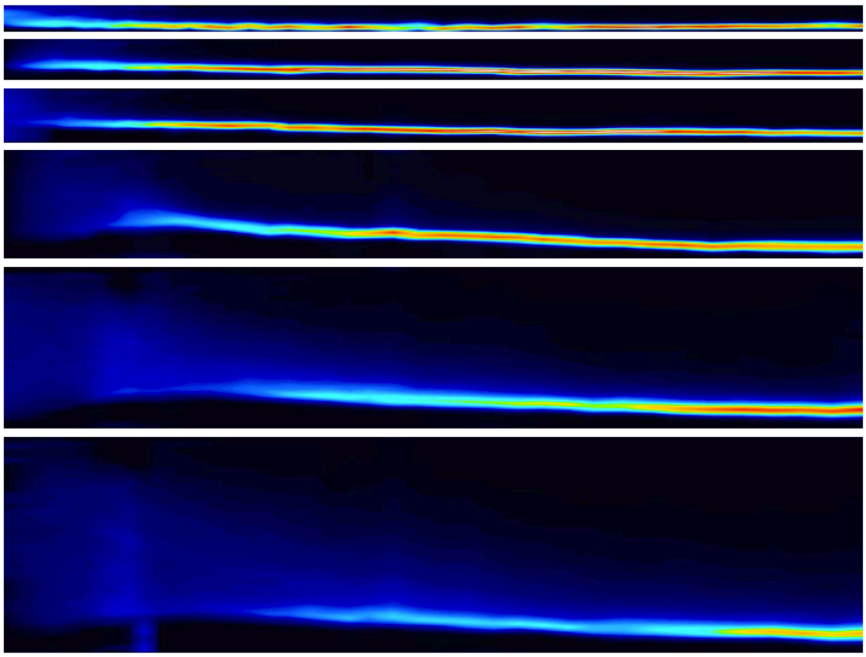

Figure B-10: Straightened images for U_{Avg}=1.032m/s. Dark blue is low intensity and red/white is high intensity seen when a focused streak is formed. All images are for decreasing Dean number devices.

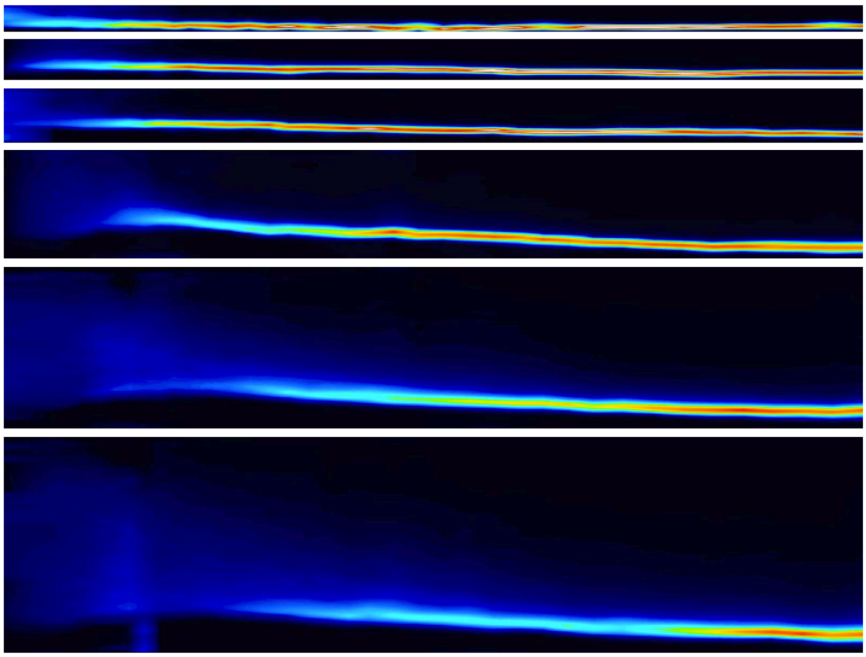

Figure B-11: Straightened images for U_{Avg}=1.100m/s. Dark blue is low intensity and red/white is high intensity seen when a focused streak is formed. All images are for decreasing Dean number devices.

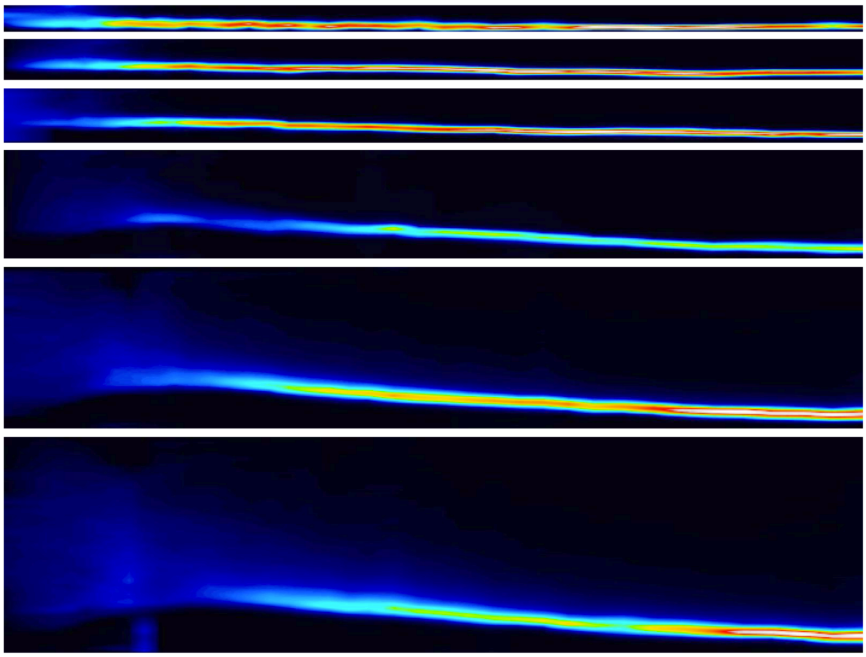

Figure B-12: Straightened images for U_{Avg}=1.290m/s. Dark blue is low intensity and red/white is high intensity seen when a focused streak is formed. All images are for decreasing Dean number devices.

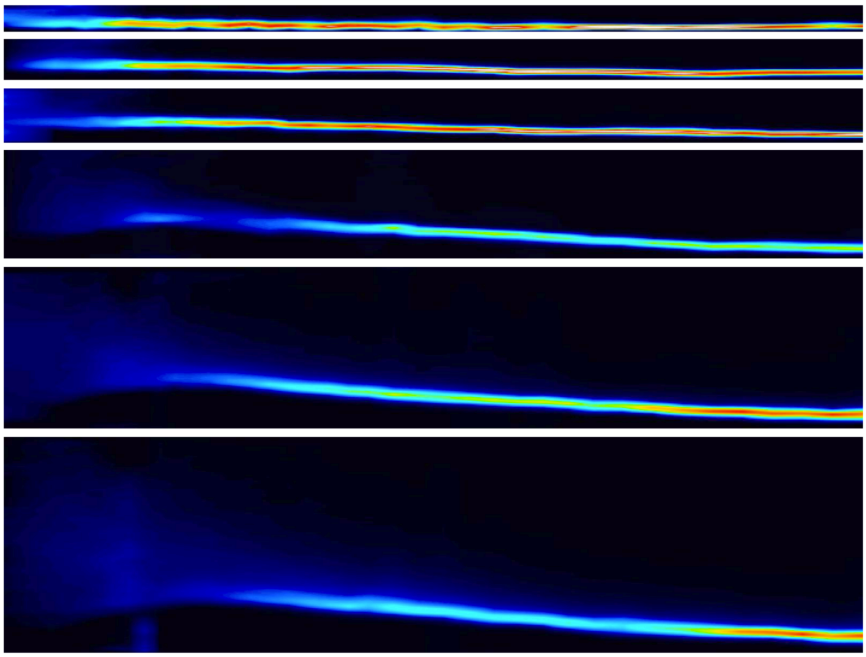

Figure B-13: Straightened images for U_{Avg}=1.333m/s. Dark blue is low intensity and red/white is high intensity seen when a focused streak is formed. All images are for decreasing Dean number devices.

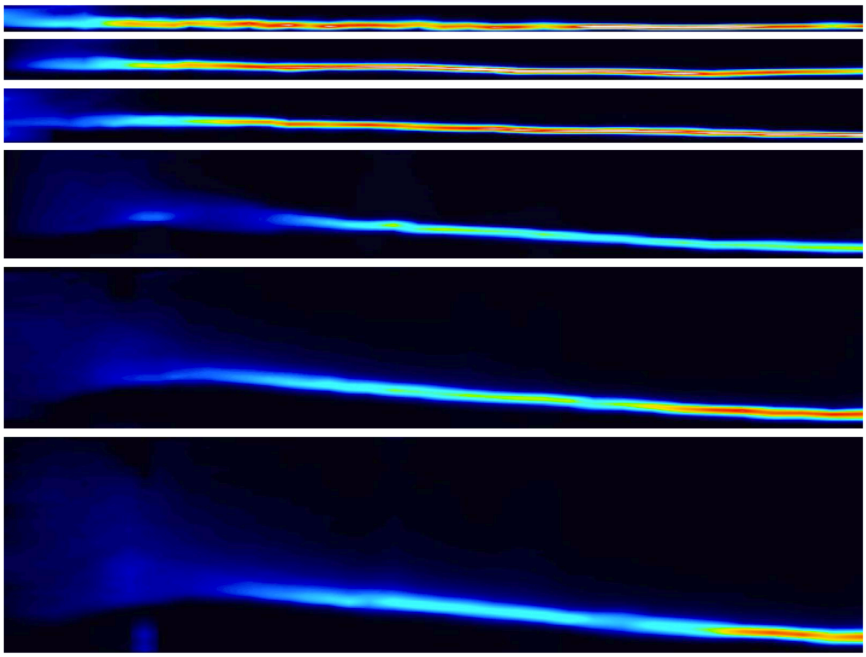

Figure B-14: Straightened images for U_{Avg}=1.467m/s. Dark blue is low intensity and red/white is high intensity seen when a focused streak is formed. All images are for decreasing Dean number devices.

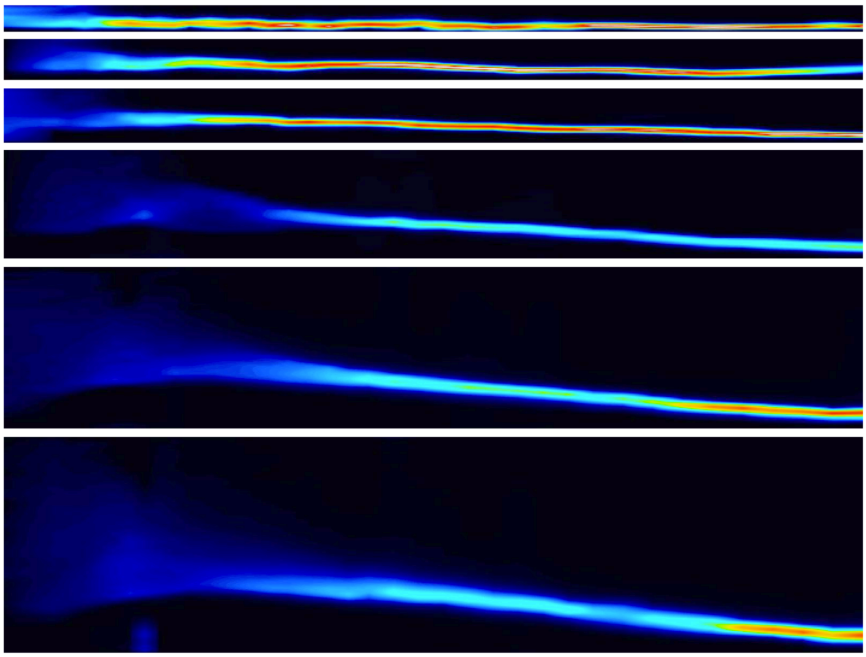

Figure B-15: Straightened images for U_{Avg}=1.667m/s. Dark blue is low intensity and red/white is high intensity seen when a focused streak is formed. All images are for decreasing Dean number devices.

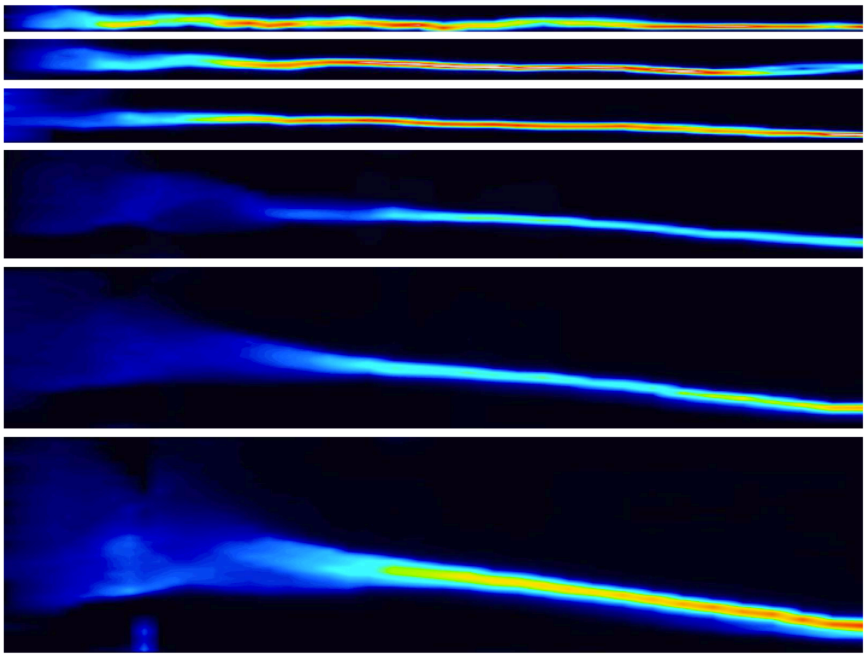

Figure B-16: Straightened images for U_{Avg}=2.000/s. Dark blue is low intensity and red/white is high intensity seen when a focused streak is formed. All images are for decreasing Dean number devices.

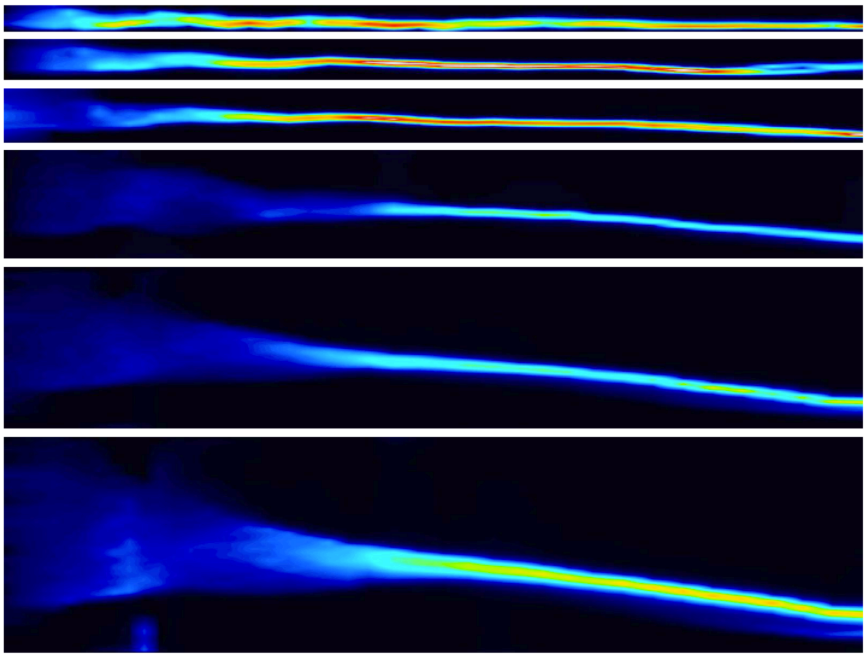

Figure B-17: Straightened images for U_{Avg}=2.200m/s. Dark blue is low intensity and red/white is high intensity seen when a focused streak is formed. All images are for decreasing Dean number devices.

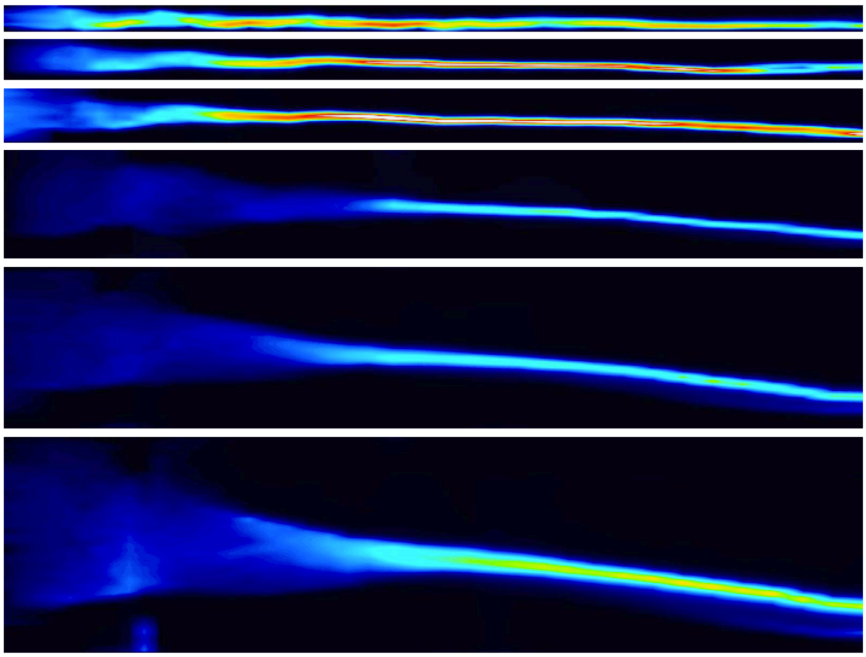

Figure B-18: Straightened images for U_{Avg}=2.333m/s. Dark blue is low intensity and red/white is high intensity seen when a focused streak is formed. All images are for decreasing Dean number devices.

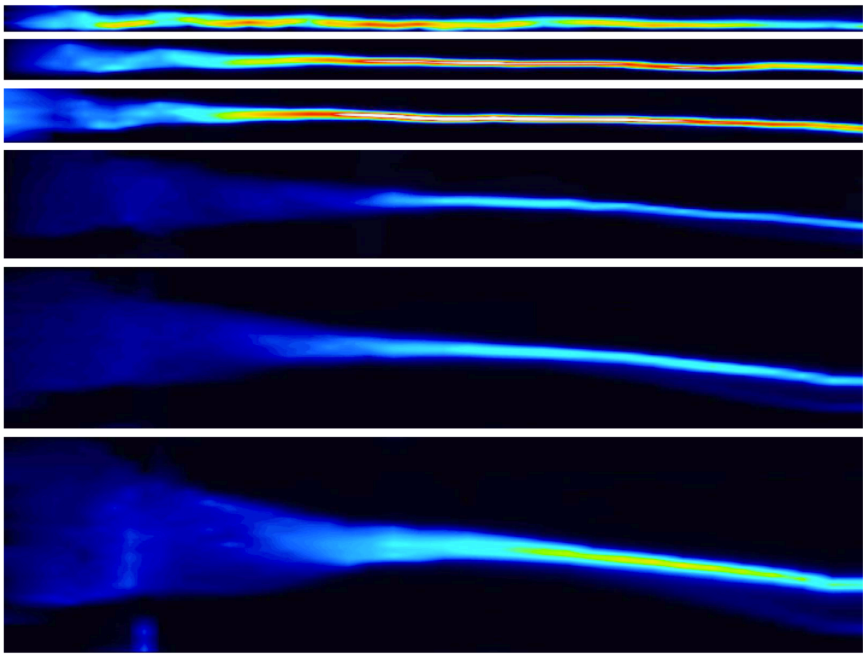

Figure B-19: Straightened images for U_{Avg}=2.667m/s. Dark blue is low intensity and red/white is high intensity seen when a focused streak is formed. All images are for decreasing Dean number devices.

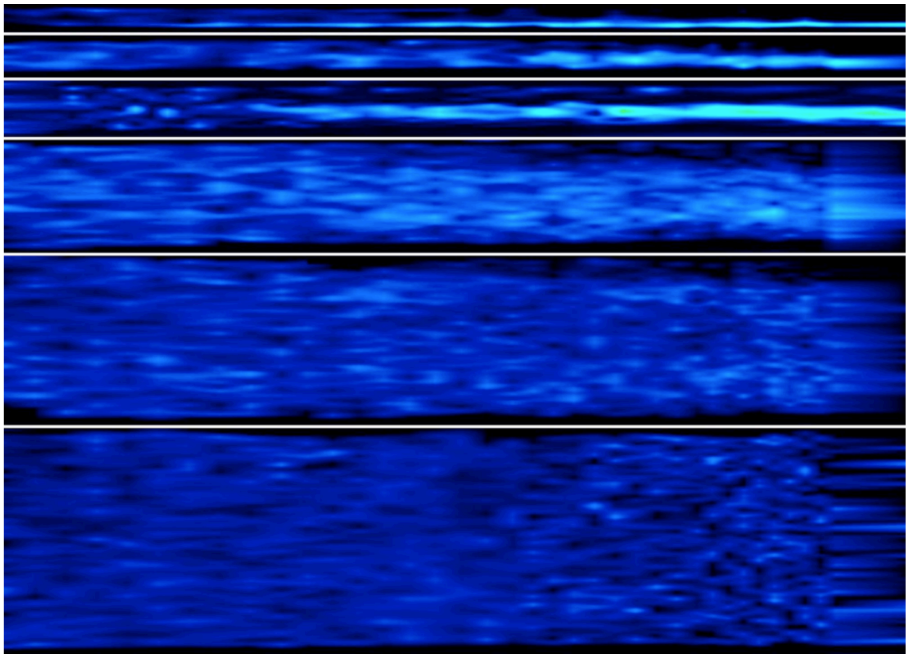

Figure B-20: Straightened images for U_{Avg}=0.133m/s. Dark blue is low intensity and red/white is high intensity seen when a focused streak is formed. All images are for increasing Dean number devices.

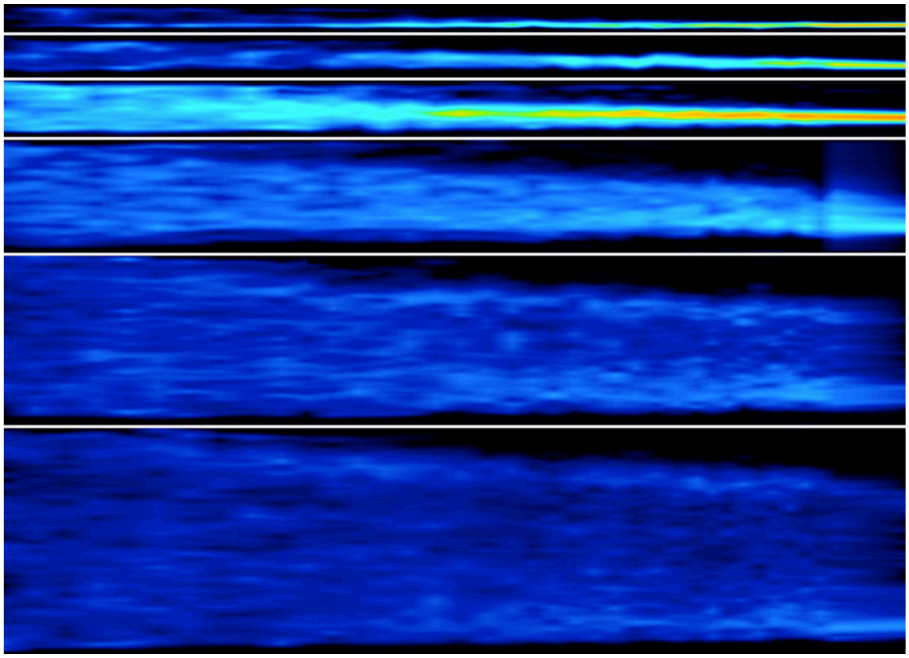

Figure B-21: Straightened images for U_{Avg}=0.333m/s. Dark blue is low intensity and red/white is high intensity seen when a focused streak is formed. All images are for increasing Dean number devices.

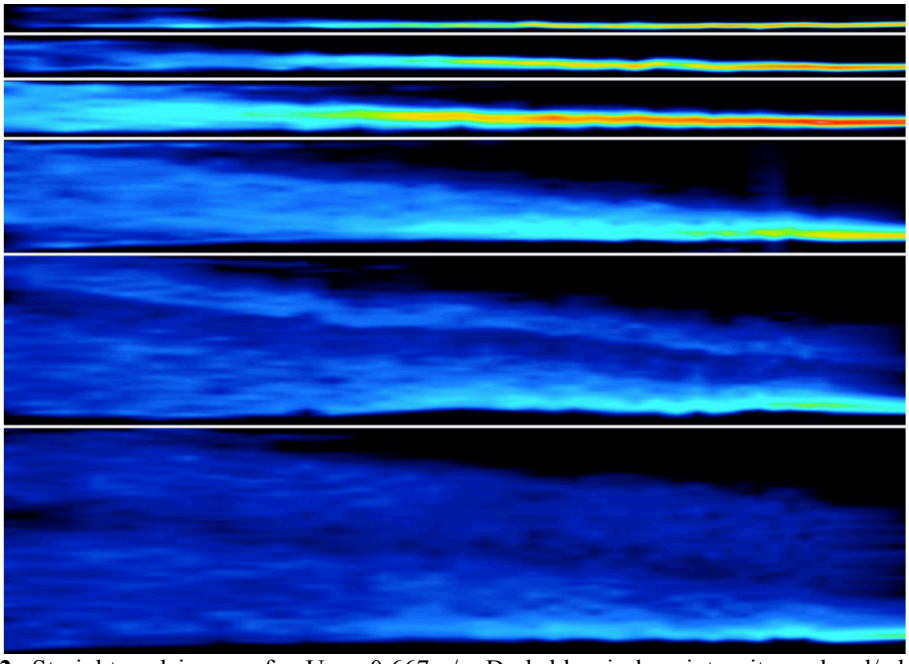

Figure B-22: Straightened images for U_{Avg}=0.667m/s. Dark blue is low intensity and red/white is high intensity seen when a focused streak is formed. All images are for increasing Dean number devices.

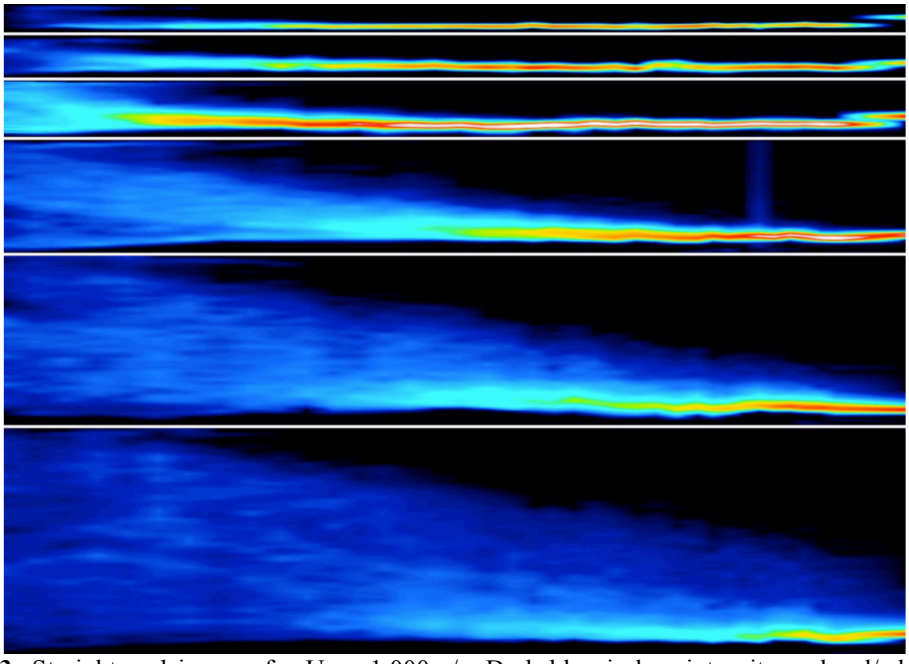

Figure B-23: Straightened images for U_{Avg}=1.000m/s. Dark blue is low intensity and red/white is high intensity seen when a focused streak is formed. All images are for increasing Dean number devices.

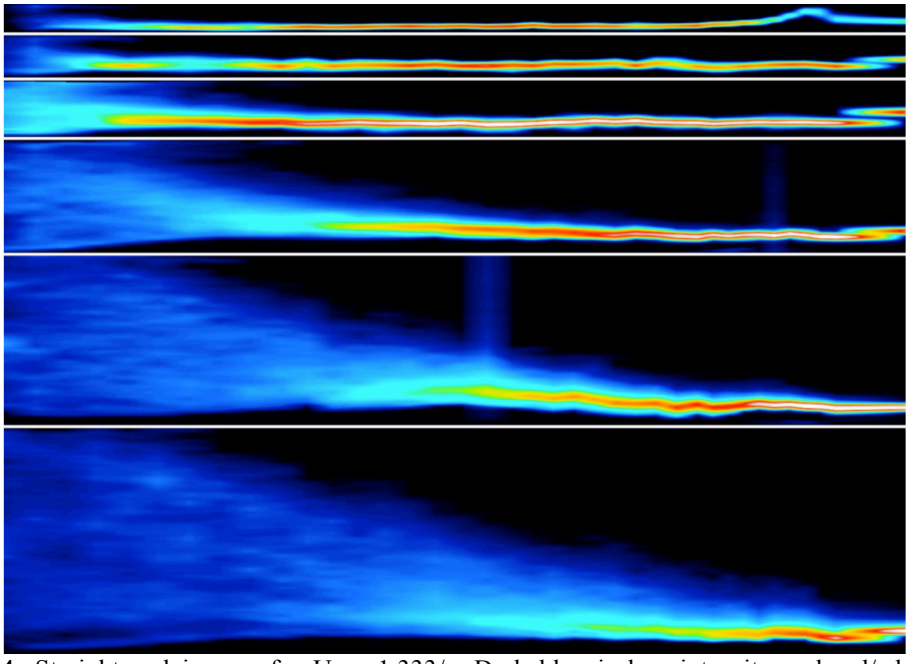

Figure B-24: Straightened images for U_{Avg}=1.333/s. Dark blue is low intensity and red/white is high intensity seen when a focused streak is formed. All images are for increasing Dean number devices.

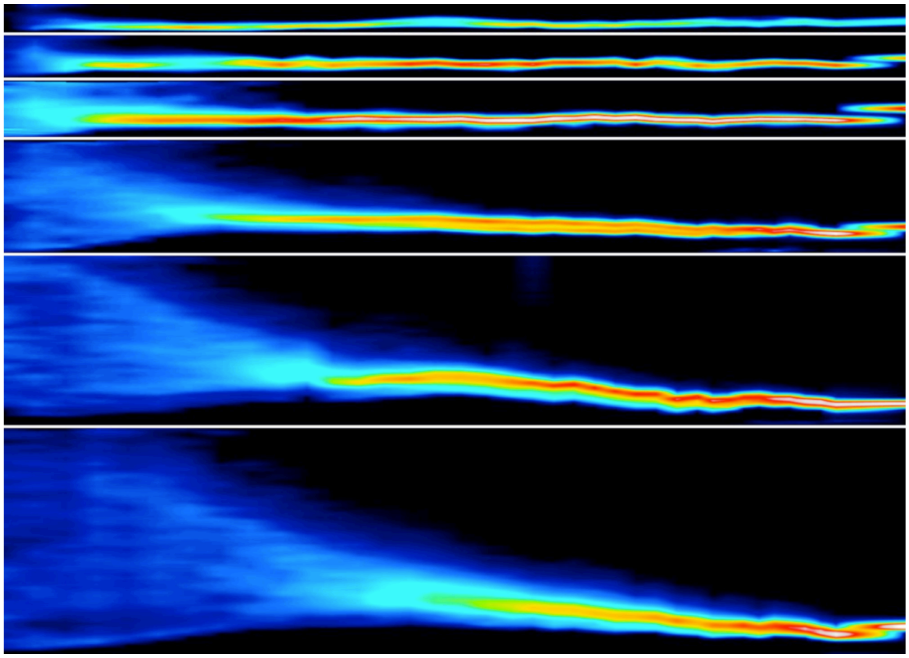

Figure B-25: Straightened images for U_{Avg}=1.667m/s. Dark blue is low intensity and red/white is high intensity seen when a focused streak is formed. All images are for increasing Dean number devices.

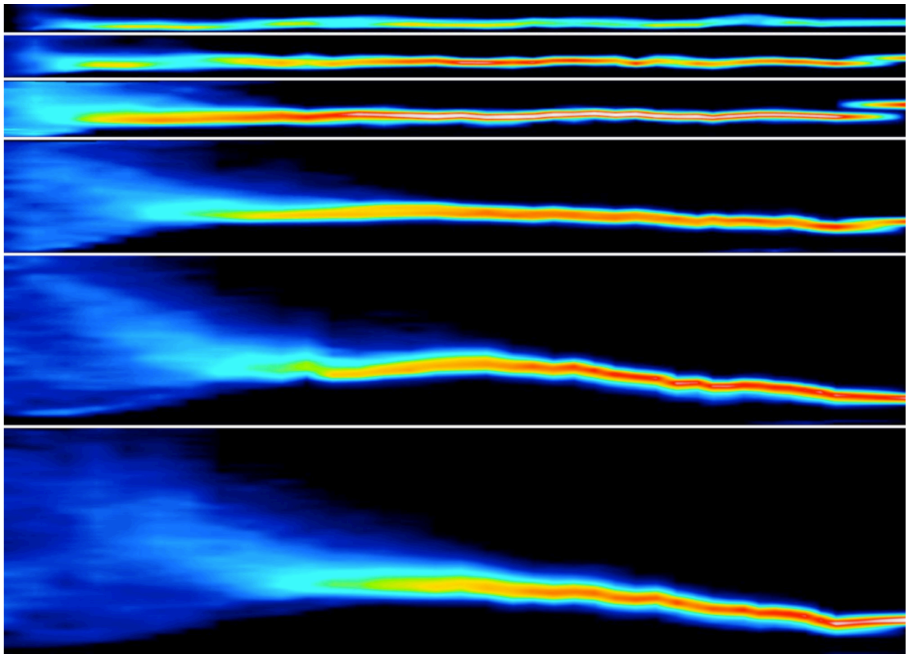

Figure B-26: Straightened images for U_{Avg}=2.000m/s. Dark blue is low intensity and red/white is high intensity seen when a focused streak is formed. All images are for increasing Dean number devices.

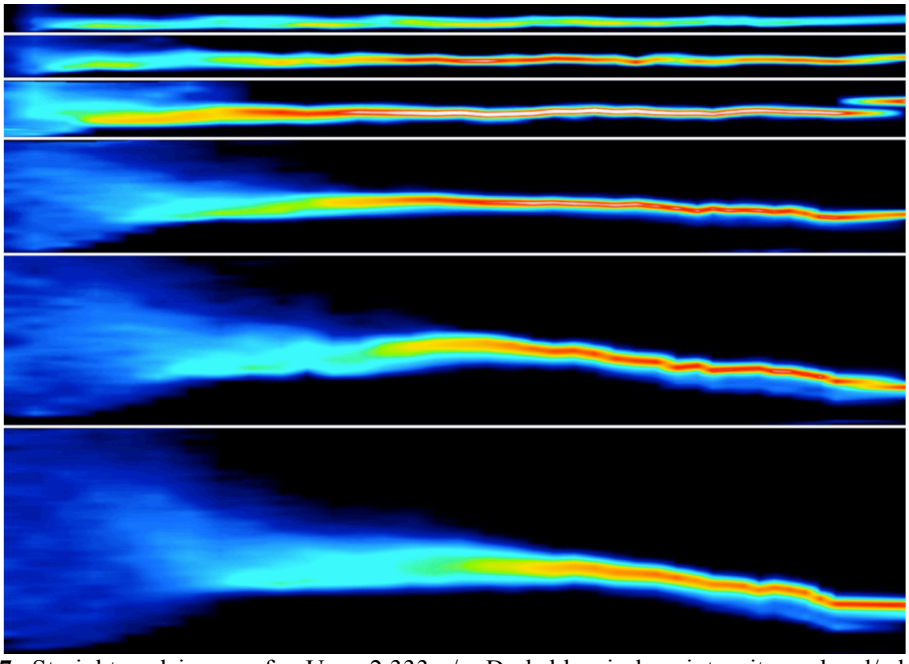

Figure B-27: Straightened images for U_{Avg}=2.333m/s. Dark blue is low intensity and red/white is high intensity seen when a focused streak is formed. All images are for increasing Dean number devices.

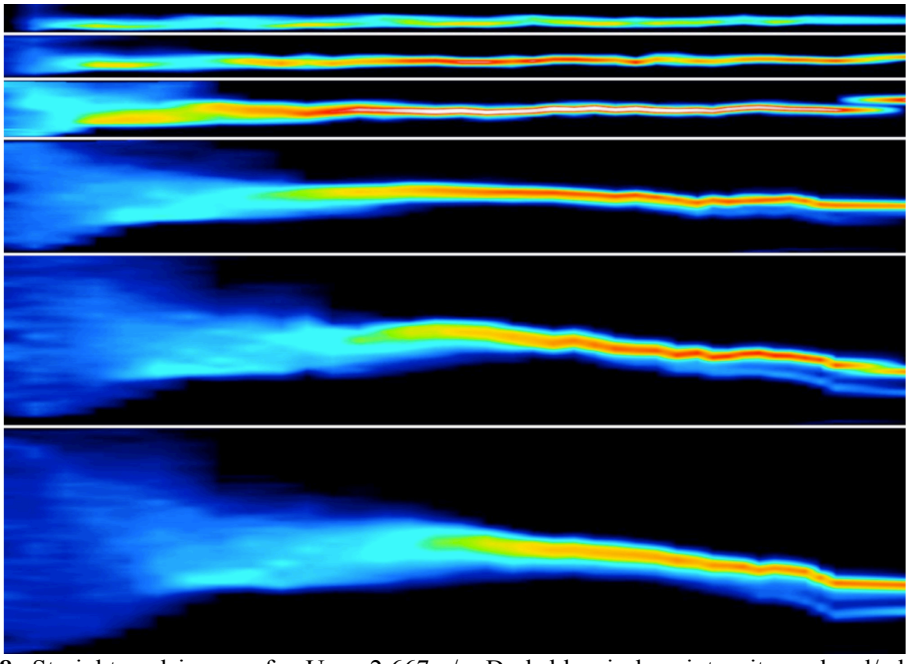

Figure B-28: Straightened images for U_{Avg}=2.667m/s. Dark blue is low intensity and red/white is high intensity seen when a focused streak is formed. All images are for increasing Dean number devices.

Appendix C

Digital Holographic Microscopy for 3D Positioning of Blurred Particles

C.1 Introduction

Obtaining 3D information on particles in microscale flows has been a topic of interest over the last 10 years [119]. Most of the technology development has surrounded improvements and translation of macro particle image velocimetry techniques to microfluidics, however, some newer techniques have been developed in order to reduce the number of cameras needed and fit within the architecture of existing microscopy equipment. While most PIV techniques utilize several images to understand the motion of particles in terms of their velocities in three dimensions, the application of these techniques to a single image requires perhaps less calculation but also the need for absolute reference. In other words, whereas PIV is investigating relative motion of the same particle, 3D positioning requires a reference plane and a means of determining the distance a particle is away from that plane. Only a few technologies allow for this means and in terms of accuracy are quite varied: Confocal microscopy, defocusing particle tracking, and digital holographic microscopy. Confocal is the most standard technique in biology for obtaining three-dimensional data. This technique limits the amount of out of focus light in an image utilizing a pinhole near the camera sensor. The z-resolution of the technique is based upon the optical properties of the microscope objective as well as the medium of the sample in addition to the wavelength of the light being used Equation C.1.

$$Res_z = 1.4\lambda_{exc} n/NA^2 \quad (C.1)$$

Defocusing particle tracking has the ability to achieve similar z-resolution utilizing a distance measurement (fluorescent wave front increasing in diameter as particle moves out of focus or triangular pattern of pinholes whose projection of the particle spread out as the particle moves further from the focal plane). There are other techniques available using multiple cameras. Digital holographic image analysis allows for the direct 3-dimensional measurement of a particle's position through the fitting of an out of focus image whose focal plane is below the sample on an inverted microscope. This out of focus image is then fit to a theoretical scattered image based upon Lorenz-Mie light scattering theory [120]. This can have resolution a few orders of magnitude better than the other mentioned techniques.

This appendix details preliminary results of 3D positioning of particles inside the same channels used in Chapter 4 and 5 in an attempt to investigate the 3D effects of inertial focusing in curved channels. While other holographic methods have been used for the examination of inertial focusing particle distributions [111, 114, 121], the current technique is accomplished without image reconstruction drastically reducing the z-positioning computational time.

C.2 Methods

A Vision Research Phantom v7.3 high-speed camera was utilized with a 635nm 50mW laser light source. Due to the high-speed nature of inertial focusing flows (up to 8m/s), particle blurring occurs even with a 1μs exposure time and was thereby accounted for by also fitting the velocity of the particle in addition to the other parameters and theoretically blurring the particle over a given distance. Figure C-1 briefly explains

holography and gives example holograms and their blurred fits. The theoretical fit is determined through the random sampling and fitting of pixels throughout a square set of pixels centered on the hologram center. Figure C-2 shows examples of the blurred images at different flow rates.

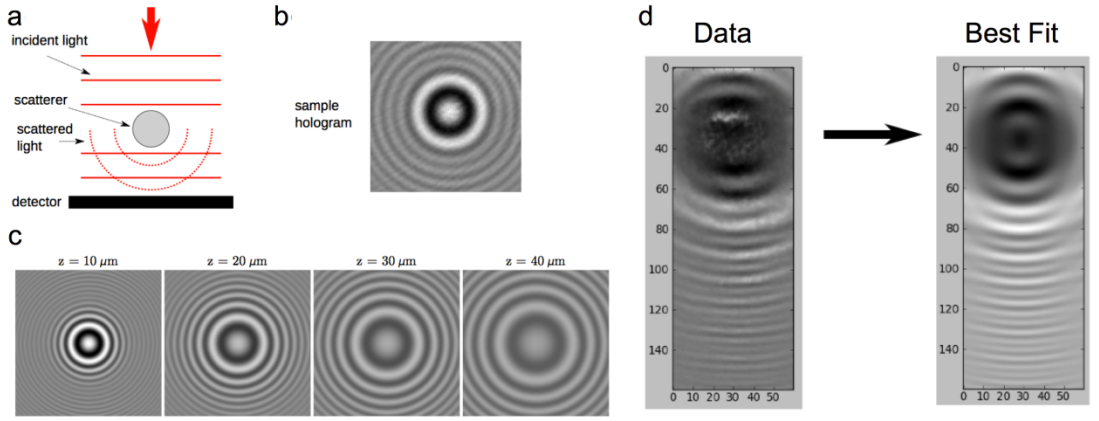

Figure C-1: (a) Image of holography concept, (b) example stationary hologram, (c) Lorenz-Mie theory produced holograms of a particle at different distances from the focal plane and (d) an example blurred holograms and their theoretical fits that determine the measured z-position relative to the focal plane [120].

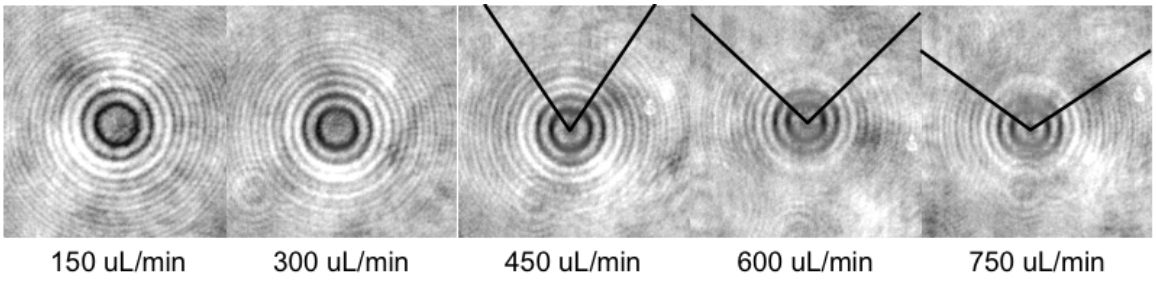

Figure C-2: Blurred holograms showing the effect of particle velocity (fluid flow rate).

After acquiring the images several steps were needed prior to fitting the holograms to theory. Tens of thousands of images were collected yet only a fraction had non-overlapping holograms. Since it is easier and more accurate to fit only single particles at a time this data was preprocessed. This reduction in data set was accomplished using a continuously updated background subtraction and absolute difference between the current image and the background image (average of five prior images without a particle). The thresholds were adjusted within each data set. Two different thresholds were needed: one

for selecting an image with a particle and two images that would be added as background frames.

C.3 Results

Preliminary data with refractive index matched fluids were collected at a flow rate of 300µL/min in a PDMS 100µm wide 50µm high channel similar to those used in Chapter 3 with 10µm particles. The distribution of particle positions match the two expected vertical streak positions predicted theoretically. The distribution of particles across the width of the channel were not significantly different considering the low number of holograms processed and the total number whose positions were averaged in the fluorescent streak image.

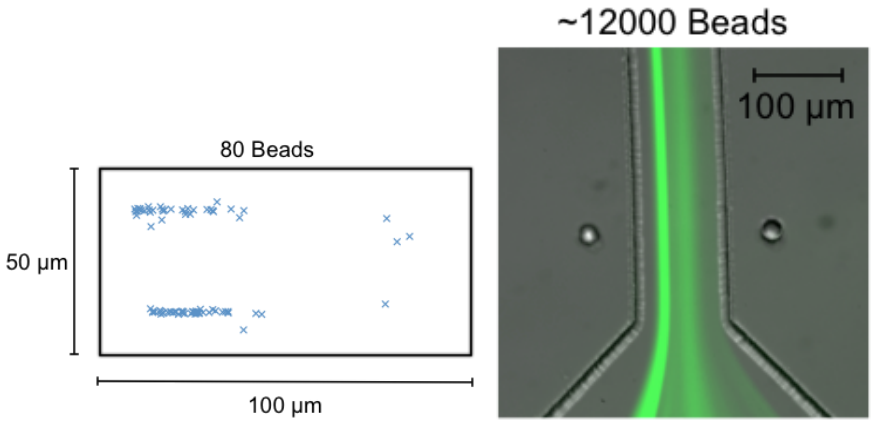

Figure C-3: Comparison of fluorescent streak image (~12000 beads) to the measurements of 80 holograms. Solution in this case was 10µm polystyrene beads refractive index matched with ~50% DMSO in water. This increased the viscosity by approximately a factor of 2 leading to a different than expected focusing pattern.

Preliminary data with non-index matched fluids were completed in an epoxy δ=0.129 device with 4.44µm beads. Imaging parameters are still being varied. Essentially, we are detecting particles but they are not being fit well and thus one z-position set of particles is being thrown out due to the low fitting values (a reduced R^2 threshold used for plots in Figure C-4).

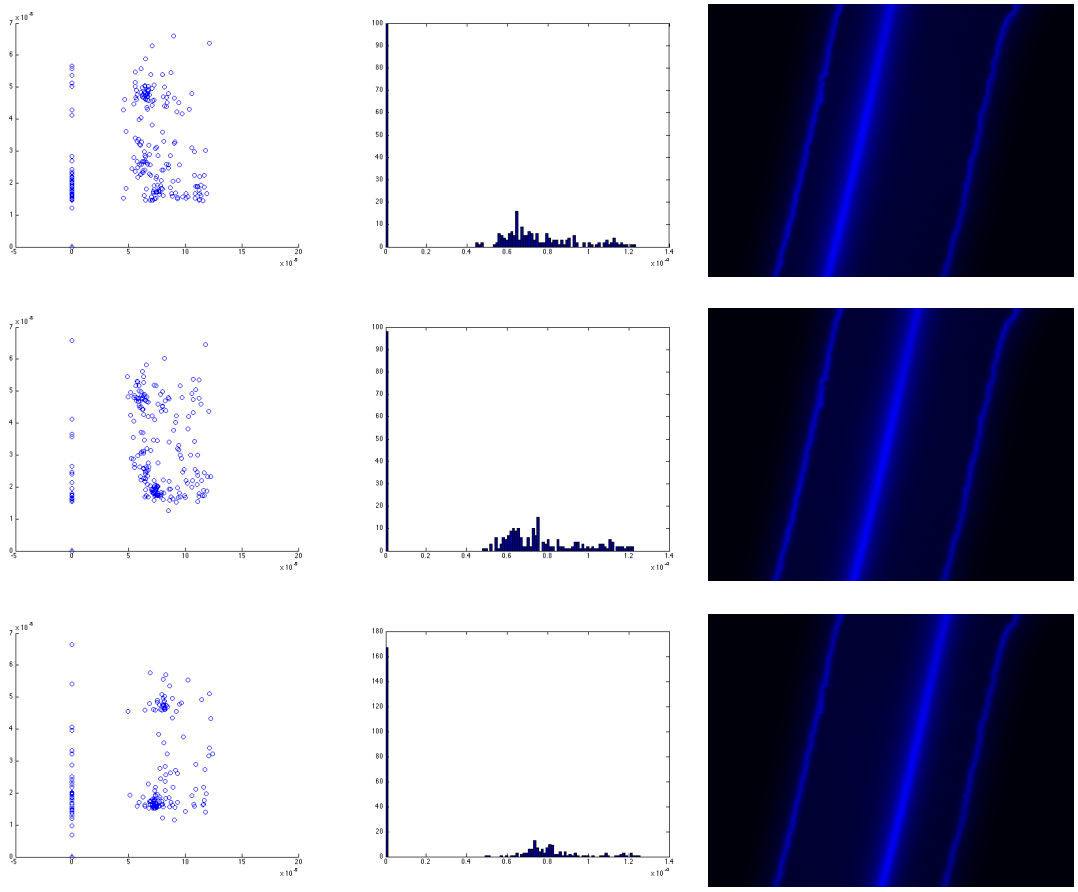

Figure C-4: Scatter plots collected for a δ=0.129 device with 4.44μm beads at several flow rates. Data is plotted both as x-z scatter plots (left) in position and as a histogram across the width of the channel, mimicking a fluorescent intensity profile plot (center) as well as fluorescent streak images taken with a separate device (right).

The data does not show as strong of lateral movement compared to the fluorescent images. There is also more scatter in the data, which is to be expected for the smaller particles but still seems less tightly focused than the fluorescent images.

C.4 Conclusions & Future Improvements

With the newest data, there is a bias in the image preprocessing using thresholds on the absolute difference between the current image and the background. There is an unknown source of variation in the images, which effectively changes the background to not only keep blank images but incorrectly remove images with particles.

Data should be more directly compared between devices in the future. Currently, different devices are used for the separate imaging setups. Being able to verify in both systems with the same fluids should help improve confidence in the results.

With further improved imaging optics (faster high speed camera-500ns exposure or pulsed laser illumination-8ns exposure) it is also possible to reduce the number of parameters requiring fitting for the improved speed of analysis.

With this type of data a cross sectional distribution of particles can be determined at a wide range of flow conditions. In general, these results, while currently in a small batch mode, could be improved to provide sufficient statistics for positions within the cross section adding the last piece of the puzzle with excellent z-resolution in order to understand the mechanisms of inertial focusing in curved channels.

References

[1] S. L. Stott, R. J. Lee, S. Nagrath, M. Yu, D. T. Miyamoto, L. Ulkus*, et al.*, "Isolation and Characterization of Circulating Tumor Cells from Patients with Localized and Metastatic Prostate Cancer," *Science Translational Medicine,* vol. 2, pp. 25ra23-25ra23, Mar 31 2010.

[2] S. L. Stott, C. H. Hsu, D. I. Tsukrov, M. Yu, D. T. Miyamoto, B. A. Waltman*, et al.*, "Isolation of circulating tumor cells using a microvortex-generating herringbone-chip," *Proceedings of the National Academy of Sciences,* vol. 107, p. 18392, 2010.

[3] D. T. Miyamoto, R. J. Lee, S. L. Stott, D. T. Ting, B. S. Wittner, M. Ulman*, et al.*, "Androgen Receptor Signaling in Circulating Tumor Cells as a Marker of Hormonally Responsive Prostate Cancer," *Cancer Discovery,* vol. 2, pp. 995-1003, Nov 1 2012.

[4] M. Yu, D. T. Ting, S. L. Stott, B. S. Wittner, F. Ozsolak, S. Paul*, et al.*, "RNA sequencing of pancreatic circulating tumour cells implicates WNT signalling in metastasis," *Nature,* vol. 487, pp. 510-513, Mar 31 2105.

[5] L. L. Horvath, D. R. Hospenthal, C. K. Murray, and D. P. Dooley, "Detection of Simulated Candidemia by the BACTEC 9240 System with Plus Aerobic/F and Anaerobic/F Blood Culture Bottles," *Journal of Clinical Microbiology,* vol. 41, pp. 4714-4717, Oct 1 2003.

[6] M. Morrell, V. J. Fraser, and M. H. Kollef, "Delaying the Empiric Treatment of Candida Bloodstream Infection until Positive Blood Culture Results Are Obtained: a Potential Risk Factor for Hospital Mortality," *Antimicrobial Agents and Chemotherapy,* vol. 49, pp. 3640-3645, Sep 1 2005.

[7] R. E. Zuna and A. Behrens, "Peritoneal washing cytology in gynecologic cancers: long-term follow-up of 355 patients," *Journal of the National Cancer Institute,* vol. 88, pp. 980-987, 1996.

[8] S. D. Lee, K. W. Ryu, B. W. Eom, J. H. Lee, M. C. Kook, and Y.-W. Kim, "Prognostic significance of peritoneal washing cytology in patients with gastric cancer," *Br J Surg,* vol. 99, pp. 397-403, Nov 18 2011.

[9] N. Sneige, J. B. Thomison, A. Malpica, Y. Gong, J. Ensor, and E. G. Silva, "Peritoneal washing cytologic analysis of ovarian serous tumors of low malignant potential to detect peritoneal implants and predict clinical outcome," *Cancer Cytopathology,* vol. 120, pp. 238-244, Jul 23 2012.

[10] V. Hird, H. Thomas, J. Stewart, and A. Epenetos, "Malignant ascites: review of the literature, and an update on monoclonal antibody-targeted therapy," *European Journal of Obstetrics & Gynecology and Reproductive Biology,* vol. 32, pp. 37-45, 1989.

[11] G. W. Hunninghake, J. Gadek, O. Kawanami, V. Ferrans, and R. Crystal, "Inflammatory and immune processes in the human lung in health and disease: evaluation by bronchoalveolar lavage.," *The American journal of pathology,* vol. 97, p. 149, 1979.

[12] R. F. Henderson, "Use of Bronchoalveolar Lavage to Detect Lung Damage," *Environmental Health Perspectives,* vol. 56, pp. 115-129, May 23 1984.

[13] F. W. Kahn and J. M. Jones, "Analysis of bronchoalveolar lavage specimens from immunocompromised patients with a protocol applicable in the microbiology laboratory.," *Journal of clinical microbiology,* vol. 26, pp. 1150-1155, 1988.
[14] K. C. Meyer, "The role of bronchoalveolar lavage in interstitial lung disease," *Clinics in chest medicine,* vol. 25, pp. 637-650, 2004.
[15] P. Haslam, C. Turton, B. Heard, A. Lukoszek, J. Collins, A. Salsbury*, et al.*, "Bronchoalveolar lavage in pulmonary fibrosis: comparison of cells obtained with lung biopsy and clinical features," *Thorax,* vol. 35, pp. 9-18, 1980.
[16] M. Potter, R. Morris, A. Ferguson, and A. Wyllie, "Detection of mutations associated with colorectal cancer in DNA from whole-gut lavage fluid," *Journal of the National Cancer Institute,* vol. 90, pp. 623-626, 1998.
[17] C. Ottiger and A. R. Huber, "Quantitative urine particle analysis: integrative approach for the optimal combination of automation with UF-100 and microscopic review with KOVA cell chamber," *Clinical chemistry,* vol. 49, pp. 617-623, 2003.
[18] J. A. Simerville, W. C. Maxted, and J. J. Pahira, "Urinalysis: a comprehensive review.," *American family physician,* vol. 71, p. 1153, 2005.
[19] S. Choi, S. Song, C. Choi, and J. K. Park, "Hydrophoretic sorting of micrometer and submicrometer particles using anisotropic microfluidic obstacles," *Analytical Chemistry,* vol. 81, pp. 50-55, 2008.
[20] K. Loutherback, K. S. Chou, J. Newman, J. Puchalla, R. H. Austin, and J. C. Sturm, "Improved performance of deterministic lateral displacement arrays with triangular posts," *Microfluidics and Nanofluidics,* pp. 1-7, May 21 2010.
[21] D. Huh, J. Bahng, Y. Ling, H. Wei, O. Kripfgans, J. Fowlkes*, et al.*, "A Gravity-Driven Microfluidic Particle Sorting Device with Hydrodynamic Separation Amplification," *Analytical chemistry,* vol. 79, p. 1369, 2007.
[22] K. Morton, K. Loutherback, D. Inglis, O. Tsui, J. Sturm, S. Chou*, et al.*, "Hydrodynamic metamaterials: Microfabricated arrays to steer, refract, and focus streams of biomaterials," *Proceedings of the National Academy of Sciences,* vol. 105, p. 7434, 2008.
[23] S. Choi, T. Ku, S. Song, C. Choi, and J.-K. Park, "Hydrophoretic high-throughput selection of platelets in physiological shear-stress range," *Lab on a Chip,* pp. 1-6, Jan 1 2011.
[24] S. Choi, S. Song, C. Choi, and J. Park, "Continuous blood cell separation by hydrophoretic filtration," *Lab Chip,* vol. 7, pp. 1532-1538, 2007.
[25] L. R. Huang, E. C. Cox, R. H. Austin, and J. C. Sturm, "Continuous particle separation through deterministic lateral displacement," *Science,* vol. 304, pp. 987-990, 2004.
[26] D. W. Inglis, J. A. Davis, R. H. Austin, and J. C. Sturm, "Critical particle size for fractionation by deterministic lateral displacement," *Lab on a Chip,* vol. 6, p. 655, Jan 1 2006.
[27] J. Kralj, M. Lis, M. Schmidt, and K. Jensen, "Continuous dielectrophoretic size-based particle sorting," *Anal. Chem,* vol. 78, pp. 5019-5025, 2006.
[28] J. Zhu, T.-R. J. Tzeng, and X. Xuan, "Continuous dielectrophoretic separation of particles in a spiral microchannel," *Electrophoresis,* vol. 31, pp. 1382-1388, Apr 1 2010.

[29] J. Voldman, "Electrical Forces For Microscale Cell Manipulation," *Annual Review of Biomedical Engineering,* vol. 8, pp. 425-454, Aug 1 2006.
[30] F. Petersson, L. Åberg, A. M. Swärd-Nilsson, and T. Laurell, "Free flow acoustophoresis: microfluidic-based mode of particle and cell separation," *Anal. Chem,* vol. 79, pp. 5117-5123, 2007.
[31] S. Miltenyi, W. Müller, W. Weichel, and A. Radbruch, "High gradient magnetic cell separation with MACS," *Cytometry,* vol. 11, pp. 231-238, 1990.
[32] M. Toner and D. Irimia, "Blood-on-a-chip," *Annual Review of Biomedical Engineering,* vol. 7, pp. 77-103, 2005.
[33] A. Lenshof and T. Laurell, "Continuous separation of cells and particles in microfluidic systems," *Chemical Society Reviews,* vol. 39, pp. 1203-1217, 2010.
[34] D. R. Gossett, W. M. Weaver, A. J. Mach, S. C. Hur, H. T. K. Tse, W. Lee*, et al.*, "Label-free cell separation and sorting in microfluidic systems," *Anal Bioanal Chem,* pp. 1-19, Apr 25 2010.
[35] H. Tsutsui and C.-M. Ho, "Cell separation by non-inertial force fields in microfluidic systems," *Mechanics Research Communications,* vol. 36, pp. 92-103, Jan 1 2009.
[36] G. Whitesides, "The origins and the future of microfluidics," *Nature,* vol. 442, p. 368, 2006.
[37] G. Segré, "Radial particle displacements in Poiseuille flow of suspensions," *Nature,* vol. 189, pp. 209-210, 1961.
[38] G. Segre and A. Silberberg, "Behavior of macroscopic rigid spheres in Poiseuille flow," *J Fluid Mech,* vol. 14, pp. 115-135, 1961.
[39] G. Segre and A. Silberberg, "Behaviour of macroscopic rigid spheres in Poiseuille flow Part 1. Determination of local concentration by statistical analysis of particle passages through crossed light beams," *Journal of Fluid Mechanics,* vol. 14, pp. 115-135, 1962.
[40] F. Bretherton, "The motion of rigid particles in a shear flow at low Reynolds number," *J. Fluid Mech,* vol. 14, pp. 284-304, 1962.
[41] S. Rubinow and J. B. Keller, "The transverse force on a spinning sphere moving in a viscous fluid," *Journal of Fluid Mechanics,* vol. 11, pp. 447-459, 1961.
[42] J. Matas, J. Morris, and E. Guazzelli, "Lateral forces on a sphere," *Oil & Gas Science and Technology,* vol. 59, pp. 59-70, 2004.
[43] J. Feng, H. Hu, and D. Joseph, "Direct simulation of initial value problems for the motion of solid bodies in a Newtonian fluid. Part 2. Couette and Poiseuille flows," *Journal of Fluid Mechanics,* vol. 277, pp. 271-301, 1994.
[44] P. G. Saffman, "The lift on a small sphere in a slow shear flow," *Journal of fluid mechanics,* vol. 22, pp. 385-400, 1965.
[45] R. Repetti and E. Leonard, "Segré-Silberberg annulus formation: a possible explanation," *Nature,* vol. 203, pp. 1346-1348, 1964.
[46] R. Jeffrey and J. Pearson, "Particle motion in laminar vertical tube flow," *Journal of Fluid Mechanics,* vol. 22, pp. 721-735, 2006.
[47] B. Ho and L. Leal, "Inertial migration of rigid spheres in two-dimensional unidirectional flows," *Journal of Fluid Mechanics,* vol. 65, pp. 365-400, 1974.

[48] P. Vasseur and R. Cox, "The lateral migration of a spherical particle in two-dimensional shear flows," *Journal of Fluid Mechanics,* vol. 78, pp. 385-413, 1976.
[49] E. Asmolov, "The inertial lift on a spherical particle in a plane Poiseuille flow at large channel Reynolds number," *Journal of Fluid Mechanics,* vol. 381, pp. 63-87, 1999.
[50] J.-P. Matas, J. Morris, and É. Guazzelli, "Lateral force on a rigid sphere in large-inertia laminar pipe flow," *Journal of Fluid Mechanics,* vol. 621, pp. 59-67, Jan 1 2009.
[51] X. Shao, Z. Yu, and B. Sun, "Inertial migration of spherical particles in circular Poiseuille flow at moderately high Reynolds numbers," *Phys. Fluids,* vol. 20, p. 103307, Jan 1 2008.
[52] B. Chun and A. Ladd, "Inertial migration of neutrally buoyant particles in a square duct: An investigation of multiple equilibrium positions," *Physics of Fluids,* vol. 18, p. 031704, 2006.
[53] D. Di Carlo, D. Irimia, R. Tompkins, and M. Toner, "Continuous inertial focusing, ordering, and separation of particles in microchannels," *Proceedings of the National Academy of Sciences,* vol. 104, p. 18892, 2007.
[54] D. Di Carlo, "Inertial microfluidics," *Lab Chip,* vol. 9, p. 3038, Jan 1 2009.
[55] D. Di Carlo, J. Edd, K. Humphry, H. Stone, and M. Toner, "Particle Segregation and Dynamics in Confined Flows," *Phys. Rev. Lett.,* vol. 102, p. 094503, Mar 1 2009.
[56] J. Zhou and I. Papautsky, "Fundamentals of inertial focusing in microchannels," *Lab on a Chip,* Jan 1 2013.
[57] J. Zhou, P. V. Giridhar, S. Kasper, and I. Papautsky, "Modulation of aspect ratio for complete separation in an inertial microfluidic channel," *Lab Chip,* pp. 1-11, Jan 1 2013.
[58] A. J. Mach and D. Di Carlo, "Continuous scalable blood filtration device using inertial microfluidics," *Biotechnol. Bioeng.,* vol. 107, pp. 302-311, Jun 29 2010.
[59] S. C. Hur, S. E. Choi, S. Kwon, and D. Di Carlo, "Inertial focusing of non-spherical microparticles," *Applied Physics Letters,* vol. 99, p. 044101, 2011.
[60] M. Masaeli, E. Sollier, H. Amini, W. Mao, K. Camacho, N. Doshi*, et al.*, "Continuous Inertial Focusing and Separation of Particles by Shape," *Phys. Rev. X,* vol. 2, p. 031017, Sep 1 2012.
[61] S. C. Hur, N. K. Henderson-Maclennan, E. R. B. Mccabe, and D. Di Carlo, "Deformability-based cell classification and enrichment using inertial microfluidics," *Lab on a Chip,* pp. 1-9, Jan 1 2011.
[62] F. Takemura, S. Takagi, J. Magnaudet, and Y. Matsumoto, "Drag and lift forces on a bubble rising near a vertical wall in a viscous liquid," *Journal of Fluid Mechanics,* vol. 461, pp. 1-24, Jun 11 2002.
[63] F. Takemura and J. Magnaudet, "The transverse force on clean and contaminated bubbles rising near a vertical wall at moderate Reynolds number," *Journal of Fluid Mechanics,* vol. 495, p. S0022112003006232, Nov 25 2003.
[64] L. Leal, "Particle motions in a viscous fluid," *Annual Review of Fluid Mechanics,* vol. 12, pp. 435-476, 1980.

[65] D. R. Gossett, H. T. K. Tse, S. A. Lee, Y. Ying, A. G. Lindgren, O. O. Yang*, et al.*, "Hydrodynamic stretching of single cells for large population mechanical phenotyping," *Proceedings of the National Academy of Sciences,* vol. 109, pp. 7630-7635, 2012.

[66] W. Lee, H. Amini, H. A. Stone, and D. Di Carlo, "Dynamic self-assembly and control of microfluidic particle crystals," *Proceedings of the National Academy of Sciences,* vol. 107, p. 22413, 2010.

[67] K. J. Humphry, "Low Reynolds number flows for microfluidic technologies: Instabilities, drops, and inertially ordered particles," *Harvard University,* pp. 1-158, Jul 31 2009.

[68] K. J. Humphry, P. M. Kulkarni, D. A. Weitz, J. F. Morris, and H. A. Stone, "Axial and lateral particle ordering in finite Reynolds number channel flows," *Phys. Fluids,* vol. 22, p. 081703, Jan 1 2010.

[69] S. C. Hur, H. T. K. Tse, and D. Di Carlo, "Sheathless inertial cell ordering for extreme throughput flow cytometry," *Lab on a Chip,* vol. 10, p. 274, Jan 1 2010.

[70] J. Oakey, R. Applegate Jr, E. Arellano, and D. Di Carlo, "Particle Focusing in Staged Inertial Microfluidic Devices for Flow Cytometry," *Anal. Chem,* Jan 1 2010.

[71] A. A. S. Bhagat, S. S. Kuntaegowdanahalli, N. Kaval, C. J. Seliskar, and I. Papautsky, "Inertial microfluidics for sheath-less high-throughput flow cytometry," *Biomed Microdevices,* vol. 12, pp. 187-195, Apr 28 2010.

[72] J. Edd, D. Di Carlo, K. Humphry, S. Köster, D. Irimia, D. Weitz*, et al.*, "Controlled encapsulation of single cells into monodisperse picoliter drops," *Lab Chip,* vol. 8, p. 1262, 2008.

[73] E. Kemna, R. Schoeman, F. Wolbers, I. Vermes, D. A. Weitz, and A. Van Den Berg, "High-yield cell ordering and deterministic cell-in-droplet encapsulation using Dean flow in a curved microchannel," *Lab on a Chip,* pp. 1-10, Jan 1 2012.

[74] H. Amini, E. Sollier, and W. Weaver…, "Intrinsic particle-induced lateral transport in microchannels," *Proceedings of the ...,* Jan 1 2012.

[75] A. J. Mach, J. H. Kim, A. Arshi, S. C. Hur, and D. Di Carlo, "Automated cellular sample preparation using a Centrifuge-on-a-Chip," *Lab on a Chip,* pp. 1-8, Jan 1 2011.

[76] S. C. Hur, A. J. Mach, and D. Di Carlo, "High-throughput size-based rare cell enrichment using microscale vortices," *Biomicrofluidics,* vol. 5, p. 022206, Jan 1 2011.

[77] S. Hur and H. Yun, "Sequential multi-molecule delivery using vortex-assisted electroporation," *Lab Chip,* 2013.

[78] J. Martel…, "Inertial focusing dynamics in spiral microchannels," *Physics of Fluids,* Jan 1 2012.

[79] J. Zhang and B. Zhang, "Dean equations extended to a rotating helical pipe flow," *Journal of engineering mechanics,* vol. 129, p. 823, 2003.

[80] A. Chung, D. Pulido, J. C. Oka, H. Amini, M. Masaeli, and D. Di Carlo, "Microstructure-induced helical vortices allow single-stream and long-term inertial focusing," *Lab Chip,* pp. 1-10, Jan 1 2013.

[81] A. J. Chung, D. R. Gossett, and D. Di Carlo, "Three Dimensional, Sheathless, and High-Throughput Microparticle Inertial Focusing Through Geometry-Induced Secondary Flows," *Small,* vol. 9, pp. 685-690, Nov 12 2012.
[82] M. Kersaudy-Kerhoas, R. Dhariwal, M. P. Y. Desmulliez, and L. Jouvet, "Hydrodynamic blood plasma separation in microfluidic channels," *Microfluidics and Nanofluidics,* vol. 8, pp. 105-114, Jan 8 2010.
[83] J. Park, S. Song, and H. Jung, "Continuous focusing of microparticles using inertial lift force and vorticity via multi-orifice microfluidic channels," *Lab Chip,* vol. 9, pp. 939-948, 2009.
[84] W. R. Dean, "Fluid Motion in a Curved Channel," *Proceedings of the Royal Society A: Mathematical, Physical and Engineering Sciences,* vol. 121, pp. 402-420, Nov 1 1928.
[85] S. Berger, L. Talbot, and L. Yao, "Flow in curved pipes," *Annual Review of Fluid Mechanics,* vol. 15, pp. 461-512, 1983.
[86] H. J. D. Vriend, "Velocity redistribution in curved rectangular channels," *Journal of fluid mechanics,* vol. 107, pp. 423-439, 1981.
[87] M. Norouzi and N. Biglari, "An analytical solution for Dean flow in curved ducts with rectangular cross section," *Physics of Fluids,* vol. 25, p. 053602, 2013.
[88] K. Cheng and M. Akiyama, "Laminar forced convection heat transfer in curved rectangular channels," *International Journal of Heat and Mass Transfer,* vol. 13, pp. 471-490, 1970.
[89] D. Di Carlo, J. Edd, D. Irimia, R. Tompkins, and M. Toner, "Equilibrium separation and filtration of particles using differential inertial focusing.," *Anal. Chem.,* vol. 80, p. 2204, 2008.
[90] S. S. Kuntaegowdanahalli, A. A. S. Bhagat, G. Kumar, and I. Papautsky, "Inertial microfluidics for continuous particle separation in spiral microchannels," *Lab Chip,* vol. 9, p. 2973, Jan 1 2009.
[91] A. Russom, A. Gupta, S. Nagrath, D. Carlo, J. Edd, and M. Toner, "Differential inertial focusing of particles in curved low-aspect-ratio microchannels," *New Journal of Physics,* vol. 11, p. 075025, 2009.
[92] G. Guan, L. Wu, A. A. Bhagat, Z. Li, P. C. Y. Chen, S. Chao*, et al.*, "Spiral microchannel with rectangular and trapezoidal cross-sections for size based particle separation," *Sci. Rep.,* vol. 3, pp. 1-9, Mar 18 2013.
[93] L. Wu, G. Guan, H. Hou, A. Bhagat, and J. Han, "Separation of Leukocytes From Blood Using Spiral Channel With Trapezoid Cross-section," *Analytical Chemistry,* Jan 1 2012.
[94] E. W. Majid, G. Guan, B. L. Khoo, W. C. Lee, A. A. S. Bhagat, D. S.-W. Tan*, et al.*, "Slanted spiral microfluidics for the ultra-fast, label-free isolation of circulating tumor cells," *Lab Chip,* pp. 1-27, Jan 1 2013.
[95] J. Sun, M. Li, C. Liu, Y. Zhang, D. Liu, W. Liu*, et al.*, "Double Spiral Microchannel for Label-free Tumor Cell Separation and Enrichment," *Lab on a Chip,* pp. 1-11, Jan 1 2012.
[96] T. Tanaka, T. Ishikawa, K. Numayama-Tsuruta, Y. Imai, H. Ueno, N. Matsuki*, et al.*, "Separation of cancer cells from a red blood cell suspension using inertial force," *Lab on a Chip,* pp. 1-31, Jan 1 2012.

[97] T. Tanaka, T. Ishikawa, K. Numayama-Tsuruta, Y. Imai, H. Ueno, T. Yoshimoto, *et al.*, "Inertial migration of cancer cells in blood flow in microchannels," *Biomed Microdevices,* pp. 1-9, Sep 6 2011.
[98] J. Hansson, M. J. Karlsson, T. Haraldsson, H. Brismar, W. Van Der Wijngaart, and A. Russom, "Inertial microfluidics in parallel channels for high-throughput applications," *Lab on a Chip,* pp. 1-9, Jan 1 2012.
[99] N. Xiang, H. Yi, K. Chen, D. Sun, D. Jiang, Q. Dai, *et al.*, "High-throughput inertial particle focusing in a curved microchannel: Insights into the flow-rate regulation mechanism and process model," *Biomicrofluidics,* Jan 1 2013.
[100] A. Bhagat, S. Kuntaegowdanahalli, and I. Papautsky, "Continuous particle separation in spiral microchannels using dean flows and differential migration," *Lab Chip,* vol. 8, pp. 1906-1914, 2008.
[101] T. Gervais, J. El-Ali, A. Günther, and K. Jensen, "Flow-induced deformation of shallow microfluidic channels," *Lab Chip,* vol. 6, pp. 500-507, 2006.
[102] B. S. Hardy, K. Uechi, J. Zhen, and H. Pirouz Kavehpour, "The deformation of flexible PDMS microchannels under a pressure driven flow," *Lab on a Chip,* vol. 9, p. 935, Jan 1 2009.
[103] E. Sollier, C. Murray, P. Maoddi, and D. Di Carlo, "Rapid prototyping polymers for microfluidic devices and high pressure injections," *Lab on a Chip,* pp. 1-14, Jan 1 2011.
[104] D. R. Gossett and D. D. Carlo, "Particle Focusing Mechanisms in Curving Confined Flows," *Anal. Chem.,* vol. 81, pp. 8459-8465, Oct 15 2009.
[105] S. Ookawara, R. Higashi, D. Street, and K. Ogawa, "Feasibility study on concentration of slurry and classification of contained particles by microchannel," *Chemical Engineering Journal,* vol. 101, pp. 171-178, 2004.
[106] N. Xiang, K. Chen, D. Sun, S. Wang, H. Yi, and Z. Ni, "Quantitative characterization of the focusing process and dynamic behavior of differently sized microparticles in a spiral microchannel," *Microfluid Nanofluid,* pp. 1-11, Jul 8 2012.
[107] A. Bhagat, S. Kuntaegowdanahalli, and I. Papautsky, "Enhanced particle filtration in straight microchannels using shear-modulated inertial migration," *Physics of Fluids,* vol. 20, p. 101702, 2008.
[108] A. Ciftlik, M. Ettori, and M. Gijs, "High throughput-per-footprint intertial focusing," *Small,* 2013.
[109] A. Hasni, K. Göbbels, A. Thiebes, P. Bräunig, W. Mokwa, and U. Schnakenberg, "Focusing and Sorting of Particles in Spiral Microfluidic Channels," *Procedia Engineering,* vol. 25, pp. 1197-1200, 2011.
[110] J. Seo, M. Lean, and A. Kole, "Membrane-free microfiltration by asymmetric inertial migration," *Appl. Phys. Lett.,* vol. 91, p. 033901, 2007.
[111] K. W. Seo, Y. S. Choi, and S. J. Lee, "Dean-coupled inertial migration and transient focusing of particles in a curved microscale pipe flow," *Exp Fluids,* vol. 53, pp. 1867-1877, Dec 20 2012.
[112] J. Z. e. Al, "Inertial focusing in a straight channel with asymmetrical expansion--contraction cavity arrays using two secondary flows," pp. 1-14, Jul 24 2013.

[113] S. Ookawara, D. Street, and K. Ogawa, "A numerical study on a macroscopic Stokes number based on shear-induced interparticle collisions in a micro-separator/classifier," *Chemical Engineering Journal,* vol. 135, pp. S21-S29, 2008.
[114] Y.-S. Choi, K.-W. Seo, and S.-J. Lee, "Lateral and cross-lateral focusing of spherical particles in a square microchannel," *Lab on a Chip,* vol. 11, p. 460, Jan 1 2011.
[115] A. A. Bhagat, "Inertial Microfluidics for Particle Separation and Filtration," *University of Cincinnati,* pp. 1-105, Mar 3 2009.
[116] W. Dean and J. Hurst, "Note on the motion of fluid in a curved pipe," *Mathematika,* vol. 6, pp. 77-85, 1959.
[117] E. Ozkumur, A. M. Shah, J. C. Ciciliano, B. L. Emmink, D. T. Miyamoto, E. Brachtel*, et al.*, "Inertial Focusing for Tumor Antigen-Dependent and -Independent Sorting of Rare Circulating Tumor Cells," *Science Translational Medicine,* vol. 5, pp. 179ra47-179ra47, Apr 3 2013.
[118] H. W. Hou, M. E. Warkiani, B. L. Khoo, Z. R. Li, R. A. Soo, D. S.-W. Tan*, et al.*, "Isolation and retrieval of circulating tumor cells using centrifugal forces," *Sci. Rep.,* vol. 3, pp. 1-8, Feb 12 2013.
[119] S. T. Wereley and C. D. Meinhart, "Recent Advances in Micro-Particle Image Velocimetry," *Annu. Rev. Fluid Mech.,* vol. 42, pp. 557-576, Jan 1 2010.
[120] J. Fung, "Measuring the 3D Dynamics of Multiple Colloidal Particles with Digital Holographic Microscopy," *Harvard University,* pp. 1-203, Jun 14 2013.
[121] Y.-S. Choi and S.-J. Lee, "Holographic analysis of three-dimensional inertial migration of spherical particles in micro-scale pipe flow," *Microfluidics and Nanofluidics,* vol. 9, pp. 819-829, Oct 26 2010.